Doctoral Dissertation
Doctoral Program in Energy Engineering (30th Cycle)

Injection and combustion analysis and knock detection models for high-efficiency natural gas engines

By

Danilo Laurenzano

******

Supervisor(s):
Prof. Daniela Anna Misul, Supervisor
Prof. Ezio Spessa, Co-Supervisor

Doctoral Examination Committee:
Prof. Roberto Cipollone, Referee, Università degli studi dell'Aquila
Prof. Luis Parras Anguita, Universidad De Málaga

Politecnico di Torino
2018

Declaration

I hereby declare that, the contents and organization of this dissertation constitute my own original work and does not compromise in any way the rights of third parties, including those relating to the security of personal data.

Danilo Laurenzano

2018

* This dissertation is presented in partial fulfillment of the requirements for **Ph.D. degree** in the Graduate School of Politecnico di Torino (ScuDo).

Alla mia famiglia, ai miei amici e a Valeria

Ringraziamenti

Abstract

Between different sectors, GHG emissions released by automotive one in 2010 were 4.5 $GtCO_2$, the 14% of the total (32 $GtCO_2$). Moreover, transport sector depends by more than 93% on oil, to be refined into gasoline and diesel fuel. Natural gas demand in transport sector has clearly increased in the last decade considering the lowest CO_2 emissions per units of energy produced among different fossil fuels but it will be used mostly in the next future. Among different sectors, the 21 % of the energy demand is indeed supplied by NG, due to lower price and reduced GHG emissions. Storage type (compressed natural gas or liquefied natural gas) and vehicle type (road transport, marine transport, etc.) mainly discriminate natural gas engine layouts. Spark-ignition natural gas engine with different configurations will be indeed taken into consideration in this research project. Today, vehicles for the road transport fueled with compressed natural gas are mainly bi-fuel ones with both gasoline and natural gas feeding system with a manual or automatic switch. To mitigate knock event, engine layout is designed up to gasoline characteristics and engine performances with natural gas are not fully exploited. Mono-fuel configuration is capable to totally exploit the potential of natural gas. Therefore, this thesis will focus on the development of mono-fuel natural gas engines and improvements in injection and combustion strategies have to be reached by implementing new combustion chamber shape, improved ignition management and improved injection systems.

A detailed analysis of the natural gas injection system will be hence carried out. Different injection system layouts will be analyzed: single-point, multi-point and direct injection systems, focusing on pressure reducing valve dynamic. As a matter of fact, its behavior affects the dynamic response of the injection system: mismatch between estimated injected fuel and real one could be appreciated. Typically, average rail pressure evaluated by ECU differs from mean value during injection window. Therefore, detailed analysis will be carried out on experimental data and a 0D-1D numerical model will be

developed to enhance the problem understanding. The research activity has been carried out in order to reproduce properly all the components of the pressure reducing valve which affects the dynamic response of the injections system. The numerical model will give useful explanation of the fuel mass injected mismatch.

Then, a heavy-duty spark ignition compressed natural gas engine provided with two different injection systems will be examined. A standardized single-point injection system and a prototypal multi-point one will be evaluated so as to evaluate the possibility for performance enhancement. Cyclic variation and combustion efficiency for each configuration will be analyzed, proving the highest combustion efficiency of the prototypal configuration. Moreover, possible improvements with new engine control strategies will be investigated by adopting a 0D-1D numerical model. Single-point injection system modelling will prove the impossibility for efficiency improvement whereas multi-point injection system can be optimized by adopting enhanced strategies. As a matter of fact, fire-skipping mode will be simulated. Feasible reductions of fuel consumption under partial load conditions will be shown: decrease in fuel consumption up to 12% will be proved.

Finally, a new methodology for combustion, cyclic variation and knock onset modelling will be presented. Indeed, high-efficiency natural gas engines could in turn lead to knock conditions due to higher CR and different combustion chamber shape. Experimental analysis at test bench could be carried out to calibrate appropriate ECU control strategies for knock mitigation, but an experimental campaign under knock condition is dangerous and costly due to possible failure of mechanical parts of the engine. Numerical models for auto-ignition prediction could hence overcome this problem. Therefore, a predictive fractal combustion tool will be calibrated: it will be able to perform a correct mass fraction burned evolution estimation for different operating conditions (speeds, loads, relative air-to-fuel ratio, etc.). Then, knock onset estimation based on auto-integral (its usage is satisfactory considering the high natural gas chemical stability) coupled with a new method for cyclic variability simulation will be adopted; these two phenomena are indeed strictly correlated. A correct estimation of the percentage of knocking cycles will be shown. This new methodology will be carried out and verified on two light-duty spark ignition engines with different characteristics so as to verify its goodness.

Contents

List of Figures

List of Tables

Nomenclature

BDC	Bottom dead center
bmep	Brake mean effective pressure
BSFC	Brake Specific Fuel Consumption
CCV	Cycle-to-Cycle Variability
CI	Compression Ignition
CNG	Compressed natural gas
CR	Compression Ratio
D/S	Downstream
DI	Direct Injection
DISI	Direct Injection Spark Ignition Engine
DOE	Design of Experiment
ECU	Electronic Control Unit
EFI	Electronic Fuel Injection
EGO	Exhaust Gas Oxygen sensor
EGR	Exhaust Gas Recirculation
EIVC	Early Intake Valve Closing
EIVO	Early Intake Valve Opening

EOC   End of Combustion

EOI   End of Injection

ET   Energizing time

FFT   Fast Fourier Transform

FL   Full load

GHG   Greenhouse gas

GtCO2   Gigatonne carbon dioxide equivalent

HC   Unburnt Hydrocarbon

HRR   Heat release rate

ICE   Internal Combustion Engine

IMEP   Indicated Mean Effective Pressure

IVC   Intake valve closing

KI   Knock Index

LES   Large Eddy Simulation

LHV   Lower Heating Value

LIVC   Late Intake Valve Closing

MBT   Maximum Brake Torque

MHC   Methane Hydrocarbons

MPI   Multi-Point Injection

NG	Natural gas
PFP	Peak Firing Pressure
PL	Partial load
PM	Particulate matter
PSD	Power Spectral Density
RON	Research Octane Number
SA	Spark advance
SI	Spark Ignition
SOx	Sulphur Oxide
SPI	Single-Point Injection
TC	Turbo Compressor
TDC	Top Dead Center
THC	Total Hydrocarbons
TPA	Three-Pressure Analysis combustion model
TWC	Three-way Catalytic Converter
U/S	Upstream
UEGO	Universal Exhaust Gas Oxygen sensor
VVA	Variable Valve Actuation
WEO	World Energy Outlook

WG   Wastegate

WOT   Wide open throttle

Symbols

A_b Spherical Flame Area

A_f Flame area

Da   Damköholer dimensionless number

D_L Molecular diffusivity

f_N Nyquist Frequency

f_S Sampling frequency

h_{min} Chamber clearance at TDC

k   Spring stiffness

Ka   First Karlovitz dimensionless number

Ka_δ Second Karlovitz dimensionless number

l_I Integral length scale

l_K Kolmogorov length scale

l_δ Inner layer length scale

m   Mass

m_b Burned gas mass

m_u Unburned gas mass

$\dot{m}_i$ Mass flow rates flowing inside the cylinder

$\dot{m}_{inj}$ Injected mass flow rate

$\dot{m}_o$ Mass flow rates flowing outside the cylinder

n   Engine speed [rpm]

P	Rate of Turbulent Kinetic Energy Production
R	Gas constant
Re_T	Turbulent Reynolds number
S_b	Turbulent Flame Speed
S_L	Laminar flame speed
S_p	Piston position from TDC
U	Fluid velocity
u'	Turbulence intensity
u_η	Characteristic Kolmogorov scale speed
v_i	Entering speed
v_{inj}	Speed of the injected gas.
X_{res}	Residual gas fraction
α	Air-to-fuel ratio
α_{st}	Stoichiometric air-to-fuel ratio
β	Damping coefficient
γ	Heat capacity ratio
δ_L	Flame thickness
ε	Rate of Turbulent Kinetic Energy Dissipation
ε_i	Inner Cutoff Length Scale
ε_o	Outer Cutoff Length Scale
λ	Relative air-to-fuel ratio
ν	Kinematic viscosity

ρ_u	Unburned gas density
τ_a	Ignition delay
τ_L	Characteristic chemical reaction time
τ_T	Characteristic Turbulent Eddy turn over time
τ_η	Characteristic Kolmogorov scale turn over time
ω	Engine speed [rad/s]

1 Introduction

1.1 Natural gas and transport sector

Nowadays the climate change, which depends on greenhouse-gas (GHG) emissions, is one of the most demanding issues for governments all around the world [1]. The human race has changed the natural condition of the atmosphere since late 18th century, which represents the well-known Industrial Revolution period [2]. Specifically, during the last two centuries, the concentration of carbon dioxide (CO_2) has increased from 275 ppm to 405 ppm [3, 4]. In 2014, 29% of the energy mix came from coal, 31% from oil, 21% from gas, 5% from nuclear, 3% from hydro, 10% from bioenergy and 1% from renewables; therefore, the fossil fuel share among different sectors was still considerable and equal to 81% [1]. WEO presents three main scenarios – 450 Scenario, New Policies Scenario and Current Policies Scenario - to forecast the different solutions in order to enhance global warming arising: the main goal of governments will be GHG emissions reduction. Between different sectors, GHG emissions released by automotive one in 2010 were 4.5 $GtCO_2$, the 14% of the total (32 $GtCO_2$) as shown in Fig.1.1 [5]. Hence, considering the almost total dependency of transport sector is almost total dependent on fossil fuel like gasoline, diesel fuel and jet fuel, decarbonization strategies have to be implemented [6]. The CO_2 production spread depends on different energy sources and a fuel switching strategy is desirable.
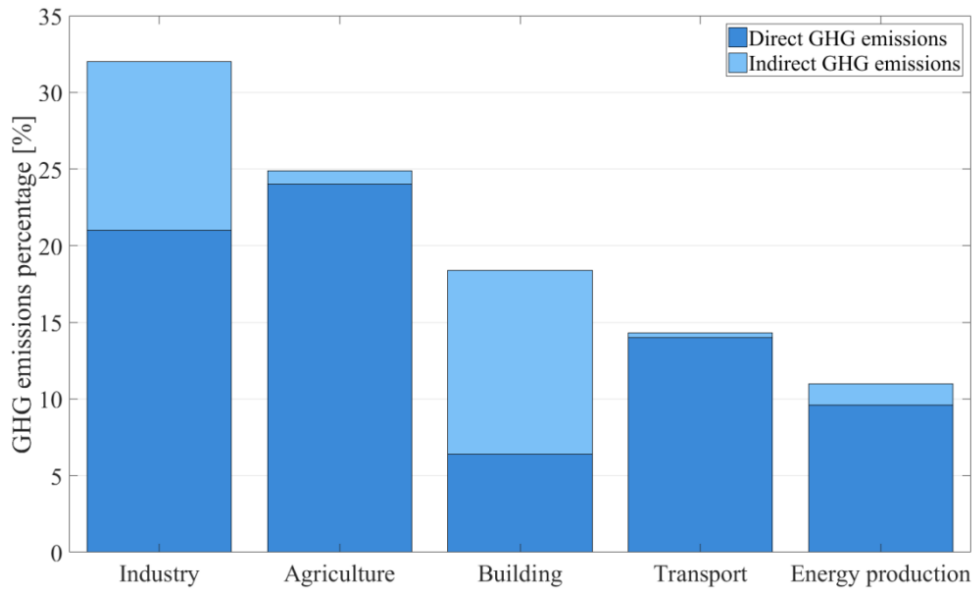
Figure 1.1: GHGs emissions by different sectors [5]

Natural gas (NG) is a rising solution in the transport sector because is mainly consisting by methane (CH_4), an alkane hydrocarbon with the highest hydrogen-to-carbon ratio (for gasoline and diesel fuel is typically equal to 1.85) of all fossil fuels and, as shown in Table 1.1, it has the lowest CO_2 emissions per units of energy produced. Indeed, among different sectors, the 21 per cent of the energy demand is supplied by NG, due to lower price and reduced GHG emissions [1].

Table 1.1: Carbon dioxide emissions per units of energy by fuel [6]

Fuel	CO_2 emission per units of energy [kg/kWh]
Coal	0.334
Diesel fuel and heating oil	0.250
Gasoline (without ethanol)	0.243
Propane	0.215
Natural gas	0.181

In the automotive sector, the reduced proliferation of NG vehicles has to be mainly ascribed to storage issues. Methane is in gaseous state at environment condition: considering a fuel tank for a light duty car of 45 dm^3, due to methane characteristics (Table 1.2), the total amount of stored mass is 3e-2 kg (at a pressure of 1 bar and temperature of 20°C) much lower than 30.6 kg for gasoline. In order to increase the storage capacity, methane and in particular NG can be stored in compressed form (CNG) or in liquefied one (LNG). In the former case the storage pressure could reach 250 bar in order to increase the amount of mass to 7.3 kg. CNG tank has to be designed in order to comply with ISO regulations [7] that specify minimum requirements for refillable on-board gas cylinders. The latter case is based on conversion of natural gas in liquid form to utilize non-pressurized tank. Natural gas is condensed into liquid at 111.66 K with a refrigeration process in order to achieve a higher reduction in volume: LNG density is generally equal to 0.42 kg/dm^3, 2.6 times higher than CNG and of the same order of magnitude of gasoline and diesel fuel. Anyway, LNG technology is typically used to facilitate transport of natural gas. In the transport sector it is adopted in over-the-road trucks due to cryogenic tank need.

Table 1.2: Methane characteristics [8]

Properties	Value
Chemical formula	CH_4
Molar mass (g/mol)	16.04
Specific gas constant (J/kg K)	518.29
Melting point (K)	90.7
Boiling point (K)	111.66
Lower Heating Value (MJ/kg)	50
Heat capacity ratio (-)	1.33
Adiabatic flame temperature (K)	2236

Natural gas demand in transport sector has clearly increased in the last decade and considering global gas demand projection for different scenarios it will nearly double up in the next two decades. Road transport will account for two-thirds of the growth. Infrastructure investment will be the key point for natural gas development in road transport: the scarce percentage of refilling station with natural gas infrastructure makes natural gas vehicles unattractive [1].

1.2 Natural gas engine layouts

Natural gas propulsion is characterized by different layouts, depending on storage type (CNG or LNG) and vehicle type (road transport, marine transport, etc.) Most of the vehicles fueled with compressed natural gas are equipped with bi-fuel gasoline-CNG spark ignition (SI) engines. CNG supply system is mainly composed by: a CNG tank, a safe valve, one or more pressure regulator, a rail with injectors and a fuel switch system. Conversion of gasoline engine into gasoline-CNG one has been done for the first time in the first half of the 20th century by adopting a well-established scheme. In the second half of the previous century, the need of CNG as fuel for road transport was necessary mostly during the "Oil crisis" period (1973) due to oil embargo. However, nowadays the percentage of vehicles equipped with CNG is humble, but, as stated before, the demand will build up. Research activities have to be carried out in order to improve CNG vehicles' efficiency and performance by adopting enhanced control strategies for the fuel injection system and by analyzing engine characteristics that could be innovative.

Today, CNG vehicles for the road transport are mainly bi-fuel ones: vehicles with spark ignition engine with both gasoline and CNG feeding system with a manual or automatic switch. It is worth observing that the engine layout is designed due to gasoline characteristics, like combustion chamber [9]: gasoline has a major propensity to auto-ignition than methane (identified by the well-known Research Octane Number: $RON_{gasoline}=95$, $RON_{methane}=120$) therefore, in order to mitigate knock event for gasoline propulsion, the efficiency and performance with CNG are not fully exploited. The need of both gasoline and natural gas has to be mainly ascribed to the lack of fueling station with CNG supplying. Bi-fuel vehicle represents the necessity to reduce cost by keeping unchanged the range due to current infrastructure. A different usage of NG in the transport sector is provided by dual-fuel layout. Dual-fuel engine is typically obtained using compression ignition (CI) configuration, where air-NG mixture is produced in the intake manifold and ignited with a marine diesel oil

pilot injection. The aforementioned layout is mainly used for marine power market and it leads to two different operating modes [10]: CI typical mode or proper dual-fuel one. In the latter one, engine operates in lean-burn Otto principle way, with a lean air-natural gas mixture in order to prevent knock. GHG emissions are consistently reduced by 20 per cent, nitrogen oxide (NO_x) decreased significantly (85-90%) and Sulphur oxide (SO_x) and particular matter (PM) emissions are negligible [10, 11]. Timing of injected pilot fuel and of injected natural gas is meticulously controlled by an electronic control unit (ECU) to adjust air-fuel ratio in order to prevent knock (rich mixture) and misfire (lean mixture) occurrences. Dual-fuel utilization was introduced in marine transport to meet emission requirements, while diesel mode is still used due to higher combustion efficiency.

Finally yet importantly, mono-fuel SI engine can be found in road transport market, equipped with CNG or LNG supply system depending on vehicle size (CNG typically for light duty vehicles, LNG for heavy-duty ones), but those engines are still not fully optimized. Only this configuration is capable to totally exploit the potential of natural gas. This thesis will focus on the development of mono-fuel natural gas engines.

1.3 SI NG engine features

The adoption of natural gas as fuel for SI NG engines involves several differences with respect to gasoline [12]. The first main difference between these two fuels is the state during injection: natural gas is already a gas and, as consequence, some distinctions exist on mixture formation. In order to precisely control injection event, natural gas injector has to work like a choked nozzle [13], thus, injected quantity depends only on injection period and upstream conditions, beyond injection system layout (listed and explained below). Rail pressure is governed by a pressure regulator, instead of pressure pump and pressure limiter as for gasoline/diesel systems. Gas state of NG leads, as expected, to improvement in mixture formation, considering a reduction in time needed for charge mixing [14, 15]. However, gas injection reduces intake phase performance. Lack of fuel evaporation lowers the air temperature reduction effect, corresponding to higher temperature during compression stroke and hence on combustion and exhaust phases, possibly resulting in higher NO_x emissions [16]. Furthermore, gaseous state of natural gas reduces the volumetric efficiency due to lower mass density and larger occupied volume.

Intake phase performances can be increased with a proper intake system new design, concerning new layouts and injection system evolution. Improvements in combustion performance have to be reached too. Power generated by internal combustion engine (ICE) for different fuels is function of lower heating value, stoichiometric air-to-fuel ratio (assuming same operating conditions and same engine layout) and flame propagation speed. For NG SI engine brake power is 15% lower than gasoline one [15], nevertheless dedicated natural gas engine could overcome this problem. For instance, compression ratio for spark ignition gasoline engine is typically equal to 10:1, instead it could reach easily 15:1 with natural gas feeding due to higher knock resistance. Hence natural gas engine could rise in same power output of gasoline one but with considerable advantages such as: up to 20% reduction of brake specific fuel consumption (BSFC), lower CO_2 emission (around 30-35%), significantly lower CO (reduction of 30-45%) due to and unburnt hydrocarbon (HC) emissions (20-30%) [17]. Pollutant emission production is strictly correlated to fuel characteristics. Indeed, because of methane chemical characteristic (high hydrogen-to-carbon ratio) complete combustion of natural gas produces lower CO_2 than gasoline/diesel fuel. The highly stability of CH_4 reduces the possibility of incurring in incomplete combustion, therefore in carbon monoxide production. Chemical reaction mechanisms of CH_4 lower than gasoline leads to a reduced number of HC, taking into account the absence of well wetting effect too. NO_x production is the main worry, considering a 30% higher production than gasoline during stoichiometric combustion. Lean burn engines could reduce NO_x production issue, by involving an unusual aftertreatment system for a SI engine: air surplus is the main constraint for the three-way catalytic converter (TWC) and Diesel aftertreatment system should be adopted (appreciable cost increasing). This thesis will focus on stoichiometric combustion for NG SI engine, because NO_x emission quantity can be easily hold off with TWC.

1.4 High performance NG engine

Common NG engines have been produced starting from SI gasoline engine with few design modifications. Nevertheless, SI CNG engine can be improved by fully exploiting the natural gas characteristic as alternative fuel [18], considering a mono-fuel system. This dissertation shows experimental and simulation analysis and results that have been done on current and prototype internal combustion engine system in order to enhance efficiency and

performances. Research activities can mainly be focused on injection system and combustion analysis.

Injection system is invariably composed by different and well-defined components. Fig 1.2 shows a CNG injection system sketch: the tank with the high-pressure line and the rail with the low-pressure line are decoupled due to pressure reducer. Fuel mixture formation is strictly correlated to feeding system performances; therefore, research activities have to be primarily focused on the CNG injection modelling and control. The key factors of CNG fueling system are the behavior of the pressure regulator, correlated to the system geometries too, the injectors control and the feeding system type: single-point injection (SPI), multi-point injection (MPI) or direct-injection one (DI). Experimental analysis on the fueling system has to be performed in order to figure out the effect of the pressure regulator dynamic behavior on the injection goodness. As a matter of fact, NG injection system has one degree of freedom less than common SI engine, because, there is no recirculation between rail and tank. Therefore, pressure regulator is the major element considering the dynamic in the feeding system that has to be taken into account during injection control strategies design.
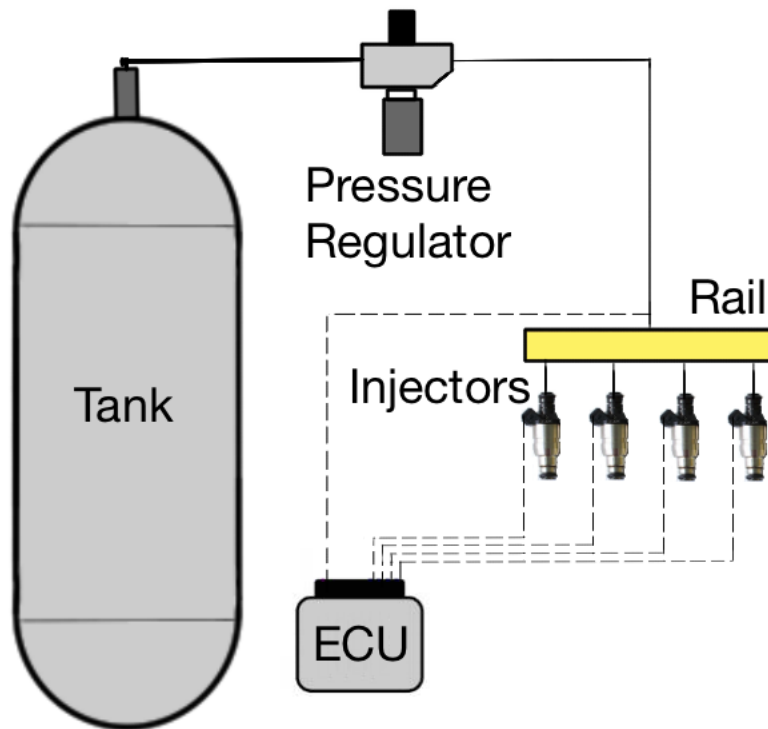
Figure 1.2: Injection system layout

Nowadays, the feeding system type is generally correlated to the engine size: for light-duty engine the MPI system is a must, instead SPI one is used in heavy-duty engine. Injection has to be approached to combustion chamber as much as possible in order to reduce the influence of NG gaseous nature on volumetric efficiency [19, 20]. Considering the abovementioned cases, CNG injection systems in road transport (both for light-duty and heavy-duty vehicles) can be improved.

Power output loss of engine fueled with CNG can be overcome by developing ICE elements correlated with combustion. In fact, one of the most meaningful attitudes of natural gas is the greater knock-resistance. In order to exploit this NG peculiarity, different strategies have to be implemented and the most important are listed: new combustion chamber shape, new turbo compressor (TC) strategies and improved ignition management [9].

- **New combustion chamber shape:** different configuration has to be realized to increase for instance the compression ratio (CR) and the turbulence intensity at the end of the compression stroke; higher

CR and turbulence are responsible of lower cycle-to-cycle variation (CCV) and higher combustion efficiency.

- **New TC strategies**: because of NG, the in-cylinder pressure during combustion could be higher with a lower possibility of incurring into auto-ignition. Therefore, boost level reachable with implementation of new TC can be higher than gasoline one. The higher boost level corresponds to higher power.

- **Improved ignition management:** current bi-fuel natural gas engines are not designed to work in maximum brake torque (MBT) timing due to structural limit (limitation on maximum in-cylinder pressure). Mono-fuel engine with a proper design can manage higher in-cylinder pressure and hence, MBT spark advance (SA) could be achieved (that corresponds to higher power and lower cyclic variation).

Although previous strategies introduce desirable improvements of engine efficiency and power, knock occurrence becomes a possibility. Knock is a well-known abnormal combustion phenomenon that occurs in SI engine when a portion of the air-fuel mixture ahead of the flame front auto-ignites. The step release of chemical energy causes a rapid local buildup of the in-cylinder pressure and, therefore, propagation of pressure waves inside the chamber that affects fatigue life of components like spark, piston, piston rings, etc. Auto-ignition of the end-gas is governed by pressure and temperature time history, and by fuel chemical characteristics [9]. As listed before, natural gas is mainly composed by methane that has a RON considerably higher than gasoline one, and hence, for bi-fuel high performance SI engine fueled with NG is impossible to incur in knock condition. While an extensive literature can be found on gasoline engines under knock condition, there is a lack of data for NG ones. In this thesis, experimental and simulation analysis on auto-ignition on a high-performance NG engine have been performed.

1.5 Simulation analysis

Nowadays, a full campaign of experimental analysis and calibration experiments on ICE is costly and time demanding, considering the amount of degree of freedom [21]. Moreover, the engine system complexity and non-linearity affects the preliminary estimation. Physically based simulation

analysis presents a satisfying solution in order to provide reliable results. Dedicated engine operations and control strategies can be preventively analyzed by modelling the entire engine system or single part with different approaches. Indeed, distinct modelling types can be discriminated considering the degree of detail. Typically, engine simulation concerns dynamic, fluid-dynamic and chemical events that can be described with different approaches, taking into account the degree of spatial resolution: modelling process can be divided from non-dimensional model to 3-D one.

Non-dimensional model can be considered as the lowest level of physical description: frequently, physical model is not considered to obtain model output from model boundary condition, and a "black box" with a mathematical finding is adopted. Although the detail level is very low, the computational time and cost are negligible; indeed, non-dimensional models are frequently used for real-time application as ECU calculation, whereas they are rejected for research activities. Heat transfer and thermodynamic problems for homogenous systems are generally analyzed through zero-dimensional time-dependent models. Dynamic and fluid-dynamic problems can be described by one-dimensional models: the former cases are based on second order differential equations in 1-D spatial and time domain. The latter ones can be described by one-dimensional equations when one dimension is big enough compared to the others, taking into consideration the continuity equation, the momentum equation and the energy conservation. 1-D models are consistently used for pipe wave flow phenomena (injection system, intake and exhaust flows, etc.) and valve mechanical translation (injectors, pressure reducer, etc.). Detail achievement is significant with an acceptable time requirement. The highest detail level for mechanical and flow motion can be achieved by adopting three-dimensional analysis. Considering flow characterization, computational fluid dynamics are well known methods depending on Navier-Stokes equations: the definition level is very high, although computational time and model complexity are consistent. Engine behavior can be evaluated by means of 1-D and 3-D analysis, in order to explore the effect of different elements on ICE main outputs (power, efficiency, pollutant emissions, etc.): recalling the multi degree of freedom issue, simulation purpose is the experimental analysis time reduction; hence, during this dissertation, different software for ICE simulation will be used.

1.6 Research aim and thesis outline

Spark-ignition natural gas engine with different layouts are taken into consideration in the research project. The main scope of the thesis can be summarized as follows:

1. A detailed analysis of the CNG injection system will be carried out. Different injection system layouts will be analyzed, focusing on pressure reducing valve dynamic. As a matter of fact, mismatch between estimated injected fuel and real one could be evaluated. Typically, average rail pressure evaluated by ECU differs from mean value during injection window. Detailed analysis will be carried out with 0D-1D numerical model, enhancing the problem understanding.

2. A heavy-duty SI CNG engine provided with two different injection systems will be examined. A standardized SPI system and a prototypal MPI ones will be evaluated. Cyclic variation and combustion efficiency for each configuration will be analyzed, proving the highest combustion efficiency of the new configuration. Moreover, possible improvements will be investigated by adopting a 0D-1D numerical model. SPI system will be modeled proving the impossibility of efficiency improvement. On the other hand, MPI system can be optimized by adopting enhanced strategies like fire-skipping mode. It will be numerically simulated and feasible reduction of fuel consumption under partial load conditions will be shown.

3. Finally, combustion, CCV and knock onset will be numerically modeled, introducing a new methodology. A predictive fractal combustion tool will be calibrated: it will be able to perform a correct mass fraction burned evolution estimation for different operating conditions (speeds, loads, relative air-to-fuel ratio, etc.). Knock onset prediction for CNG engines is one of the main topic of recent research activities. Experimental campaign is indeed too risky considering mechanical stresses produced by knock occurrence. Therefore, auto-ignition integral will be adopted (considering the high CNG chemical stability) coupled with a new method for cyclic variability simulation; these two phenomena are indeed strictly correlated. A correct estimation of the percentage of knocking cycles will be a powerful tool

for cost reduction aiming. This new methodology will be carried out and verified for two light-duty SI CNG engines.

1.7 References

[1]   IEA (2017), *World Energy Outlook 2017*, OECD Publishing, Paris/IEA, Paris. http://dx.doi.org/10.1787/weo-2017-en

[2]   S.A. Elias, Climate Change and Energy, In Encyclopedia of the Anthropocene, edited by Dominick A. Dellasala and Michael I. Goldstein, Elsevier, Oxford, 2018, Pages 457-466, ISBN 9780128135761,   https://doi.org/10.1016/B978-0-12-809665-9.10515-4.

[3]   Neftel, A., Friedli, H., Moor, E., Lotscher, H., Oeschger, H., Siegenthaler, U., & Stauffer, B. (1994). Historical carbon dioxide record from the Siple Station ice core. ESS-DIVE (Environmental System Science Data Infrastructure for a Virtual Ecosystem); Oak Ridge National Lab.(ORNL), Oak Ridge, TN (United States).

[4]   Keeling, R. F., Piper, S. C., Bollenbacher, A. F., & Walker, J. S. (2009). Atmospheric carbon dioxide record from Mauna Loa. ESS-DIVE (Environmental System Science Data Infrastructure for a Virtual Ecosystem); Oak Ridge National Laboratory (ORNL), Oak Ridge, TN (United States).

[5]   IPCC: Climate Change 2014 Synthesis Report, 2.1 Emissions of long-lived GHGs. https://www.ipcc.ch/report/ar5/syr/, accessed

[6]   EIA: 2017, International Energy Outlook, Washington, DC, US Department of Energy, Energy Information Administration, DOE/EIA-0484(2017)

[7]   International Organization for Standardization. (2013). Gas cylinders -- High pressure cylinders for the on-board storage of natural gas as a fuel for automotive vehicles (ISO 11439:2013).

[8]   Hodgman, C. D. (1951). Handbook of chemistry and physics (Vol. 71, No.3, p. 246). LW.

[9]   Heywood, J. B. (1988). Internal combustion engine fundamentals (Vol. 930). New York: Mcgraw-hill.

[10]   Woodyard, D. (2009). Pounder's marine diesel engines and gas turbines. Butterworth-Heinemann.

[11]   Johnson, D. R., Heltzel, R., Nix, A. C., Clark, N., & Darzi, M. (2017). Greenhouse gas emissions and fuel efficiency of in-use high horsepower diesel, dual fuel, and natural gas engines for unconventional well development. Applied Energy, 206, 739-750.

[12]   Khan, M. I., Yasmeen, T., Khan, M. I., Farooq, M., & Wakeel, M. (2016). Research progress in the development of natural gas as fuel for road vehicles: A bibliographic review (1991–2016). Renewable and Sustainable Energy Reviews, 66, 702-741.

[13]   Moran, M. J., Shapiro, H. N., Boettner, D. D., & Bailey, M. B. (2010). Fundamentals of engineering thermodynamics. John Wiley & Sons.

[14]   Bhandari K., Bansal A., Shukla A.& Khare M. (2005) Performance & Emissions of a Natural Gas Fueled Internal Combustion Engine-A Review. *Journal of Scientific & Industrial Research*, Vol.64, May2005, pp. 333-338.

[15]   Khan, M. I., Yasmeen, T., Khan, M. I., Farooq, M., & Wakeel, M. (2016). Research progress in the development of natural gas as fuel for road vehicles: A bibliographic review (1991–2016). Renewable and Sustainable Energy Reviews, 66, 702-741.

[16]   Kakaee, A. H., Paykani, A., & Ghajar, M. (2014). The influence of fuel composition on the combustion and emission characteristics of natural gas fueled engines. Renewable and Sustainable Energy Reviews, 38, 64-78.

[17]   Jahirul, M. I., Masjuki, H. H., Saidur, R., Kalam, M. A., Jayed, M. H., & Wazed, M. A. (2010). Comparative engine performance and emission analysis of CNG and gasoline in a retrofitted car engine. Applied Thermal Engineering, 30(14), 2219-2226.

[18]   Tilagone, R., Venturi, S., & Monnier, G. (2006). Natural gas-an environmentally friendly fuel for urban vehicles: the smart demonstrator approach. Oil & gas science and technology, 61(1), 155-164.

[19]   Thipse, S. S., Sonawane, S. B., FD'Souza, A., Rairikar, S. D., Kavathekar, K. K., & Marathe, N. V. (2015). Injection Strategies, Optimization and Simulation Techniques on DI CNG Technology (No. 2015-26-0046). SAE Technical Paper.

[20]   Choi, M., Lee, S., & Park, S. (2015). Numerical and experimental study of gaseous fuel injection for CNG direct injection. Fuel, 140, 693-700.

[21]   Guzzella, L., & Onder, C. (2009). Introduction to modeling and control of internal combustion engine systems. Springer Science & Business Media.

2 CNG injection system

* Part of the work described in this chapter has been previously published in:

1. Baratta, M., Kheshtinejad, H., Laurenzano, D., Misul, D., & Brunetti, S. (2015). Modelling aspects of a CNG injection system to predict its behavior under steady state conditions and throughout driving cycle simulations. Journal of Natural Gas Science and Engineering, 24, 52-63.
2. Kheshtinejad, H., Baratta, M., Laurenzano, D., Maino, C., & Misul, D. A. (2018). Investigation into the Potentials of a Dedicated Multi-Point Injection System for a production NG Single-Point Heavy-Duty Engine. SAE International Journal of Engines, 11(2018-01-9275).

2.1 Introduction to CNG injection system

Injection system represents the main difference between commonly gasoline/diesel engines and natural gas ones, due to fuel physical differences [1-3]. Light-duty vehicles are provided with a high-pressure tank, due to gaseous state condition of natural gas at environment temperature and pressure, in order to enhance the vehicle range. The fuel reservoir is designed in accordance with ISO regulations (ISO 11439:2013) to guarantee or to improve the level of safety currently insured by other vessels, by maintaining a light weight. The regulation involves cylinders of different material like seamless steel, seamless aluminum alloy and non-metallic material (like plastics, fiber-reinforced plastic composites, etc.) with a suggested working pressure of 200 bar (different working pressure can be adopted too) and it shows the design, construction and testing of the 4 different "Types" of tank [4]. In the above-mentioned standard, the ISO 15500-13:2012 is referenced: it displays the

feeding system components and specifies all the requirements and tests [5]. The *Road vehicles — Compressed natural gas (CNG) fuel system component* standard consists of the following parts.

- Part 1: General requirements and definitions
- Part 2: Performance and general test methods
- Part 3: Check valve
- Part 4: Manual valve
- Part 5: Manual cylinder valve
- Part 6: Automatic valve
- Part 7: Gas injector
- Part 8: Pressure indicator
- Part 9: Pressure regulator
- Part 10: Gas-flow adjuster
- Part 11: Gas/air mixer
- Part 12: Pressure relief valve (PRV)
- Part 13: Pressure relief device (PRD)
- Part 14: Excess flow valve
- Part 15: Gas-tight housing and ventilation hose
- Part 16: Rigid fuel line in stainless steel
- Part 17: Flexible fuel line
- Part 18: Filter
- Part 19: Fittings
- Part 20: Rigid fuel line in material other than stainless steel

In order to boost performance and efficiency of the forthcoming engines, the flow dynamic and injection layout of the CNG fueling system has to be carefully evaluated, because combustion efficiency is strictly correlated to mixture formation quality [6]. Flow dynamic depends on feeding system geometry, pressure regulator behavior and injection system layout. Generally, fueling system geometries are correlated to vehicle dimension and set due to standards, therefore, pressure regulator plays a major role in rail pressure control and dynamic. It is used in order to uncouple the high-pressure line (tank) to the low-pressure line (rail) by checking the downstream pressure: if the exit pressure is lower than desired one the valve delivers mass from tank to rail, whereas it arrests the CNG flow rate. Nevertheless, pressure regulator dynamic is affected by pressure waves in low-pressure line and occasionally by tank condition [7]. Finally, mixture formation quality depends on injection

system layout. For CNG engines, injection event has to be approached as much as possible to combustion chamber in order to raise volumetric efficiency. Moreover, in order to boost mixture formation, injection time has to be reduced and rail pressure has to be increased (keeping in mind standards limit vessel pressure) [8, 9]. Research activities have been carried out on the analysis of the injection system response depending on the feeding pressure [10]. Furthermore, injection window period is proportional to rail pressure; hence, lower rail pressure succeeds in worsening the volumetric efficiency. Engine power output and emissions are connected with air fuel mixing goodness too, thus the precise control of the injected fuel mass quantity is a key factor of the fueling system [11]. More specifically, considering the injector, the ratio between the downstream (D/S) pressure and the upstream (U/S) one (rail pressure) must be always kept lower than the natural gas critical ratio value:

$$\frac{p_{D/S}}{p_{U/S}} < \left(\frac{2}{\gamma + 1}\right)^{\frac{\gamma}{\gamma-1}} \qquad (2.1)$$

Where γ is the heat capacity ratio. With a pressure ratio lower than the critical one, the fuel mass flow rate is constant for a given rail pressure and the injected mass can be controlled by adjusting the injection energizing time (ET). However, injection control strategies have to be designed taking into consideration the pressure waves inside the rail [7, 12]. Due to a lack of researches in literature dealing with CNG injection systems modelling, Diesel reliable methodologies could be used for CNG applications [13, 14]. The characterization of the fuel injection system dynamic and the effects of the design parameters and engine operating conditions on the fueling system performance have to be carefully analyzed [15, 16]. Typically, simulations are performed in order to estimate the effects of the system design parameters on the injection event that are difficult to be experimentally quantified. Furthermore, validated numerical models could provide useful results also with different layout and control strategies. In [17] a new injection system for CNG engine was studied through a numerical analysis. The effects of a model-based predictive model with an embedded electro-valve for the rail pressure control were estimated. The analyzed system showed an appreciable enhancement of the rail pressure response during the engine transients. In [7] a sensitivity analysis on the primary geometric characteristic of the rail was carried out with a 1D numerical model, in order to estimate the effects of the injection system design on its fluid-dynamic behavior. In [18] the interaction between pressure

waves caused by injection events and by pressure regulator has been analyzed, by highlighting the noteworthy effect of the pressure valve dynamic on the injection system.

A part of present work focuses on the characterization of the pressure regulator behavior and impact on the fueling system dynamic, and the effect of the injection system layout on the mixture formation.

2.2 Pressure regulator for CNG system

Natural gas is typically stored in standardized tanks at high pressure (up to 250 bar) or in liquefied state due to its low energy density. In order to uncouple the rail pressure from the tank one, a pressure regulator valve is mandatory (Fig.2.1). For CNG engine, pressure reducer valve has to be designed in order to control the rail pressure so as to guarantee an accurate metering fuel flow. A correct setting of the injected fuel mass leads to a pollutant emission reduction and an enhancement of the vehicle drivability. The working rail pressure as to be set in accordance with injector type and with feeding system layout, but the pressure regulator has to guarantee limited oscillations of temperature and pressure due to compressibility of natural gas.
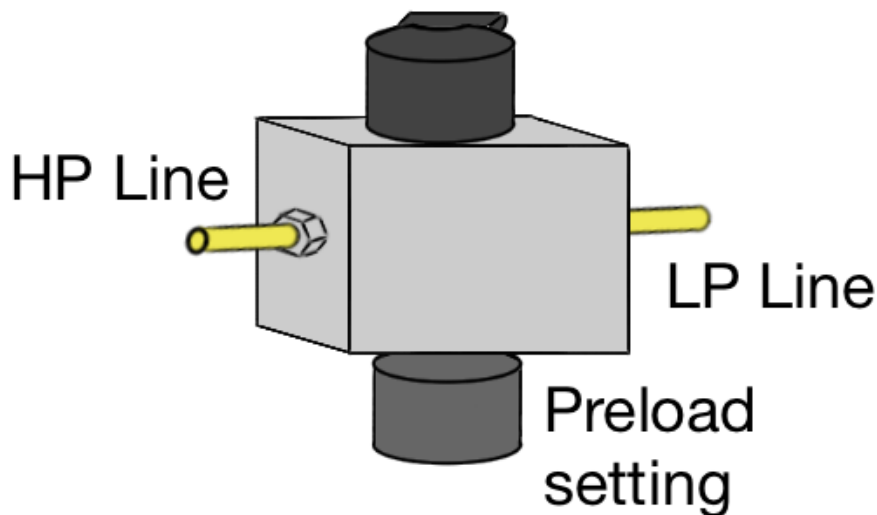
Figure 2.1: Pressure regulator

Pressure reducer valve could have different configurations: the valve could have more the one reduction stages and it could be either balanced or unbalanced. If there are multiple reduction stages, the effect of the pressure of the tank on the reducer valve is diminished. The adoption of a balanced pressure regulator could prevent the impact of tank condition on the valve itself. In Fig. 2.2 the two configurations have been shown: for a balanced valve the force of the spring is counterbalanced only by the force generated by the downstream pressure, instead for an unbalanced valve it is compensated by the force generated by the upstream pressure too.

$$F_s = F_0 + F_i$$

$$F_0 = P_{out} \cdot (A - A_i)$$

$$F_i = P_{out} \cdot A_i$$

$$F_s = P_{out} \cdot A_i + P_{out} \cdot (A - A_i)$$

(a)

$$F_s = F_0 + F_i$$

$$F_0 = P_{out} \cdot (A - A_i)$$

$$F_i = P_{in} \cdot A_i$$

$$F_s = P_{in} \cdot A_i + P_{out} \cdot (A - A_i)$$

(b)
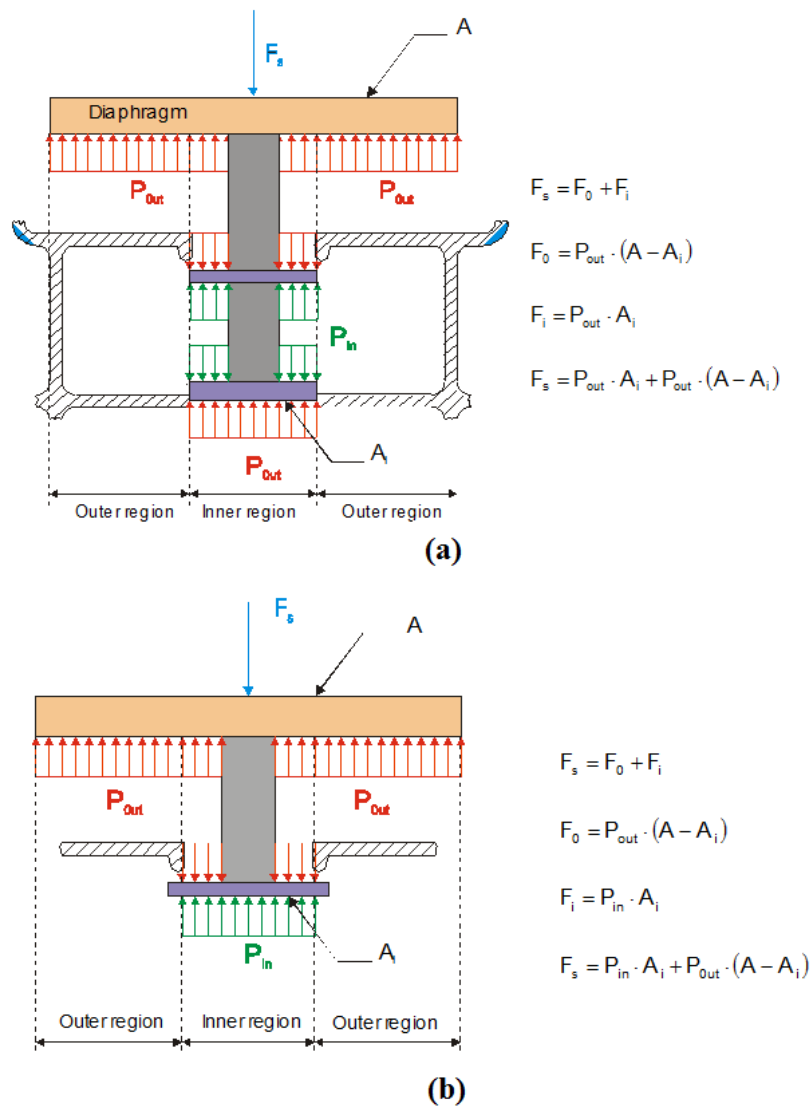
Figure 2.2: Balanced (a) and unbalanced (b) pressure regulators [19]

A pressure regulator valve is also affected by the so called "pressure drop" phenomenon. Fig. 2.3 shows the shape of the pressure downstream from the valve depending on the mass flow rate flowing through the regulator at a fixed upstream pressure. As the valve starts to operate, there is a sudden pressure drop called "Cracking drop" due to valve and spool resilience and misalignments between the piston and the seat. By increasing the mass flow rate, the pressure drop becomes smoother: this phase is called "Dynamic drop". It has mainly to be ascribed to the spring stiffness (and non-linearity) as well as to the frictions between the moving parts and the seat.
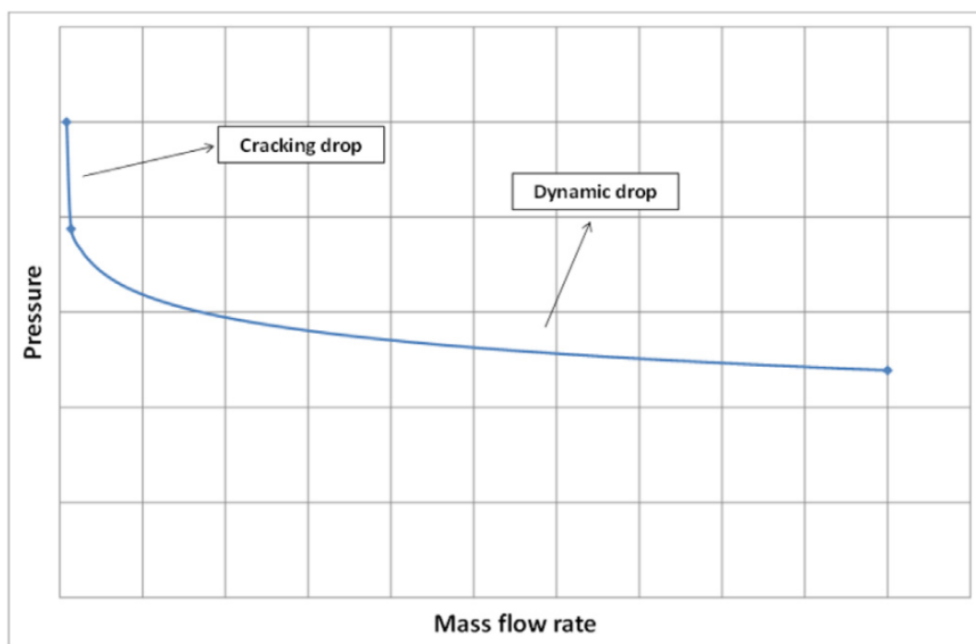
Figure 2.3: Pressure drop phenomenon: pressure downstream of the valve as a function of the mass fuel flow rate

Furthermore, the "creep" phenomenon occurs during the closing phase, when the pressure regulator locks the fuel passage between the tank and the rail: rail pressure builds up due to leakage from high-pressure line to low-pressure line because of stiffness of the closing valve surface. Finally, vale is affected by hysteresis phenomenon; therefore, downstream pressure is affected by fluctuating changing of the fuel flow rate. The amplitude of the hysteresis typically depends on sealing rings friction. For an unbalanced pressure regulator, the dynamic behavior could be evaluated referring to Figure 2.4.
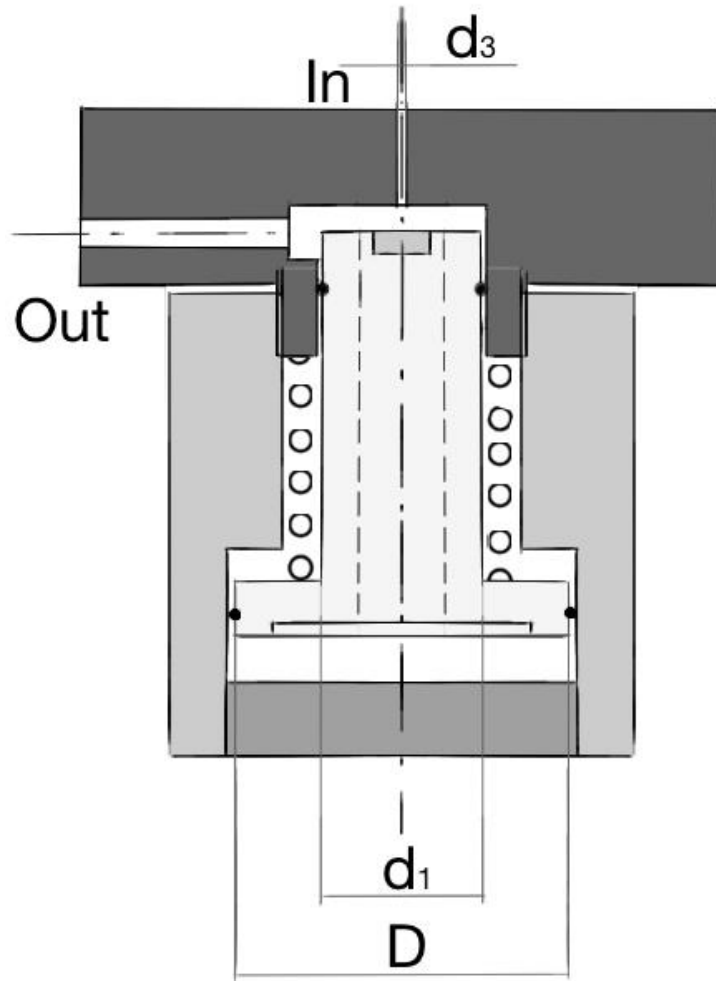
Figure 2.4: Unbalanced pressure regulator layout

The effects on the valve displacement can be evaluated, depending on the valve mass characteristics, as follows:

$$m\ddot{x}(t) + \beta\dot{x}(t) + (F_0 + kx(t)) - p_{D/S}(t)\left(\frac{\pi D^2}{4} - \frac{\pi d_1^2}{4}\right) + F_{U/S} = 0 \qquad (2.2)$$

Where m is the piston mass, β is the damping coefficient, k is the spring stiffness, F_0 is the spring pre-load, $F_{U/S}$ is the force deriving from the high-pressure line. The latter has two different characterizations: if the pressure reducing valve is closed, the force is equal to:

$$F_{U/S} = p_{U/S}\, \pi d_3{}^2 \qquad (2.3)$$

If the pressure reducing valve is working, the force can be derived by considering the momentum conservation. The force can be written as follows:

$$F_{U/S} = \dot{m}c = \pi d_3 x \frac{p_{U/S}{}^o}{\sqrt{RT^o}} \sqrt{\gamma \left(\frac{2}{\gamma+1}\right)^{\gamma+1/\gamma-1}} \sqrt{2\frac{\gamma}{\gamma+1}\frac{p_{U/S}{}^o}{\rho_{U/S}{}^o}} \qquad (2.4)$$

The tank pressure is always higher than critical value, therefore the pressure valve act like a chocked nozzle. The dynamic behavior of the pressure regulator and the downstream pressure are strictly connected. Hence, the force due to momentum conservation depends only on the tank pressure and can be added to the spring preload:

$$\ddot{x}(t) + \beta\dot{x}(t) + kx(t) = p_{D/S}(t)\frac{\pi(D^2 - d_1^2)}{4} - \left(F_0 + F_{U/S}\right) \qquad (2.5)$$

A feeding system with CNG will be evaluated with a 0D-1D numerical model in order to assess the effect of the pressure reducer behavior on the injection event. Indeed, experimental analyses are not able to fulfill the requirements. A deepest investigation on the results of a validated numerical model could lead to refined and dedicated injection control strategies.

2.3 CNG injection system layouts

The goal of the car manufacturers is the improvement of the air-to-fuel mixture preparation [20]. As a matter of fact, a better mixture leads to higher efficiency and lower pollutant emission [21]. Generally, natural gas engines operate with an Otto cycle (SI engines) with a single-point injection system or a multi-point one; the engineering solutions adopted with the abovementioned layouts are well-defined and the former is mostly used for heavy-duty vehicles, the latter for light-duty ones. Nowadays, car makers are moving to direct injection system in order to boost the ICE performances [22], although some engineering issues have to be analyzed: the rail pressure should be kept always higher than the critical value in order to control the amount of injected fuel only by adjusting the ET; a correct trade-off between rail pressure value and injection phasing has to be evaluated.

2.3.1 Single-point injection

Single-point injection system was the direct evolution of the carburetor, a mechanical device that works thanks to Bernoulli's principle: the fuel is directly sucked by the air flowing through the pipe due to Venturi effect [20]. Indeed, carburetor was replaced for passenger cars with electronic fuel injection (EFI) since 1992 to satisfy emission standards. The introduction of three-way catalytic converter (TWC) with EURO 1 standards was mandatory in order to reduce CO, HC and NOx emissions. It operates efficiently with a SI gasoline engine running in a precise window of air-to-fuel ratio, showed in Fig. 2.5 [20], and carburetor was no longer able to guarantee a precise control of air-to-fuel ratio (α).
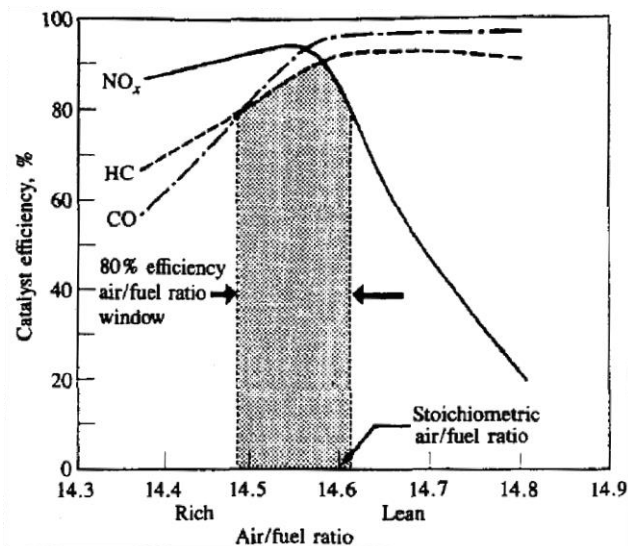
Figure 2.5: TWC efficiency conversion at different air-to-fuel ratio for SI gasoline ICE [19]

EFI technology with closed lambda loop was adopted to maintain air-to-fuel ratio close to the target value: the exhaust gas oxygen sensor (EGO), typically named λ sensor (λ is the relative air-to-fuel ratio, expressed as the ratio between nominal and stoichiometric one, α_{st}), returns a step signal function of the relative air-to-fuel ratio, with a high value for the rich mixture and a low value for the lean one. The ECU with a closed loop control holds the equivalence ratio in a narrow window by adjusting the ET, and α oscillates periodically. The single-point injection system has one or more injectors located together before intake manifold in order to maintain a homogenous charge at different operating conditions. Frequently, fuel is injected in the

throttle body before the throttle valve, and better mixture formation quality could be achieved by using a mixer (Fig. 2.6). SPI system is capable to prepare a uniform λ composition for each cylinder.
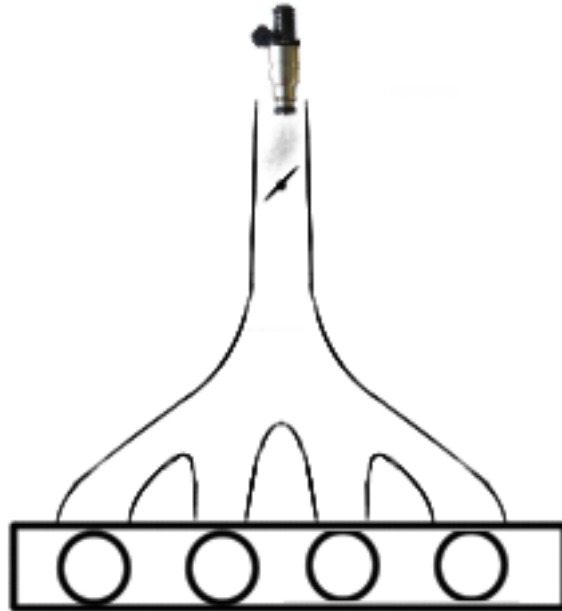
Figure 2.6: SPI system layout

Unfortunately, a single-point injection system introduces several issues for SI engine and in particular for CNG one. Overlap valve angles have to be reduced in order to avoid anomalous combustion in exhaust port and, as a consequence, exhaust gas temperatures increase [23]. Volumetric efficiency is affected by natural gas nature, therefore, SPI systems have the lowest efficiency [8, 9]. Finally, SPI system provides worse feedback to transient operation due to a significant spatial delay between injectors and combustion chamber [23].

2.3.2 Multi-point injection

Multi-point injection system could overcome some of the SPI system issues. One injector is placed in the intake runner before the intake port for each cylinder as shown in Figure 2.7.
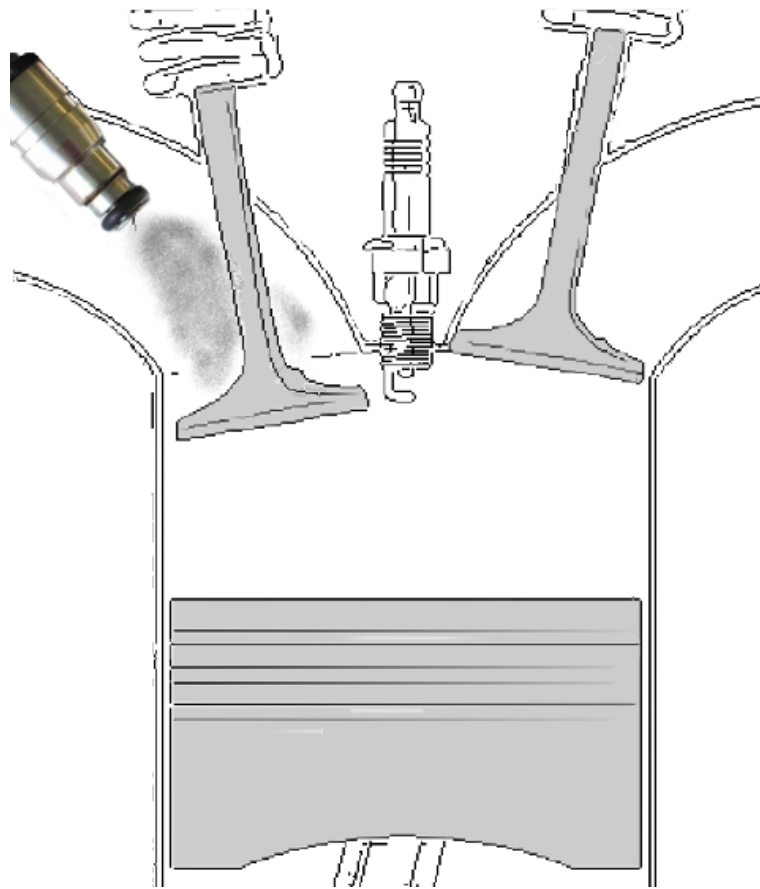
Figure 2.7: MPI system layout

The ET width could be determined with closed lambda loop or by considering look-up table functions of engine speed, intake manifold pressure and throttle valve position. The latter condition is typically adopted during full load conditions, whereby a stoichiometric mixture could lead to knock combustion: a rich mixture has to be adopted and ECU cannot operate in closed lambda loop due to EGO characteristics [24]. MPI system overcomes volumetric efficiency and transient response issues of SPI system, because injection is approached to combustion chamber [8, 9], with lower rail pressure (7-10 bar) than DI system. Nowadays, MPI is the common injection system layout for light-duty vehicles because it allows a better mixture formation with respect to single-point one and a reduced structural requirement than direct injection. Typically, CNG heavy-duty vehicles have mono-fuel engines derived from common ones (SI or CI), thus a SPI system is usually adopted because of easiness installation. However, MPI layout could be adopted because the

implementation is feasible and relatively accessible, providing the chance to improve engine efficiency and power. Indeed, MPI flexibility allows the usage of improved strategies: injection phase could be adjusted and controlled in order to deal with intake valve opening and valve overlap period and could be neglected for cylinder deactivation mode [25, 26]. The air-to-fuel ratio is evaluated by means of one lambda sensor independently from fueling system layout. The relative air-to-fuel ratio evaluated is a global information. Therefore, MPI engines (as well as DI ones) could suffer of cylinder-to-cylinder variations, because the amount of air received by each cylinder could be different, whereas the fuel injected is the same. A new intake system layout has to be designed to enhance the cylinder-to-cylinder equality and a correct injector positioning could improve the engine performance [27].

2.3.3 Direct injection

Direct injection spark ignition engine (DISI) has been the latest evolution for car manufacturer in light-duty sector. The layout is shown in Figure 2.8. Its implementation is the most complicated, indeed in order to guarantee acceptable ET window, rail pressure for DI system should be increased, according to higher downstream pressure. Moreover, the injector overlooks the combustion chamber, leading to high thermal and mechanical stresses, thus different materials have to be adopted. On the other hand, DI layout is the fueling system with the highest flexibility, and it's able to guarantee better engine performance. As a matter of fact, fuel could be injected after intake valve closing (IVC), avoiding reduction of air trapped. DI layout can ensure same levels of volumetric efficiency for different fuels: considering gaseous state of CNG, it is the most promising layout [8, 9].
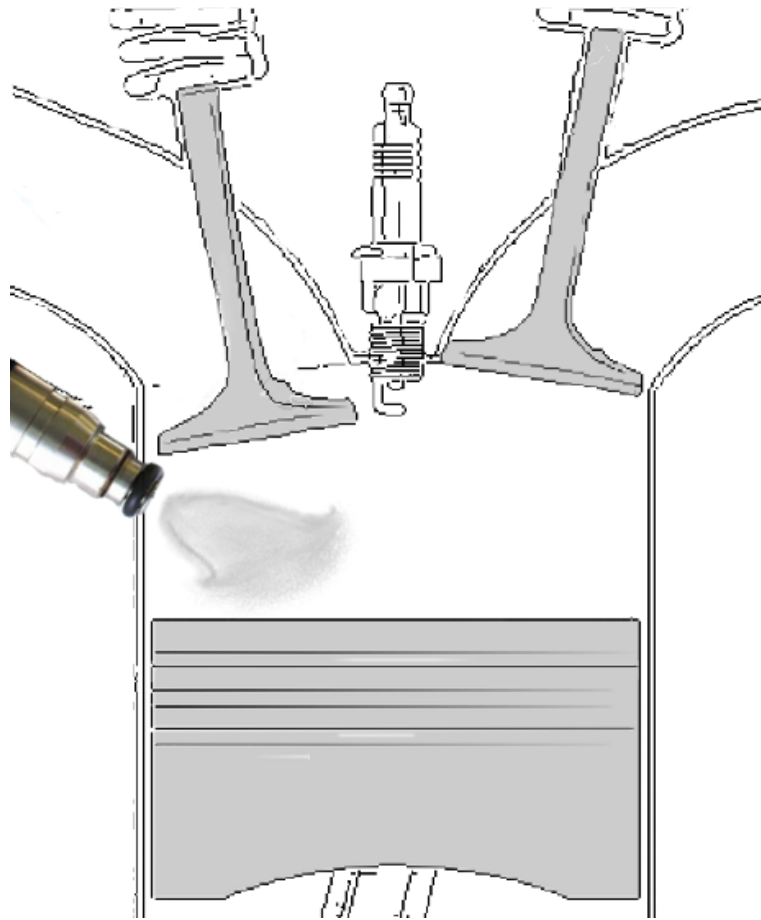
Figure 2.8: DISI system layout

Typically, DISI engine runs with homogeneous charge made during the compression stroke, but the system flexibility allows also different mixture preparation: stratified mixture could be formed with DI system. Higher engine performance could be achieved during partial loads by neglecting throttle valve (harsh reduction of the pumping loss) and by adjusting the charge composition. As a matter of fact, with a correct injection phasing at the end of the compression stroke and a proper shape of the piston surface, a stoichiometric mixture is formed near spark plug, whereas the leftover volume is occupied only by air. Like in CI engine, the power can be adjusted by controlling the amount of injected fuel. A global lean combustion is allowed with a BSFC reduction at partial loads (up to 40%) and an improved control of the emissions. The goodness of the stratified mixture formation depends mainly on the combustion chamber shape piston surface in particular), the injector position with the connected spray direction, the injection characteristics (rail pressure, injector type, number of holes, etc.) and the in-cylinder fluid motion.

However, stratified direct injection is not yet commonly implemented in DISI engine, due to difficult implementation and control: homogeneous direct injection layout is the current best trade-off between engine performance enhancement and implementation issues [28-31].

2.4 References

[1]   Catania, A. E., Misul, D., Spessa, E., & Martorana, G. (2000). Conversion of a multivalve gasoline engine to run on CNG (No. 2000-01-0673). SAE Technical Paper.

[2]   Middleton, A., Neumann, B., & Khatri, D. S. (2007). Natural Gas Injection System for Buses and Trucks-Potential to Achieve Future Performance and Emission Norms (No. 2007-26-026). SAE Technical Paper.

[3]   Hodgman, C. D. (1951). Handbook of chemistry and physics (Vol. 71, No.3, p. 246). LW.

[4]   International Organization for Standardization. (2013). Gas cylinders -- High pressure cylinders for the on-board storage of natural gas as a fuel for automotive vehicles (ISO 11439:2013).

[5]   International Organization for Standardization. (2015). Road vehicles -- Compressed natural gas (CNG) fuel system components -- Part 1: General requirements and definitions (ISO 15500-1:2015).

[6]   d'Ambrosio, S., Spessa, E., Vassallo, A., Ferrera, M., & Peletto, C. (2006). Experimental investigation of fuel consumption, exhaust emissions and heat release of a small-displacement turbocharged CNG engine (No. 2006-01-0049). SAE Technical Paper.

[7]   Baratta, M., Misul, D., Spessa, E., Gazzilli, G., & Gerini, A. (2012, May). Fluid-dynamic characterization of a CNG injection system. In ASME 2012 Internal Combustion Engine Division Spring Technical Conference (pp. 829-836). American Society of Mechanical Engineers.

[8]   Thipse, S. S., Sonawane, S. B., FD'Souza, A., Rairikar, S. D., Kavathekar, K. K., & Marathe, N. V. (2015). Injection Strategies,

Optimization and Simulation Techniques on DI CNG Technology (No. 2015-26-0046). SAE Technical Paper.

[9]   Choi, M., Lee, S., & Park, S. (2015). Numerical and experimental study of gaseous fuel injection for CNG direct injection. Fuel, 140, 693-700.

[10]   Middleton, A., Neumann, B., & Khatri, D. S. (2008). Development of dedicated cng engine with multipoint gas injection system (No. 2008-28-0014). SAE Technical Paper.

[11]   McCormick, R. L., Graboski, M. S., Alleman, T., Herring, A. M., & Nelson, P. (1999). In-use emissions from natural gas fueled heavy-duty vehicles (No. 1999-01-1507). SAE Technical Paper.

[12]   Hu, Q., Wu, S. F., Lai, M. C., Stottler, S., & Raghupathi, R. (1999). Prediction of pressure fluctuations inside an automotive fuel rail system (No. 1999-01-0561). SAE Technical Paper.

[13]   Lino, P., Maione, B., & Rizzo, A. (2007). Nonlinear modelling and control of a common rail injection system for diesel engines. Applied mathematical modelling, 31(9), 1770-1784.

[14]   Mulemane, A., Han, J. S., Lu, P. H., Yoon, S. J., & Lai, M. C. (2004). Modeling dynamic behavior of diesel fuel injection systems (No. 2004-01-0536). SAE Technical Paper.

[15]   Chiavola, O., & Giulianelli, P. (2001). Modelling and simulation of common rail systems (No. 2001-01-3183). SAE Technical Paper.

[16]   Seykens, X. L. J., Somers, L. M. T., & Baert, R. S. G. (2004). Modelling of common rail fuel injection system and influence of fluid properties on injection process. Proceedings of VAFSEP, 6-9.

[17]   Lino, P., Maione, B., & Amorese, C. (2008). Modelling and predictive control of a new injection system for compressed natural gas engines. Control Engineering Practice, 16(10), 1216-1230.

[18]   Misul, D. A., Baratta, M., & Kheshtinejad, H. (2014). Fluid-dynamic modeling and advanced control strategies for a gaseous-fuel injection system (No. 2014-01-1096). SAE Technical Paper.

[19]   Laurenzano, D. (2014). Sviluppo di un modello AMESim per la simulazione di un sistema di iniezione a gas naturale con valvola riduttrice elettronica e confronto con le prestazioni di un riduttore meccanico (MSc Thesis, Politecnico di Torino)

[20]   Heywood, J. B. (1988). Internal combustion engine fundamentals (Vol. 930). New York: Mcgraw-hill.

[21]   Tilagone, R., Venturi, S., & Monnier, G. (2006). Natural gas-an environmentally friendly fuel for urban vehicles: the smart demonstrator approach. Oil & gas science and technology, 61(1), 155-164.

[22]   Kalam, M. A., & Masjuki, H. H. (2011). An experimental investigation of high performance natural gas engine with direct injection. Energy, 36(5), 3563-3571.

[23]   Ji, S., Lan, X., Cheng, Y., Zhao, X., Li, X., & Wang, F. (2016). Cyclic variation of large-bore multi point injection engine fuelled by natural gas with different types of injection systems. Applied Thermal Engineering, 102, 1241-1249.

[24]   Dickinson, P., & Shenton, A. T. (2009). Dynamic calibration of fuelling in the PFI SI engine. Control Engineering Practice, 17(1), 26-38.

[25]   Mathur, H. B., & Soni, S. L. (1999). Development of timed manifold injection system for compressed natural gas (cng) operation of spark ignition engine (No. 990005). SAE Technical Paper.

[26]   Kheshtinejad, H., Baratta, M., Laurenzano, D., Maino, C., & Misul, D. A. (2018). Investigation into the Potentials of a Dedicated Multi-Point Injection System for a production NG Single-Point Heavy-Duty Engine. SAE International Journal of Engines, 11(2018-01-9275).

[27]   Yamato, T., Sekino, H., Ninomiya, T., & Hayashida, M. (2001). Stratification of in-cylinder mixture distributions by tuned port injection in a 4-valve SI gas engine (No. 2001-01-0610). SAE Technical Paper.

[28]   Baratta, M., Catania, A. E., Spessa, E., Herrmann, L., & Roessler, K. (2008). Multi-dimensional modeling of direct natural-gas injection and mixture formation in a stratified-charge SI engine with centrally mounted injector. SAE International Journal of Engines, 1(2008-01-0975), 607-626.

[29]   Shiga, S., Ozone, S., Machacon, H. T. C., Karasawa, T., Nakamura, H., Ueda, T., ... & Kono, M. (2002). A study of the combustion and emission characteristics of compressed-natural-gas direct-injection stratified combustion using a rapid-compression-machine. Combustion and Flame, 129(1-2), 1-10.

[30]   Baratta, M., & Rapetto, N. (2014). Fluid-dynamic and numerical aspects in the simulation of direct CNG injection in spark-ignition engines. Computers & Fluids, 103, 215-233.

[31]   Boretti, A., Lappas, P., Zhang, B., & Mazlan, S. K. (2013). CNG Fueling Strategies for Commercial Vehicles Engines-A Literature Review (No. 2013-01-2812). SAE Technical Paper.

3 Modelling of pressure reducing valve for CNG injection system behavior prediction

3.1 Introduction

Engine performance and engine out emissions are strictly correlated with mixture formation goodness. Therefore, the actual estimation of the quantity of injected fuel is a key point for the engine control system [1]. The injected mass flow rate is constant for a given rail pressure for CNG injection system, because the pressure ratio across the injector is always kept lower than critical expansion ratio. The injected fuel is hence controlled by varying the ET. Injection system dynamic is affected by changing in the feeding pressure, as highlighted by different research activities [2, 3], and for that reason, the engine control system should be designed considering the pressure waves developing in the rail [4, 5]. For common fuel ICE, this specific goal has been currently solved by adopting electro-hydraulic valves [5], highlighting the need of improved control strategies for CNG injection system [6]. CNG injection system modelling is indeed a common goal for recent research activities,

adopting common methodologies regularly adopted for DI and SI ones. The characterization of the dynamic of the feeding system has to be characterized as a function of the engine design and different operating conditions in order to find the best control strategies. Experimental tests have to be carried out in order to estimate the system dynamic but, considering the large number of operating parameters that affects the system behavior and taking into consideration the thermo-dynamic, the mechanics and the control strategies of the fueling equipment [5-9], simulations are typically performed, with well-known commercial codes, to support system design. Simulation analysis points out the effects of the totality of injection system parameters and allows estimating the consequence of different configuration or control strategies. This is a well-established practice as shown in [10], in which the effects of commons rail, valves, pipelines, high pressure pump and a diaphragm on a gasoline injection system were simulated, giving relevant indication for the system design. Furthermore, the experimental data were used for the numerical model validation. In [11], a new CNG common rail injection system was modeled and a model-based predictive control was tested: the ECU was able to adjust the pressure of injection by controlling an electro-valve feeding the rail. The electro-valve was tested in order to bypass the limits of the mechanical-based CNG injection system by smoothing the pressure waves in the rail, thus improving the injection phase. In [6, 12] accurate fluid-dynamic simulation of CNG injection systems were carried out, analyzing the relationship between the injection system characteristics and its behavior and between the pressure dynamic in the rail and the injection events. A connection between the dynamic caused by the injection events and the pressure waves in the rail produced by the pressure reducing valve was presented. A rail pressure reduction during the injection window causes a mismatch between the actual injected fuel and the ECU estimation: the global mean rail pressure has been shown to be higher than the mean value during the injection window. Even though a deep characterization of the injection system is introduced, a poor modelling of the pressure reducing valve leads to misleading results.

The present section shows a thorough mechanics and fluid-dynamic modelling of a CNG injection system for a two-cylinder ICE with an accurate characterization of the pressure reducing valve, focusing on the dynamic behavior of the equipment during a driving cycle. The engine out emissions and engine performance and the cylinder-to-cylinder variability could be affected by the air-to-fuel ratio non-homogeneity between the two cylinders caused by mismatch in the injected fuel mass due to pressure waves inside the

rail. Therefore, an accurate modelling of the pressure reducing valve has been made, considering its effects on the injection equipment behavior. Experimental data collected at the test bench has been handled to validate the 0D-1D numerical model and to understand the system dynamic during transient conditions.

3.2 Experimental set-up

Experimental tests have been performed at CRF (Centro Ricerche Fiat, Strada Torino, 50 - 10043 Orbassano (TO), Italy) and at Metatronix (Via Olivetti Adriano, 26 - 10040 Volvera (TO), Italy) laboratories and test bench layout have been designed to reproduce the on-board fueling system of a two-cylinder engine. Therefore, the system is made up of a high-pressure tank, in which the CNG is stored at a pressure ranging around 200 bar, connected to the injection system by means of a pressure reducing valve which lowers the natural gas pressure to approximately 9 bar [12]. The characteristics of the injection system and the engine it supplies are listed in table 3.1.

Table 3.1: Engine and injections system characteristics

Engine specifications	Value
Bore (mm)	80.5
Stroke (mm)	80
Compression ratio	10
Cylinder number	2
Displacement (cm^3)	875
Injector Manufacturer	Robert Bosch GmbH
Maximum injector pressure (barA)	12
Regulator Manufacturer	Metatronix s.r.l.
Injection system type	MPI

The measurement equipment is composed by: high-frequency pressure transducers located upstream and downstream from the regulator and in the fuel rail, thermocouples placed upstream and downstream from the regulator and a mass flow meter. The injectors are controlled by the ECU in order to guarantee a stoichiometric mixture. The injection timing and phasing mapped in the ECU are corrected according to the average rail pressure and temperature as shown in [2], introducing anyhow a mismatch between the ECU estimation and the actual air-to-fuel ratio [12]. In order to characterize the injection system four different experimental tests have been performed:

- **Static run:** in order to estimate the nozzle cross section area and the discharge coefficient, the injector has been kept wide open and the rail pressure has been set at a constant value. The test has been carried out in order to provide the model with the specification to well define the injector.
- **Single injection:** the system free response has been analyzed by actuating a single injection at the beginning of the test. With this case the natural frequencies and the damping factor of the injection system have been determined.
- **Steady state points:** the injection system has been tested under steady state conditions in order to reproduce the behavior of the equipment during actual engine operating conditions. The ten different steady state points corresponding to different engine loads and speeds are listed in Table 3.2.
- **Driving cycle:** the experimental test reproduces on the pneumatic test bench the real on-board driving cycle. In order to replicate the actual driving conditions, the ETS are consequently adjusted. The driving cycle case has been carried out in order to test the goodness of the global numerical model of the injection system.

The pressure sampling frequency for the driving cycle test has been set to 5 Hz whereas for the other cases it has been regulated to 3.2 kHz. Finally, CNG has been replaced with air and the injectors discharged the fluid in open environment ($p_{env} \cong 1$bar).

Table 3.2: Steady state cases

Case number	Speed [rpm]	bmep [bar]	ET [µs]
1	1100	1	4000
2	1100	3	5000
3	1100	6	8000
4	2300	2	4000
5	2300	4	6000
6	2300	12	14000
7	3000	1	4000
8	3000	3	5300
9	3000	7.5	10000
10	3000	12	14000

3.3 CNG injection system model

3.3.1 AMESim 0D-1D: review of the theory

The simulation activity was carried out by means of the AMESim software, a numerical tool developed by LMS International, and in particular with the "Pneumatic Library". It solves the 1D compressible Navier-Stokes equations for the fluid flow. A detail explanation of the implemented equations can be found in the software manual [13].

3.3.2 Model description

The CNG injection system has hence been modeled within the AMESim environment [14]. The model is shown in Fig. 1. It has been built considering the technical drawings of the injection system; therefore, all the geometric

characteristics have been introduced (the surface roughness of the pipes has to be meticulously set in order to estimate the distributed losses). The radius, joints and connections have been carefully designed to correctly implement the concentrate losses.
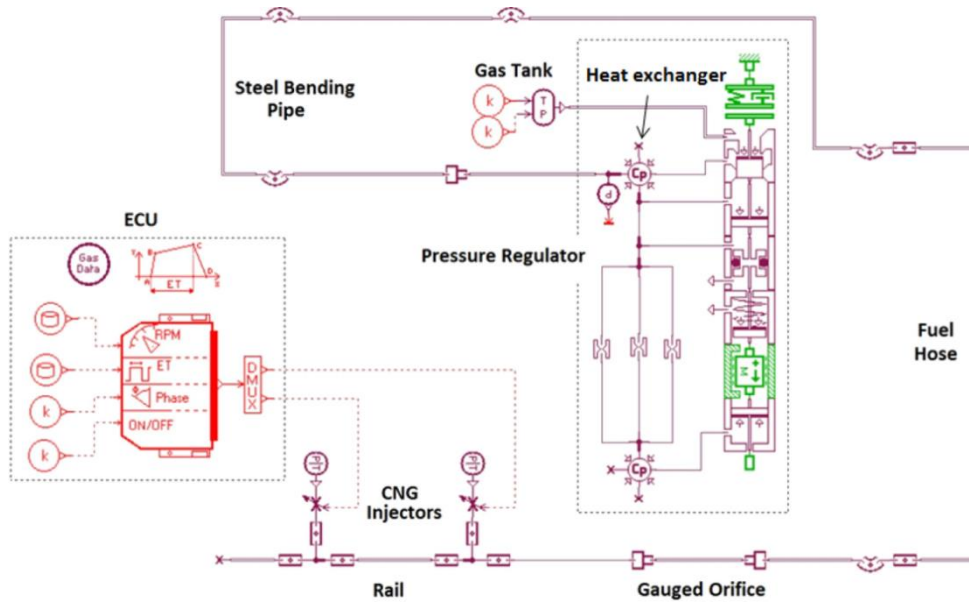
Figure 3.1: AMESim model of the considered injection system [14]

The high-pressure line is replaced by imposed pressure and temperature boundary conditions (the experimental data, acquired at the regulator inlet, have been imposed). The AMESim model has been hence built as follows: the tank boundary condition has been introduced at the inlet of the pressure reducing valve; the pressure regulator models will be further explained. The low-pressure line has been added downstream the reducing valve, presenting the actual models of the pipes connected with the rail. The two injectors, which have been inserted in the rail, discharge the fluid in the environment ($p_{env} \cong 1$ bar, $T_{env} \cong 293$ K); each injector has been modeled with a gauged orifice and a pipe to reproduce the detailed valve fluid-dynamics and its effect on the injection system behavior. The lumped element model of the injector has been calibrated matching the experimental data of the "static run" and "steady state points" cases, as shown in [6]. The injectors are governed by the ECU driver: the driver reproduces the engine control, as shown in Figure 3.1, by adjusting the ET and the injections phasing considering the simulated engine speed. The opening dynamics of the injector has to be properly modeled and correlated to the ET command in order to define the lift profile. The opening profile can be

divided in three phases: the opening ramp, the maximum lift and the closing ramp. The first part of the stroke depends on the mechanics characteristics of the injector and on the coil command, whereas the second and the third ones depend only on the injector characteristics. The energizing time only manages the sum of the first and the second period times. Therefore, in order to guarantee the injected fuel target, the ET is modified. The correction factors have been experimentally calculated as a function of the rail pressure and temperature and have been introduced in the ECU driver.

In [6, 12], worth fluid-dynamic simulations of a CNG injection system were carried out, showing the effects of the injection events on the dynamic behavior of the system. The research activities deepen the study in the effects of the injection system geometry on the rail pressure dynamic, underestimating the pressure regulator dynamic. In the present study, a thorough modelling of the pressure reducing valve has been developed thanks to the experimentally acquired data, and the effects of the valve on the behavior of the system and on the injected fuel mass have been carefully analyzed. The injection system dynamic is indeed strictly correlated to the pressure regulator behavior [14].

3.4 Pressure regulator modelling

3.4.1 First release of the pressure regulator

The first release of the pressure regulator (Fig. 3.2) is a modification of the model presented in [12]. The model of the valve has been designed considering the characteristic of the actual valve, the Metatron Meta M ND1single stage piston pressure regulator [15], deriving the main model parameters from the technical drawings. The model has to be minor adjusted, depending on the tolerance, in order to obtain a correct valve modelling: the first release, as the other ones, has been tuned with a design of experiment (DOE).
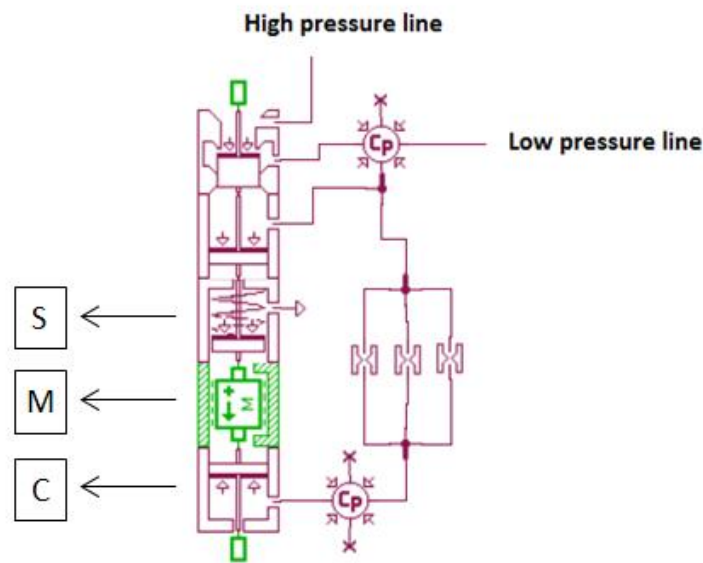
Figure 3.2: First release of the pressure regulator [14]

The inlet port of the pressure regulator is connected with the high-pressure line, receiving the CNG from the tank, whereas the outlet port is connected with the low-pressure line. The valve is modeled by using lumper-parameter AMESim objects that represent the actual pressure regulator parts: the model embeds the spring element (S), the equivalent mass of the piston (M) and the control chamber (C) where the pressure from the low-pressure line is received through a pilot line. The three elements have been modeled considering the actual characteristics of the real pressure regulator valve: "S" box has been calibrated by adopting stiffness and preload of the actual spring; piston mass has been used to calibrate "M" box and control chamber volume to calibrate "C" one. Unfortunately, few characteristics of the actual valve are affected by uncertainty and hence a calibration process has to be performed.

The piston equilibrium is described by Equation 2.5. It depends on the forces generated by the high-pressure line and the low-pressure line acting on the upper surface (unbalanced pressure regulator), on the spring load, on the force generated by the low-pressure line in the control chamber and on the inertia. The rail pressure is affected by the tank condition, as shown in Chapter 2.2 and remarked in Figure 3.3, because of the lack of a pilot line for the high-pressure line. The tank pressure decrease, due to engine functioning, generates a reduction in the rail pressure, reflecting into a growth of the energizing time.
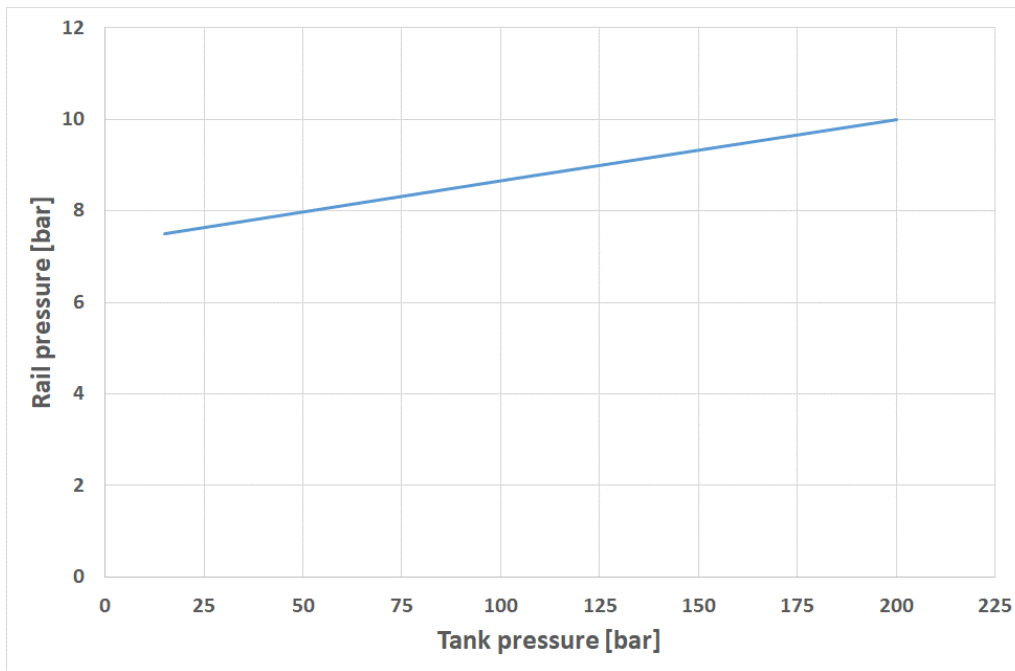
Figure 3.3: Effect of the tank condition on the rail pressure

The main issue of the above-mentioned release of the pressure regulator is the lack of lumped parameter elements connected with friction which discriminates the real valve.

3.4.2 Second release of the pressure regulator

The pressure drop phenomenon (explained in Chapter 2.2) has mainly to be ascribed to the spring stiffness (and non-linearity) as well as to the frictions between the moving parts and the seat. Therefore, the first release is not able to properly model the pressure regulator behavior.

The pressure downstream the regulator is a function of the fuel flow rate flowing through the valve for a given pressure level of the high-pressure line (tank). As the valve starts to open the passage between the high-pressure line and the low-pressure line, there is a rapid pressure drop called "Cracking drop" because of the valve and spool resilience and misalignments between the piston and the seat. By increasing the mass flow rate with a larger displacement of the valve piston, the pressure drop is leveled: this phase is called "Dynamic drop". It is a function of the spring characteristics as well as to the frictions that appear between the moving parts and the seat. The second release has been

developed by the first one, introducing additional elements to proper reproduce the pressure drop phenomena (Fig. 3.4).
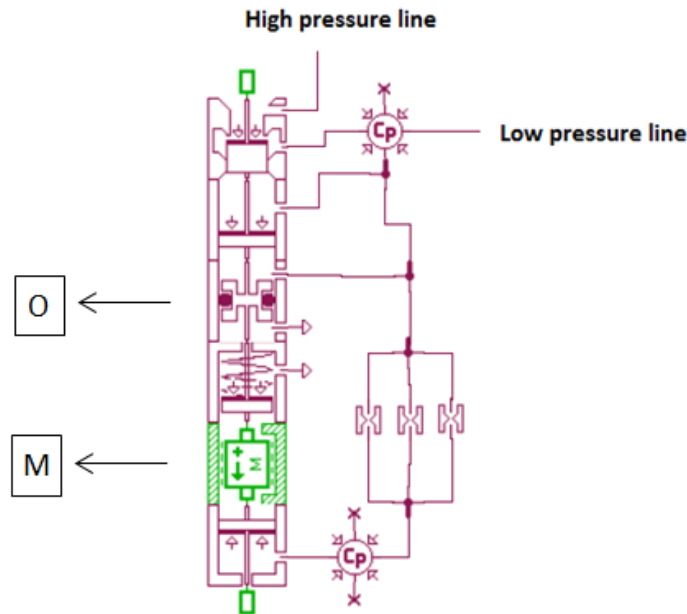
Figure 3.4: Second release of the pressure regulator [14]

The element prescribed to introduce the inertial effect in the first release has been changed with a different lumped element (M) that represents both the equivalent mass of the piston (inertial effects) and the static and dynamic friction between the moving parts and the seat. The above-mentioned lumped element was still not able to reproduce the "sealing friction": the "sealing O-ring" element (O) has been hence introduced to fully reproduce the pressure drop phenomena. Figure 3.5 shows the comparison between the experimental data and the simulation data of the two releases during the functioning at a giving tank pressure for different fuel flow rate. The simulation results have been acquired for both releases by matching the valve model to the previously calibrated line model. The differences between the simulation results are definitely to be ascribed to the differences between the first and the second release. The results of the second release (green triangles) match adequately the experimental data (blue diamonds), reproducing correctly the dynamic drop, whereas the first release (red square) is not able to model a proper pressure drop. The rail pressure reduction that occurs in the first release simulation has indeed to be ascribed to the spring stiffness. Both the models were anyhow not able to fully reproduce the cracking drop phenomenon: the valve and spool

resilience that play a role during the closing and opening phases have not been still introduced.
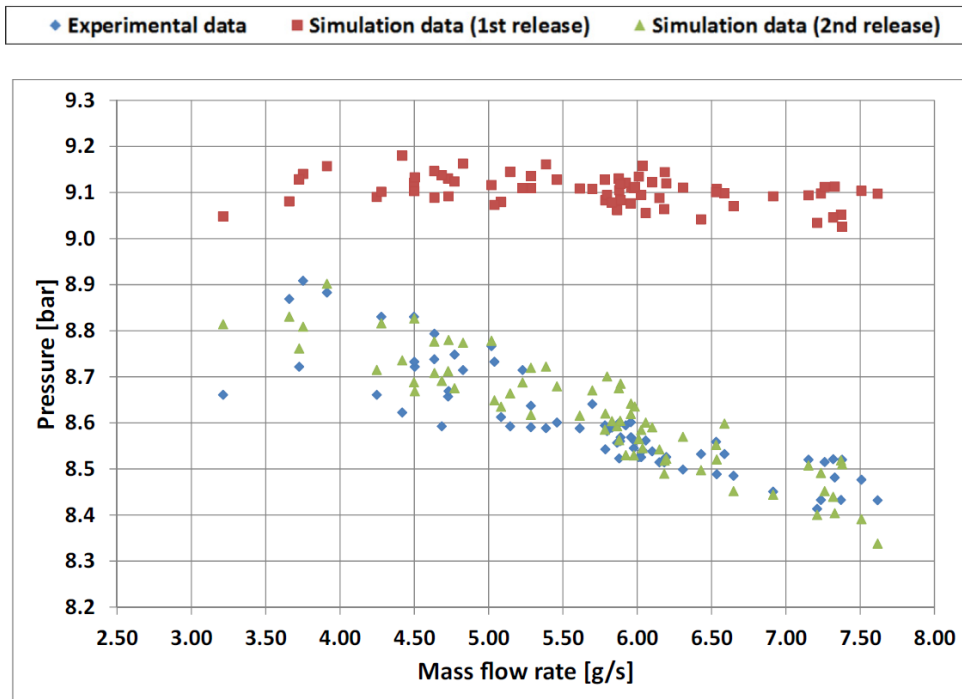
Figure 3.5: Pressure drop phenomenon: comparison between the experimental data and the simulation data of the 1st and 2nd release [14]

3.4.3 Third release of the pressure regulator

The previous releases were not able to reproduce the effect of the piston shim which affects the pressure regulator behavior during the opening and closing phases. The shim is positioned on the closing surface of the piston in order to dump the impact of the piston against the seat during its closure. The shim was made by a plastic material, introducing an elastic and dumping behavior to the spool during the closure. Unfortunately, the plastic pad accounts for an imperfect sealing and thus for leakages from the high-pressure line to the low-pressure ones during the closing phase. During engine cut-off phases the pressure regulator should indeed be technically closed, whereas a rail pressure buildup takes place. In order to numerically reproduce the shim behavior, a new lumped parameter element was added in the third release (Figure 3.6). The spool shim element (P) carries out an elastic and dumping effect only during the contact between the piston and its seat.
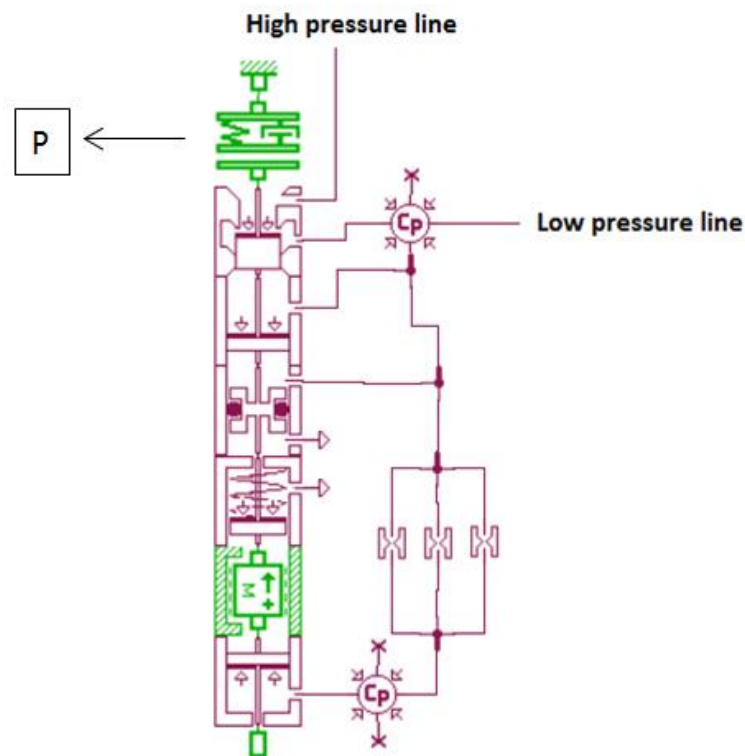
Figure 3.6: Third release of the pressure regulator [14]

3.4.1 Calibration of the pressure regulator models

The three pressure regulator models required a calibration phase. Indeed, some of the regulator parameters like the mass, the spring stiffness, the geometry and the surface roughness have been acquired by the technical drawings of the Metatron Meta M ND1and have been carried out unchanged for all the models. The set of parameters implemented in the three releases is listed in Table 3.3. The supplementary regulator parameters' values were not available; therefore, they have been estimated considering a starting value obtained from the own commercial regulator analyzed. These values have been calibrated by using a fraction factorial DOE on the single shot and steady state cases, by targeting the rail pressure. Simulated rail pressure has been compared with experimental one and RMS error has been calculated. The set of parameters which minimizes the error has been selected as the optimum one.

The DOE has been carried out for all the pressure regulator releases and the parameters' ranges are shown in Table 3.3. The best values have hence been found on the basis of the experimental data. Moreover, the parameters

optimized for a previous release have been kept unchanged for the subsequent releases and they are used for all the four tests.

Table 3.3: Parameters of the three releases

Release model	Parameter	Starting value	Range	Optimum
All	Mass [g]	25	-	-
	Spring stiffness [N/mm]	30	-	-
	Surface roughness [mm]	5e-4	-	-
1st	Spring force at zero displacement [N]	680	630÷730	710
	Control chamber Volume 1 [cc]	15	10÷40	30
	Control chamber Volume 2 [cc]	15	10÷40	20
2nd	Dynamic friction pressure gradient [N/bar]	0.1	0÷100	10
	Dynamic to stiction friction coefficient [-]	1	0÷10	2
	Stick displacement threshold [mm]	0.2	0÷5	0.1
3rd	Maximum piston displacement for which the shim is active [mm]	0	0÷1	4e-5

3.5 Results and simulation analysis

3.5.1 Single injection test

With the single injection test the system free response has been analyzed. With this case the natural frequencies and the damping factor of the injection system

have been determined. Single injection events with different energizing time have been carried out in order to reproduce the free response of the injection system by analyzing the pressure waves in the rail and downstream the pressure reducing valve. The single injection test as well as the steady state and driving cycle tests have been simulated with each pressure regulator model. Figure 3.7 shows the comparison between the experimental results and the simulation data for two different single injection tests corresponding to a small ET and a larger one (3.5 times). The experimental pressures downstream the pressure regulator (Figure 3.7 a, c) and the rail ones (Figure 3.7 b, d) have been compared with the numerical models, considering the three releases. The blue traces represent the experimental data, the red, green and purple traces represent the first, second and third releases respectively, while the light blue trace represents the injector voltage.

The numerical model with the first release of the pressure regulator is not able to reproduce the experimental behavior of the actual pressure reducing valve. Indeed, after the injection event (its command corresponds to the peak in the light blue line) the rapid buildup of the pressure downstream the valve as well as of the rail one has to be ascribed to the lack of friction lumped parameter elements. Although the first release is not able to properly describe the experimental event, it's correctly design (the same for pipes, rail and injectors): the single-sided spectrum of the simulated pressure waves are comparable with experimental ones except for response at reduced low frequencies (Figure 3.8). The inertial and stiffness characteristics have been thus properly evaluated but frictions have to be implemented. In the second release the friction element has been added in order to enhance the pressure regulator modelling. The dynamic dumping effect and the stick-slip phenomenon have been introduced by adding the sealing O-ring element. The promptness of the second release (green lines) is lower than the first one, leading to better estimation of the pressure regulator (Figures 3.7 and 3.8). Still the numerical model produces a mismatch in the rapidity of the low-pressure line pressure build up. The valve and spool resilience and the misalignments between the piston and the seat are responsible of leakages between the high-pressure line and the low pressure one, leading to a pressure increase after the injection event and to the so called "cracking drop". The third release with the spool shim element is correctly able to reproduce the pressure regulator dynamic behavior. The lumped parameter element "P" is indeed able to introduce a dumping and elastic effect only in the first part of the displacement of the spool.

Two different ETs have been shown to estimate the different behavior of the system. The second single injection case (Figure 3.7 c, d) is characterized by a long ET (ET=14000 µs), implying a higher pressure drop in the low-pressure line because of a higher injected fuel mass with respect to the first single injection case (Figure 3.7 a, b). The second and third releases appear to have a different behavior considering a short ET and a long one. For a longer ET duration, the higher rail pressure decrease leads to a higher spool displacement, thus to a greater mass flow rate flowing through the pressure regulator. An increased spool displacement neglects the effect of the shim. As a matter of fact, the shim introduces the elastic and dumping effects only for reduced displacements (4e-5 mm); the two releases perform hence the same behavior for generous piston displacement. The third release shows considerable differences with respect to the previous one during the opening and closure phases.
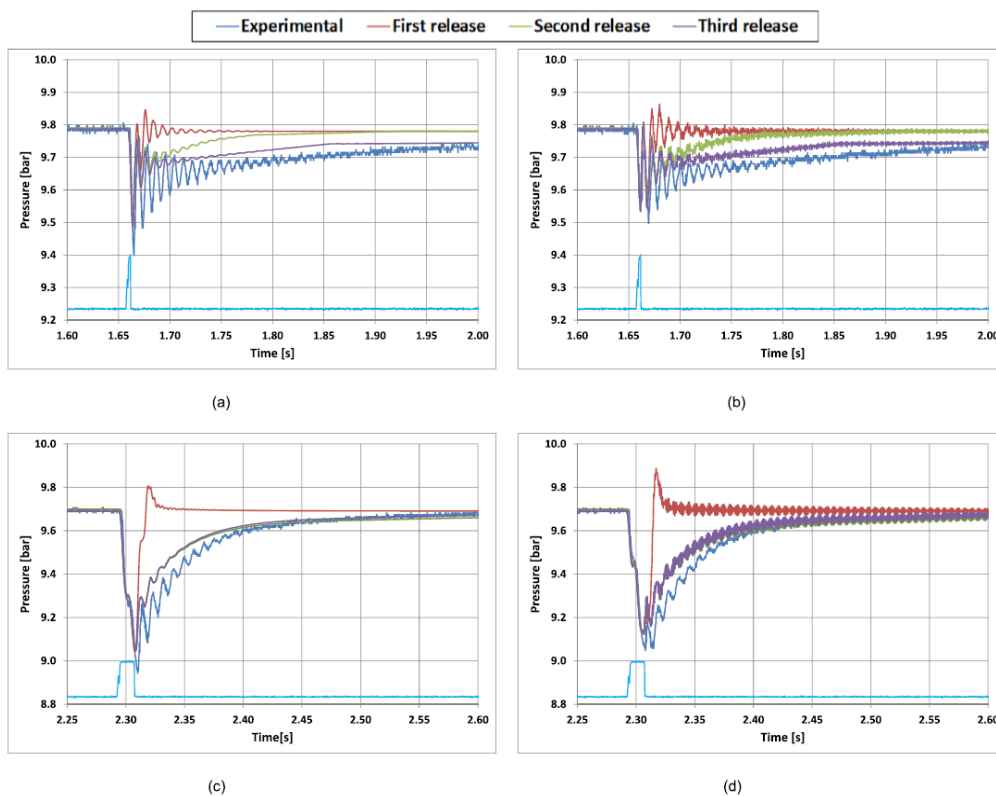
Figure 3.7: Comparison between experimental data and simulation results at the regulator downstream (a, c) and in the pressure rail (b, d) for two single injection tests: (a, b) ET=4000 µs, (c, d) ET=14000 µs. [14]
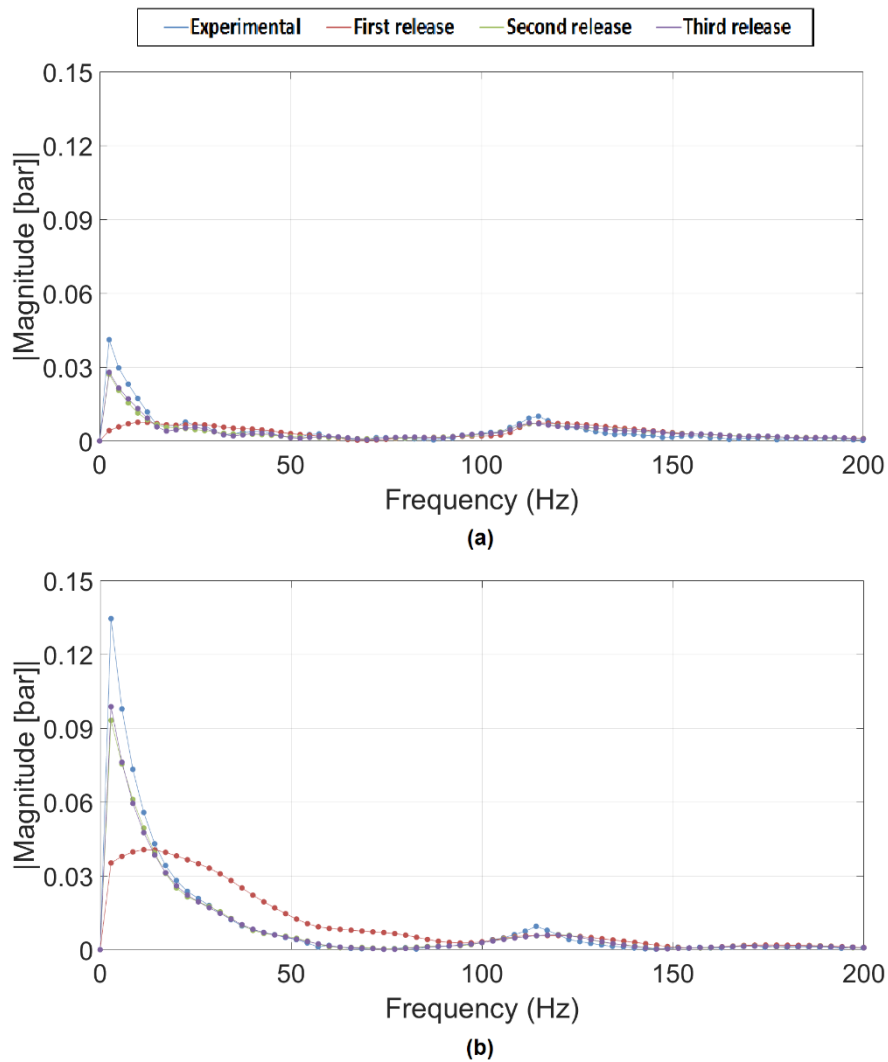
Figure 3.8: Comparison of single-sided spectrum between experimental data and simulation results for two single injection tests: (a) ET=4000 μs, (b) ET=14000 μs. [14]

3.5.2 Steady state cases

The steady state cases reproduce the injection system functioning during different engine loads and speeds (Table 3.2). The low-pressure line model has been designed considering [12], in which a 0D-1D numerical model of a CNG injection system correctly reproduces the pressure waves in the rail. The aim of the research activity presented in [12] is the evaluation of the effect of the engine operating conditions connected with different energizing times on the

mismatch between the injected fuel mass and the ECU calculated one. The numerical model assesses the optimal geometric characteristic of the injection system, adopting a pressure regulator model similar to the above-mentioned first release. Unfortunately, the pressure reducing valve model needs a point by point calibration in order to properly reproduce the behavior of the pressure regulator for different conditions. Instead, the purpose of the research activity is the modelling of a pressure regulator and an injection system with the capability to proper reproduce the actual valve behavior. In particular, the third release of the valve as well as the injection system model has the aim to correctly simulate the actual system response and behavior during all the possible operating conditions. Anyhow, the calibrated version of the three releases has been used during the simulation analysis of the experimental tests to proper define the origins of the dynamic effects.

The case at the lowest engine speed and ET (case 1 Table 3.2) and the one at highest (case 10 Table 3.2) have been previously analyzed to recognize the differences between the three releases: the experimental and simulated rail pressures have been compared (Figure 3.9). The first case (Figure 3.9 a) represents a partial load case with a low engine speed and reduced torque. The two injections (lilac and light blue lines) are short (reduced ET) and distant (low engine speed) leading to a slow dynamic response of the pressure inside the rail. Similar results were presented for the single injection case, leading to a correct estimation of the second and third release; as a matter of fact, they are overlapped. The two releases reproduce the main pressure wave inside the rail in both the steady state cases, whereas the first one is not able to reproduce the carrier (main pressure wave) and it also misleads the average pressure due to the lack of dumping factors. In Figure 3.9 the error of the first release is well shown.

Figure 3.9: Comparison of the experimental rail pressure and the simulated ones (three releases) for: (a) steady state case 1 and (b) steady state case 10 (Table 3.2) [14]

The second and third releases are always overlapped. As explained in section 3.4.4, the third release is an evolution of the second one: the shared lumped parameter elements include the same specifications. The last release is hence perfectly equal to the second one except for the shim element. During steady state conditions the spool of the pressure regulator is always floating around an average displacement, neglecting the shim effect (it works only during opening and closure phases). The average displacement indeed depends on the mean injected fuel flow rate which is function of the ET and engine speed. The peak-to-peak amplitude of the rail pressure of the model embedding the first release is the larger, showing the inconsistent promptness of the pressure regulator model to the excitements operated by the injection events. The above-mentioned behavior is highlighted by the dynamic response presented in Figure 3.9 b: the steady state case with the faster excitation confirms the need of dumping elements embedded in the pressure regulator model. Finally, the significant mismatch between the simulated average rail pressure of the model with the first release and the experimental one is function of the single calibration of the parameters of the pressure regulator model. As a matter of fact, the pressure regulator model in [12] was point by point calibrated. During this activity, the calibrated parameters listed in Table 3.3 have been kept unchanged. The first release is thus unable to reproduce the cracking drop and pressure drop effects. For the sake of conciseness, the behavior of the last two releases is shown (Figure 3.10) for other three cases.
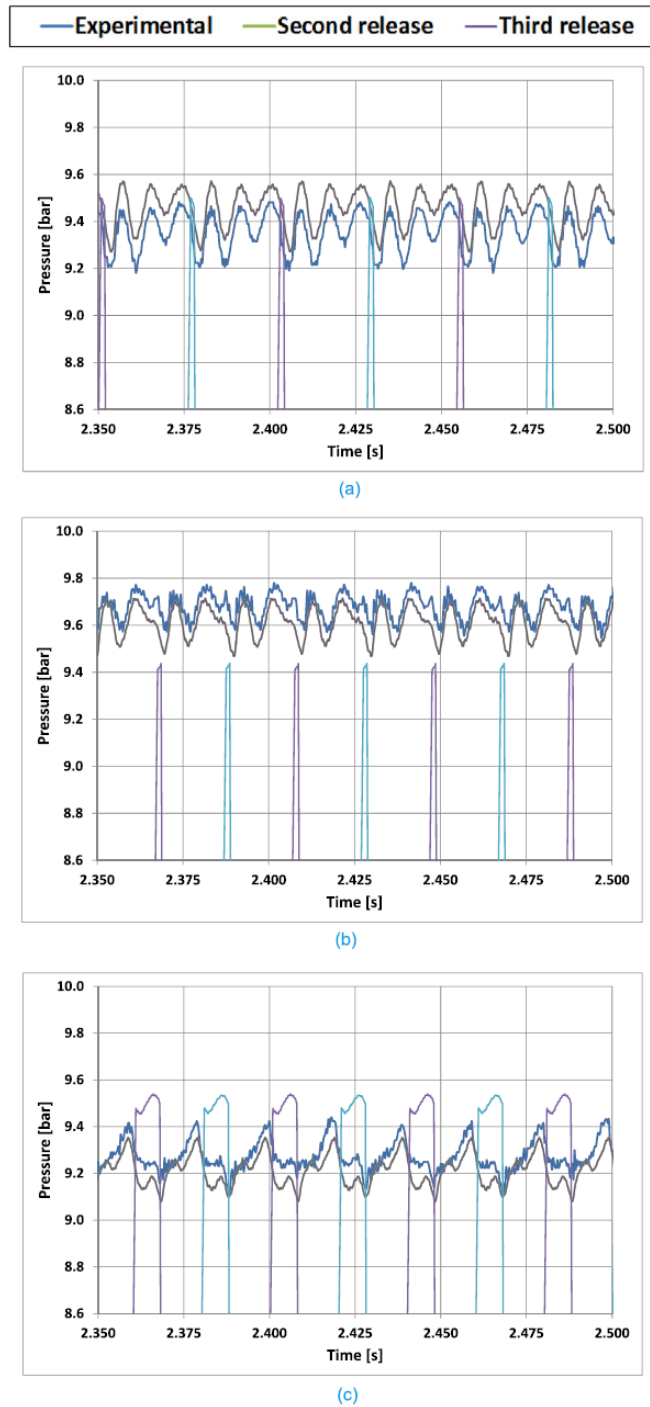
Figure 3.10: Comparison of the experimental rail pressure and the simulated ones
(second and third release) for: (a) steady state case 4, (b) steady state case 7 and (c)
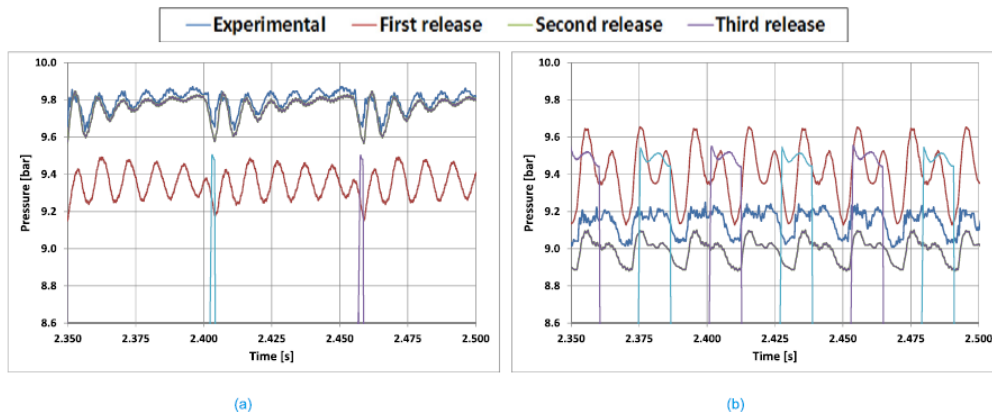steady state case 9 (Table 3.2) [14]

The last two releases demonstrate an adequate accordance with the experimental results for all the steady state cases. Figure 3.10 shows the results obtained by the numerical model compared with the experimental signals for three steady state cases. The first two cases reproduce two operating conditions with different engine speeds (2300 rpm and 3000 rpm respectively) but same ET (4000 μs), whereas the last two work at the same engine speed (3000 rpm) but different ET (4000 μs and 10000 μs respectively). The two releases are able to reproduce the dynamic behavior of the pressure regulator under different excitation and the average pressure of the numerical data in the rail (and hence downstream the pressure reducing valve) is approximately equal to the experimental one for all the cases (the minor differences have to be ascribed to the single calibration).

3.5.3 Driving cycle test

The three pressure regulator releases together with the injection system model have been tested on the so called "Driving cycle" test. This test stresses the feeding system and pressure regulator on all the possible conditions highlighted in Section 2.3. The figure 3.11 displays the comparison between the experimental rail pressure (blue line) and the simulated one (red line) during the first 180 seconds. The sampling frequency used for this test has been reduced to 5 Hz in order to reduce the amount of data and to catch the low frequency dynamic response of the low-pressure line (the high frequency response of the system has been analyzed with the steady state cases). The focus has been set to the dynamic response during the change of injected mass flow rate (dynamic drop) and during the cut-off phases (cracking drop). Considering the time scale of the above-mentioned phenomena (5÷10 s), the selected sampling frequency is acceptable (f_S>>$10f_N$). The experimental analysis was carried out on a test bench reproducing the on-board actuation and the pressure tank decrease. The latter is responsible of the average rail pressure decrease shown both in experimental and simulation data: the Metatron Meta M ND1 is indeed an unbalanced pressure regulator. Figure 3.10a displays the comparison between the experimental data and the results of the numerical model with the first release. The lack of elements introducing the frictions and the shim properties leads to an inaccurate evaluation of the pressure drop phenomena. The correct implementation of the actual valve basic parameters (geometry, mass of the piston, spring stiffness, etc.) brings just to an appropriate simulation of the decrease of the rail pressure because of the vessel emptying. The numerical models with the second and third release (Figure 3.11

b and c respectively) are able to simulate the rail pressure drop due to the introduction of the frictions (consider the time interval from 40 to 50 s). The acceleration phases are correctly simulated by both the last two releases, whereas the cut-off phases (time interval from 55 to 60 s) are well-simulated just by the last one. The pressure buildup in the rail when no injection is performed is caused by the spool shim. With the last element introduced in the third release the dumping effect that occurs during the contact between the piston and its seat has been introduced and thus, the leakages between the tank and the rail have been finally simulated. A focus of the goodness of the third release is shown in Figure 3.12. It is worth observing that the numerical model is able to replicate the pressure drop dynamic and the pressure build up occurring during the cut-off phase, which starts at 126 s. The numerical model has to be finely calibrated so as to deeply analyze the dynamic of the injection system and also to adopt the code in a predictive way. The model with the third release is reliable, as shown in Figures 3.11 and 3.12, and it can be adopted for further analysis.
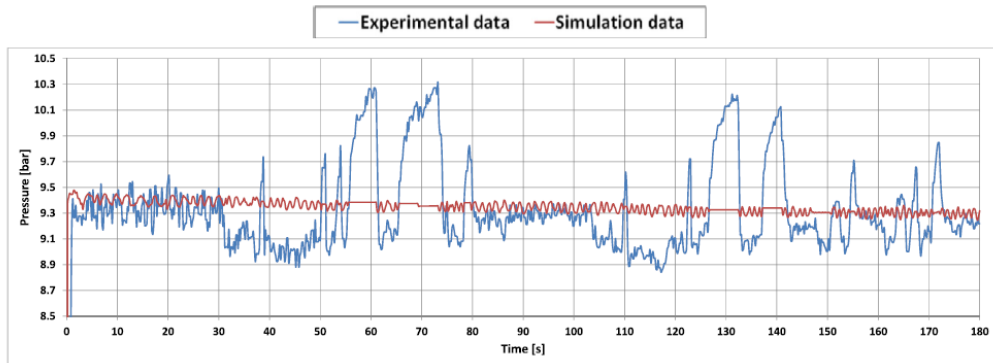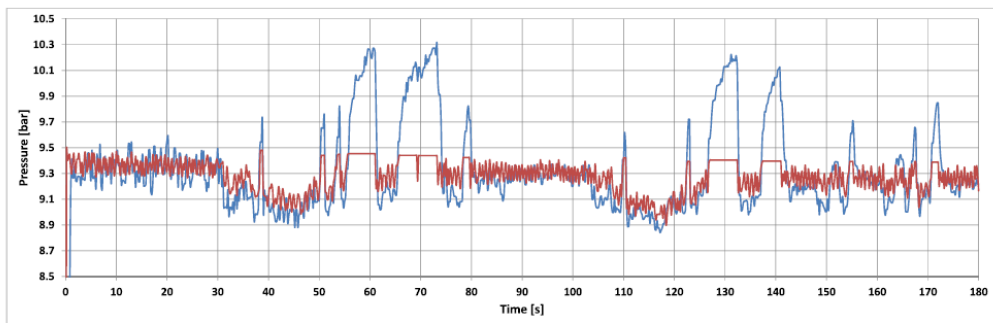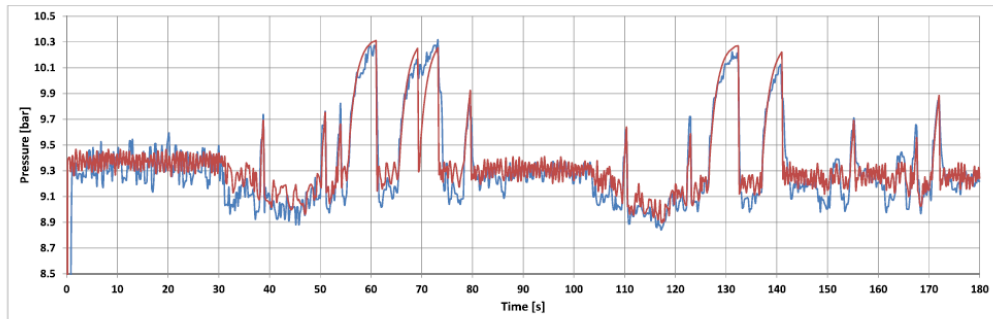
Figure 3.11: Comparison of the experimental rail pressure and the simulated one during the driving cycle: (a) first release, (b) second release and (c) third release [14]
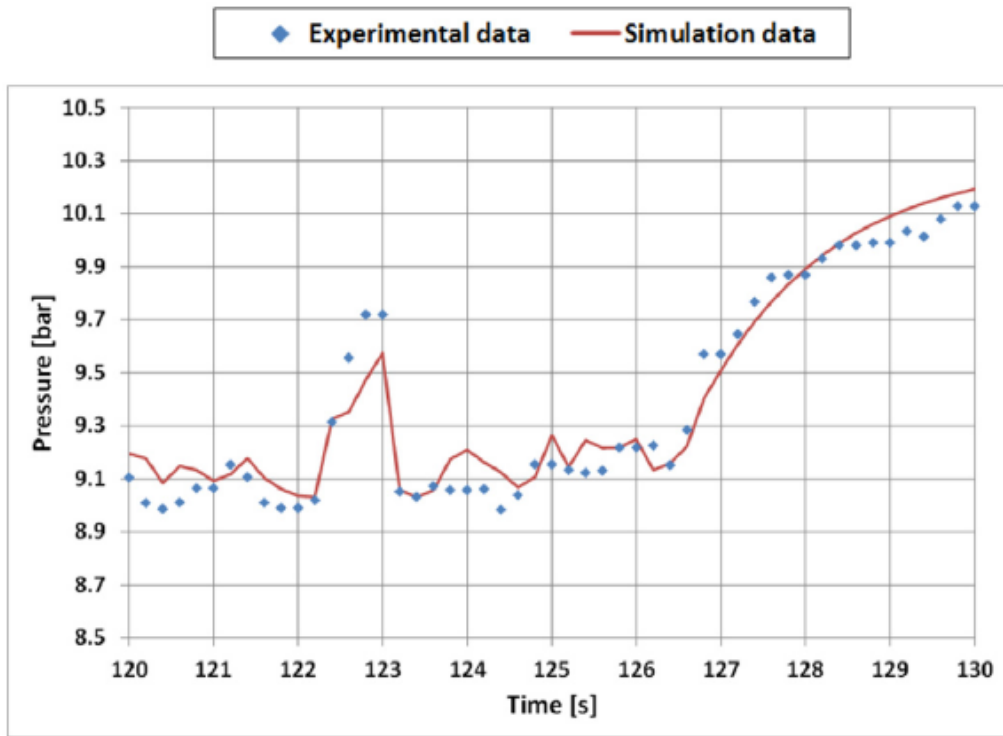
Figure 3.12: Focus of a transient and a cut off phase [14]

3.6 Transient predictive simulation

The driving cycle test shows the high quality of the third release (and its correct calibration) and highlights the needing of analysis under transient conditions. The numerical model of the injection system with the third release of the pressure regulator could be used in a predictive way in order to analyze the system during fast transient conditions. The predictability of the system is due to the unique calibration of the pressure regulator (the point-by-point calibration shown in [12] can't be accepted) and its goodness. Thus, speed transient and load transient simulations have been carried out with the third release (Figure 3.13 and 3.14). The figures show the dynamic of the rail pressure (red line, left hand side y axis) as a function of time, for changing of speed strategy (Figure 3.13) and load strategy (Figure 3.14) (black lines, representing the normalized values). The lilac and light blue lines represent the fuel mass flow rate injected by the two injectors (right hand side y axis). Finally, the injected fuel mass is represented by solid circles (right hand side y axis) and the average rail pressure during the injection window is provided with red squares (left hand side y axis).

For the speed transient simulation, the starting and incoming operating conditions have been selected from the ones evaluated in the steady state cases and the speed ramp has a period of 0.3 s. Figure 3.13a shows the speed transient from case 4 to case 7 and Figure 3.13b displays the transient from case 1 to case 16 (Table 3.2). The speed transient duration is considerably lower with respect to the time constant of the pressure waves in the rail. As a matter of fact, the injection system dynamic rapidly follows the changing of the injection events and swiftly reproduces the dynamic of the main steady state cases. The shapes of the pressure waves before and after the transient phase are indeed identical to the corresponding steady state cases (Fig. 3.10).
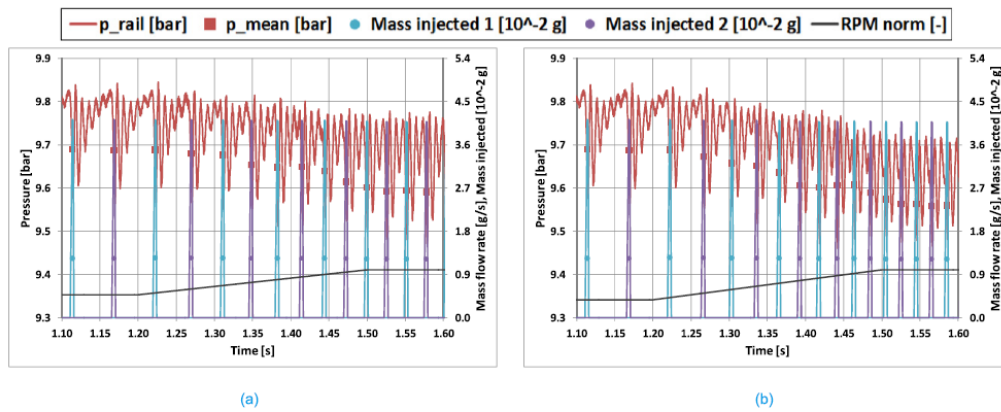
Figure 3.13: Speed transient simulation: (a) from 1100 to 2300 rpm, (b) from 1100 to 3000 rpm (ET=4000 μs) [14]

The rise of the engine speed leads to an increment of the average injected mass flow rate (considering the same ET of the two steady state cases). The reduction of the average rail pressure depends indeed on the pressure drop phenomenon shown in Figure 2.3. During the speed transient local increasing of the average rail pressure during the ET window can occur: the local increase depends on the interaction between the injection excitation, the pressure regulator dynamic and the resulting pressure waves. The occurrence of the injection event and its phasing with respect to the rail instantaneous pressure could lead to a mismatch between the actual injected fuel mass and the ECU evaluated one. More specifically, the ECU estimation of the rail pressure is based on the mean value calculated during the entire period, whereas the pressure drop caused by the injection event implies an average pressure during the ET window lower than the mean one, as shown in [12]. The miscalculation of the ECU estimation of the rail pressure with respect to the experimental one leads to error in the abovementioned steady state cases ranging from 1% to

2.5%. This discrepancy is even more significant for the pressure drop caused by the engine acceleration and the engine efficiency is hence affected by the incorrect air-to-fuel ratio (lean mixture). Thus, numerical model and predictive control strategies have to be actuated in order to prevent irregularities in the mixture formation.

The load transient simulations have been modeled moving from case 9 to case 10 as shown in Figure 3.14 a and from case 7 to case 10 as highlighted in Figure 3.14 b. The ET adjustments have been modeled with a sudden change to reproduce a rapid transition in the engine loads. The figures show the effect of the different injected mass flor rate on the average rail pressure: the pressure drop phenomenon is highlighted in the load transient, in which the distance between the two main injections is the same but the ET windows changes. The response of the injection system is function of the low-pressure line geometry and of the pressure regulator dynamic. It is anyhow rapid, and the injected fuel mass quickly reaches the target value. The misleading of the evaluation of the mass flow rate varies between the 1% for the first load transient (Figure 3.14 a) to 4% for the second one (Figure 3.14 b). Taking into consideration the results of the numerical model under the driving cycle and the transient operating conditions, the predictive model could be adopted in order to verify the effectiveness of suitable control-based strategies under different transient operating conditions.
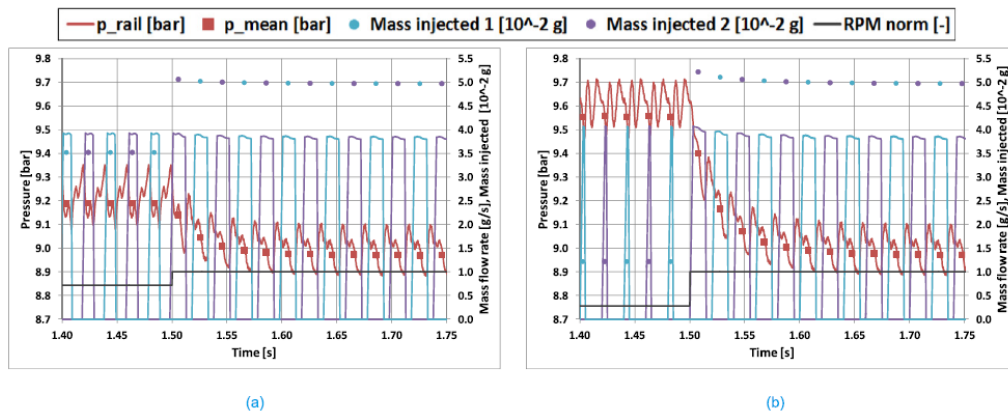
Figure 3.14: Load transient simulation: (a) energizing time changing from 10000 to 14000 μs, (b) from 4000 to 14000 μs (n=3000 rpm) [14]

3.7 Discussion

The research activity is a development of analysis showed in [12], in which a CNG injection system was deeply simulated with a numerical model. The pressure regulator is modeled with a point by point calibration. In this thesis a consisting and predictive modelling of the pressure reducing valve has been achieved, showing the necessity of a proper description of the whole injection system. As matter of fact, a numerical model of the fueling system with three different releases of the reducing valve has been compared to the experimental data in order to show the connections between the dynamic response of the low-pressure line and the elements of the pressure regulator. All the releases are able to reproduce the system natural frequencies due to a proper estimation of the valve inertia and the spring stiffness. The first simplest release is not capable to reproduce the pressure drop effects of the injection system due to a poor design of the model. It is based simply on the parameters of the technical drawings, neglecting all the friction elements. The actual pressure regulator valve is better reproduced with the second and third release: the dumping effects have been reproduced with the "O-rings" lumped parameter in former and the piston shim resilience and the misalignments between the piston and the seat have been added in the latter. The frictions of the pressure regulator are required in order to reproduce pressure drop phenomenon as well as to replicate the injections system behavior during the steady state conditions. However, the second release cannot completely simulate the fueling system behavior: during the so-called cut-off phases the model is not able to reproduce the leakages between the high-pressure line and the low-pressure one. Therefore, the third release of the pressure reducing valve has been designed to proper simulate the injection system in all the possible conditions. The last release has been indeed able to correctly match the experimental data of the pressure rail during the driving cycle test. The dynamic response of the system, the pressure drops phenomena and the build-up of the rail pressure during the cut-off are correctly simulated with the injections system model embedding the calibrated third release of the pressure regulator.

A worth description of the modelling approach of the pressure regulator has been shown in this chapter. The correct estimation of the rail pressure free response can be achieved by importing correctly geometric parameters, the mass of the spool and the stiffness of the spring. The pressure drops phenomena can be reproduced only by adding the frictions lumped parameter elements. The rubbing frictions have to be introduced with the "O-ring"

element which simulates the dynamic friction and the stick-slip phenomenon. Finally, the piston shim lumped parameter element is responsible of the piston resilience during the opening and closure phases. These elements introduce a considerable number of parameters that have to be calibrated: an optimization technique is needed. The fraction factorial DOE has been selected for the optimization of the three releases. The experimental data of the pressure downstream the pressure regulator and in the rail have been adopted for the model calibration. The last release is able to fully reproduce the actual behavior of the valve. It's a predictive model that has been adopted for load and speed transient simulation analysis. The model highlights the mismatch between the injected fuel mass and the ECU evaluation. The estimated injected mass is always lower than the actual one, moreover during the rising speed or load transient. The simulation results highlight the need of a precise control strategy for the injection control. Therefore, the model can be used to realize, to verify and to adopt low throughput control strategies for the air-to-fuel mixture control.

3.8 References

[1]   Heywood, J. B. (1988). Internal combustion engine fundamentals (Vol. 930). New York: Mcgraw-hill.

[2]   Middleton, A., Neumann, B., & Khatri, D. S. (2008). Development of dedicated cng engine with multipoint gas injection system (No. 2008-28-0014). SAE Technical Paper.

[3]   A-Aziz, A.-R & Firmansyah, Firmansyah. (2009). The Effect of Fuel Rail Pressure on the Performance of a CNG-Direct Injection Engine (No. 2009-01-1498). SAE Technical Paper.

[4]   Hu, Q., Wu, S. F., Lai, M. C., Stottler, S., & Raghupathi, R. (1999). Prediction of pressure fluctuations inside an automotive fuel rail system (No. 1999-01-0561). SAE Technical Paper.

[5]   Lino, P., Maione, B., & Rizzo, A. (2007). Nonlinear modelling and control of a common rail injection system for diesel engines. Applied mathematical modelling, 31(9), 1770-1784.

[6]   Baratta, M., Misul, D., Spessa, E., Gazzilli, G., & Gerini, A. (2012, May). Fluid-dynamic characterization of a CNG injection system. In

ASME 2012 Internal Combustion Engine Division Spring Technical Conference (pp. 829-836). American Society of Mechanical Engineers.

[7]   Chiavola, O., & Giulianelli, P. (2001). Modelling and simulation of common rail systems (No. 2001-01-3183). SAE Technical Paper.

[8]   Mulemane, A., Han, J. S., Lu, P. H., Yoon, S. J., & Lai, M. C. (2004). Modeling dynamic behavior of diesel fuel injection systems (No. 2004-01-0536). SAE Technical Paper.

[9]   Seykens, X. L. J., Somers, L. M. T., & Baert, R. S. G. (2004). Modelling of common rail fuel injection system and influence of fluid properties on injection process. Proceedings of VAFSEP, 6-9.

[10]   Corno, M., Savaresi, S. M., Scattolini, R., Comignaghi, E., Sofia, M., Palma, A., & Sepe, E. (2009). Rapid virtual prototyping and dynamics analysis of a common rail injection system for gasoline engines. International Journal of Vehicle Systems Modelling and Testing, 4(1-2), 17-42.

[11]   Lino, P., Maione, B., & Amorese, C. (2008). Modelling and predictive control of a new injection system for compressed natural gas engines. Control Engineering Practice, 16(10), 1216-1230.

[12]   Misul, D. A., Baratta, M., & Kheshtinejad, H. (2014). Fluid-dynamic modeling and advanced control strategies for a gaseous-fuel injection system (No. 2014-01-1096). SAE Technical Paper.

[13]   http://nupet.daelt.ct.utfpr.edu.br/_ontomos/paginas/AMESim4.2.0/doc/pdf/pdfmain.html

[14]   Baratta, M., Kheshtinejad, H., Laurenzano, D., Misul, D., & Brunetti, S. (2015). Modelling aspects of a CNG injection system to predict its behavior under steady state conditions and throughout driving cycle simulations. Journal of Natural Gas Science and Engineering, 24, 52-63.

[15]   http://www.metatron.it/products-systems/pressure-regulators/product-range/meta-m-nd1.html

4 Transition from a production SPI CNG heavy-duty engine to a MPI one

* Part of the work described in this chapter has been previously published in:

1. Baratta, M., Kheshtinejad, H., Laurenzano, D., Maino, C., & Misul, D. A. (2018). Investigation into the Potentials of a Dedicated Multi-Point Injection System for a production NG Single-Point Heavy-Duty Engine. SAE International Journal of Engines, 11(2018-01-9275).

4.1 Introduction

In the previous chapter the effects of the pressure regulator behavior on the rail pressure dynamic have been analyzed. During this chapter the effects of two different injection system layouts on the goodness of the mixture formation will be discussed. It is worth recalling that the engine efficiency is strictly connected to the fueling system layout [1]. The CNG is injected by means of three possible layouts as explained in Section 2.3: single-point, multi-point or direct injection systems [2]. Typically, the heavy-duty engines are provided with SPI system. It is the simplest solution, with a simplified control of the amount of fuel injected mass and a reduced number of injectors [3]. The throttle body is connected with a fuel mixer, which is constituted of a reduced number of injectors. The single-point injection system is able to provide a global uniform air-fuel mixture: the charge is indeed formed after the throttle but typically before the intake manifold. Therefore, the SPI system leads to a mixture with the highest homogeneity among the cylinders. The intake system

dynamic affects the total mass trapped, but the air-to-fuel mixture for each cylinder is the same. Unfortunately, this feeding system introduces several issues. Overlap valve angles has to be reduced in order to avoid anomalous combustion in exhaust port and, as a consequence, exhaust gas temperatures increase [4]. Volumetric efficiency is affected by natural gas nature, therefore, SPI system has the lowest efficiency [5, 6]. These issues can be avoided by adopting a MPI system. This system introduces minor changes (one injector for each cylinder has to be adopted) but the anomalous combustion in the exhaust port (backfiring) can be easily overcome. As a matter of fact, the injection could be phased to increase the angle overlap (by delaying the injection window), and to maximize the volumetric efficiency. Moreover, the multi-point injection system can lead to a rapid control of the mixture formation during the transient conditions due to the reduced distance between the lambda control and the injectors [4, 7, 8]. Thus, the MPI system can be adopted in CNG heavy-duty engines, following the same evolution of the light-duty engines and it can lead to advance control strategies like the cylinder deactivation [9, 10]. The so called dynamic fire skipping can increase the specific fuel consumption under the partial load conditions, accepting additional costs for the realization of the adaptive valve actuation.

During the research activity showed in this chapter, the performance of a heavy-duty CNG engine designed with a SPI system has been compared with a dedicated MPI one. A wide experimental data set has been acquired with both injection systems in order to analyze the engine performance at different speeds and loads for the base single-point fueling system and the multi-point prototypal one. Furthermore, the effects of the different feeding system layouts on the cyclic variability and the cylinder-to-cylinder variation have been examined so as to evaluate the best solution. The prototypal MPI system has been fully analyzed by worth observing the engine performance output with different injection phasing. 0D-1D numerical simulations have been adopted giving the wide range of possible engine strategies to be verified. A numerical calibration can give some important advices for the optimal engine calibration [11, 12]. The numerical model simulates both the fluid-dynamic of the engine and the combustion process. For the latter a good compromise between accuracy and simplicity has been selected. The 0D-1D tool has been adopted and calibrated in order to evaluate the finest SPI system control that can be adopted and to evaluate the possible enhancement of the engine performance obtainable with the MPI system. The heavy-duty engine equipped with the

multi-point system has been indeed simulated with the adoption of the cylinder deactivation strategies for the partial load conditions.

4.2 Experimental set-up

The research activity has been carried out on a Yuchai YC6G turbocharged 7.8-liter heavy-duty engine fueled with CNG [13], and its characteristics are listed in Table 4.1. The abovementioned engine is based on a Diesel engine. Few modifications have been adopted in order to run the engine with CNG: new fueling system (with a new metering system) with a SPI layout, dedicated intake and exhaust system, optimized for the CNG and for the injection system layout, a different turbine (to resist to different exhaust temperature), a new piston and the substitution of the diesel injector with a spark plug. The SPI design and control were carried out by EControls Company.

Table 4.1: Engine characteristics

Engine specifications	Value
Type	Turbocharged, Vertical In-line, CNG engine
Bore (mm)	112
Stroke (mm)	132
Compression ratio	11
Cylinder number	6
Displacement (cm^3)	7800
Rated Power (kW/rpm)	191/2300
Rated speed (rpm)	1400
Injection system type	SPI/MPI

The engine layout mounted on the test bench is shown in Figure 4.1. The heavy-duty engine was indeed provided with both the injection systems. The SPI system has four injectors which fed the CNG provided by a fuel rail into a rubber pipe that is connected to a mixer after the throttle body. The mixer, a toroid with twenty-four holes in its inner surface, produces the charge mixture with the air flowing in the intake duct. The prototypal MPI system introduces instead one injector for each cylinder (six injectors that supply the natural gas in the runners near the intake valves) with CNG fed by a common rail. The experimental tests have been carried out with the heavy-duty engine running with the two different fuel injection systems. The engine is actually provided with the SPI system, although a MPI system solution with port-fuel injection layout is preferable.
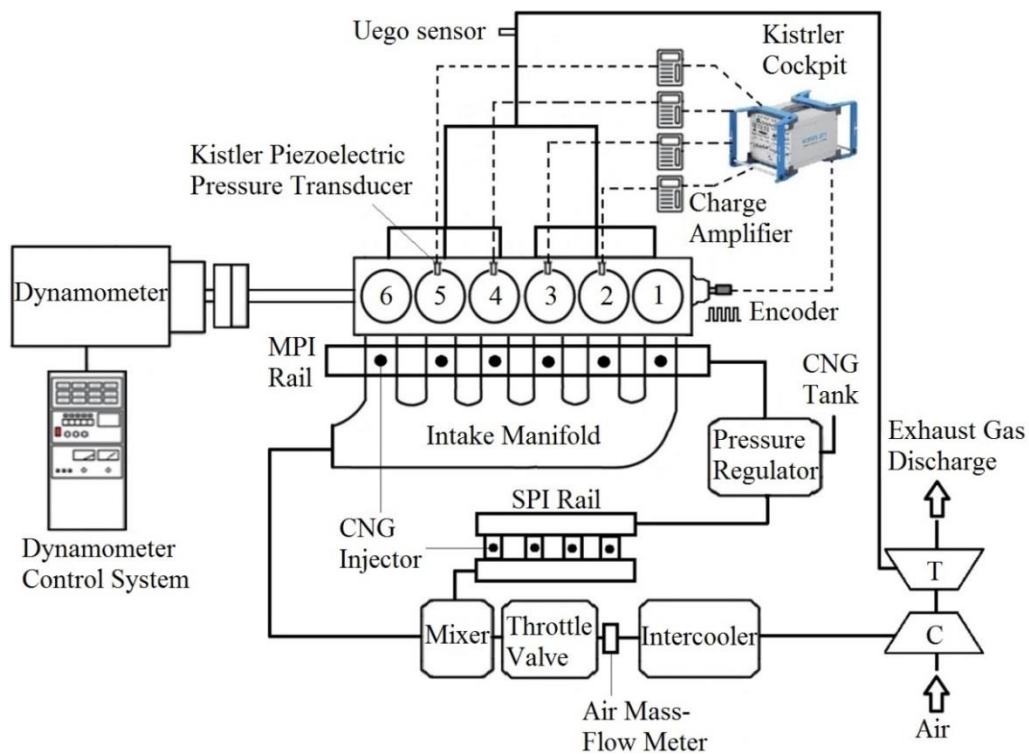
Figure 4.1: Engine set-up [14]

The CNG is stored in a tank at around 200 bar and the high-pressure line is connected to the low-pressure one by means of a Meta-M HFR Double Stage pressure regulator. The pressure valve reduces the pressure to 5 bar and feeds both the injection systems. The SPI system adopts four injectors (29B001-832 Yuchai YC6K13N), whereas six Keihin KN8-KEIH01 injectors have been selected for the MPI one. The ECU controls the sequential injections of the

injectors, governing the phasing and the injection duration. The injected fuel quantity is estimated by means of the closed-loop control guaranteed by the EGO lambda sensor and by the pressure and temperature estimation collected by sensors mounted on the rail. The control layout is the same for both the feeding system.

The acquisition system has been designed in order to acquire the cycle averaged engine speed and torque, the average pressure and temperature at the compressor inlet and outlet, at the inter-cooler outlet, in the intake manifold and intake runners and at the turbine admission. At the exhaust runners both the temperature and the air-to-fuel ratio have been acquired. The air-to-fuel ratios have been calculated by means of six universal exhaust-gas oxygen sensors (UEGO sensor). A further UEGO sensor has been installed at the turbine admission. The engine has been also equipped with an air mass flow meter. The in-cylinder pressure data cycles from cylinder "2" to cylinder "5" have been collected using four water-cooled KISTLER piezoelectric cylinder pressure sensor transducers with a crank angle resolution of 0.2° in order to correctly describe cyclic variation. The engine was tested with both the injection system layouts, under different operating conditions: thirty-two engine-conditions have been analyzed for different engine speeds and loads (Figure 4.2). In addition, transient operations have been analyzed with both the configurations. The tests have been carried out in order to verify the spread between the performances of the engine running with the SP and MP injection systems.
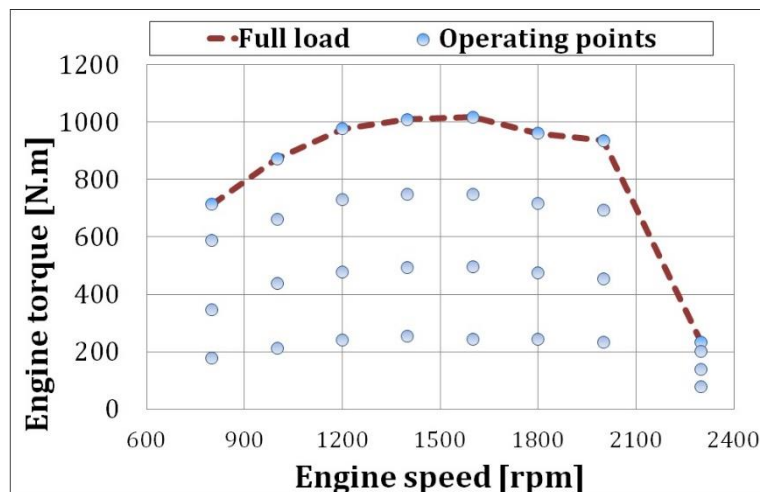
Figure 4.2: Engine operating conditions [14]

Furthermore, the potentiality of the engine running with the MPI system has been analyzed in deep by studying the effect of the injection phasing on the performance (Table 4.2) by changing the injection duration and the end of injection (EOI) position. Moreover, the aim of this research activity was the investigation of the air-to-fuel mixture formation quality attainable with the two injection system as well as the potentiality of the MPI system because of the enhanced control on the phasing.

Table 4.2: Injection duration and EOI phasing for different MPI operating conditions

Speed [rpm]	Injection duration [deg]		EOI advance with respect to BDC [°CA]			
	100% load	50% load				
800	112	65	0	30	60	120
1000	165	92	0	30	60	120
1200	217	117	0	30	60	120
1400	270	143	0	30	60	120
1600	326	170	0	30	60	120
1800	370	185	0	30	60	120
2000	408	206	0	30	60	120
2300	160	128	0	30	60	120

4.3 Experimental results

4.3.1 Steady-state conditions and transient tests

Engine steady-state campaign shown in Figure 4.2 has been run with both configurations as a first comparison. The engine torque, the in-cylinder average peak firing pressure (PFP), the BSFC and the turbine inlet temperature (synonym of the combustion efficiency) have been considered for the comparison. Figure 4.3 displays the experimental results for wide open throttle

condition (WOT) and for 50% load. The considered heavy-duty engine running in MPI configuration (blue squares) presents a sequentially phased injection with the end of injection set 60 deg before the compression bottom dead center (BDC). Instead, the SPI configuration features six injections (with four injectors) evenly spaced during one engine cycle. The spark advance (SA) was set to a single value for both systems. The brake specific fuel consumption is one of the most important characteristic for a heavy-duty engine. Figure 4.3c shows lower fuel consumption for the MPI system at the highest speed and for the 50% load in the entire range of engine speeds. As a matter of fact, the lower combustion efficiency of the SPI configuration reflects in higher turbine inlet temperatures, as shown in [15]: Figure 4.3d shows the turbine inlet temperature and it's worth observing that the two configurations operated with the same pressure at the intake manifold. The results highlighted in Figure 4.3c and Figure 4.3d are hence strictly correlated. Figure 4.3a and Figure 4.3b highlight the engine performance available by the two configurations.
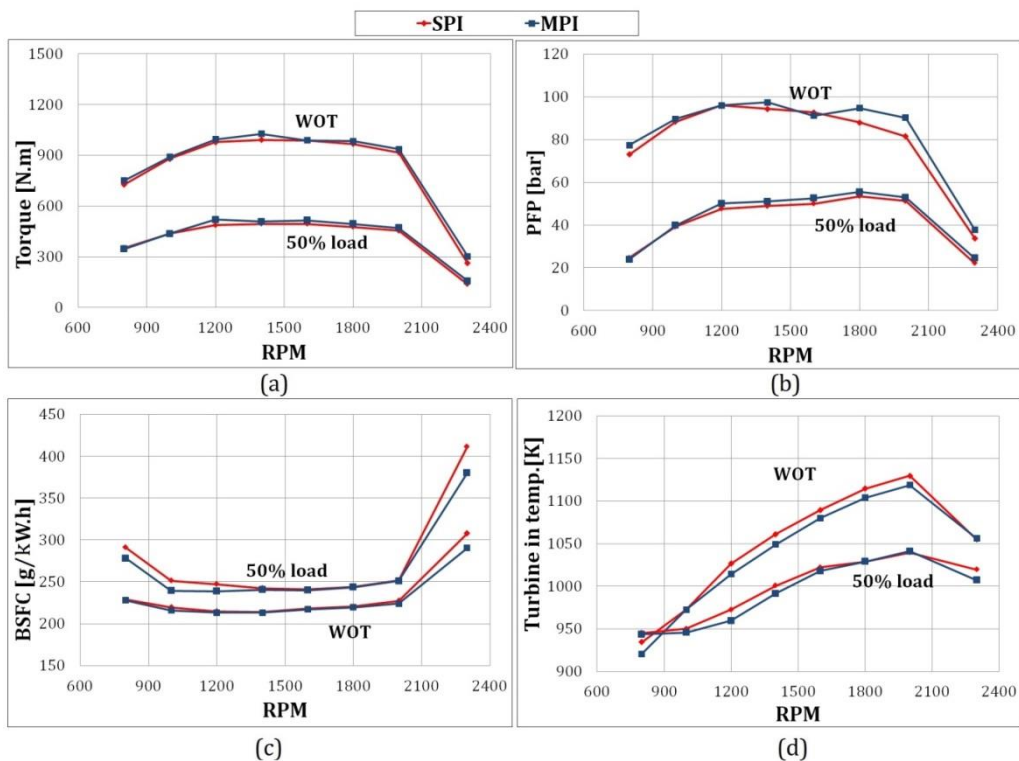
Figure 4.3: MPI vs. SPI for full load cases and 50% load ones [14]

The performance of the two layouts can be better evaluated by studying the effects on the mixture formation. The relative air-to-fuel ratios for the six

cylinders are displayed in Figure 4.4 for the MPI configuration (blue data) and SPI one (red data) under full load and 50% load conditions. The single-point injection system is not influenced by the intake system dynamic, because the air-to-fuel mixture formation is done after the throttle body and before the intake manifold. The formation is hence not affected by the pressure waves in the six runners. The relative air-to-fuel ratio is almost equal and homogeneous among the cylinders. The differences showed in Figure 4.4b will be insight in Section 4.5. The multi-point configuration is instead affected mainly by the intake runners' dynamics and slightly by the derating of the injectors and it is worth recalling that the port fuel injection affects intake runner's dynamic and the volumetric efficiency itself. Therefore, the MPI system leads to non-homogeneity of the charge among the cylinders. Considering negligible variation of the injected fuel between the different ports, cylinder 3 is typically the one with the larger air trapped for all the operating conditions, leading to a leaner mixture with respect to the other cylinders. On the opposite, cylinder 2 results in the lowest air mass trapped so it's the richest cylinder. The different air trapped reflects in different air-to-fuel mixture composition, leading to different combustion characteristics. Considering the gas nature of CNG the major effect is a different combustion laminar speed. Different combustion speeds affect the peak firing pressure pattern among the cylinders and the second one produces the highest one.

Under full load conditions a dynamic response change is appreciable. At the lower speeds the intake process is facilitate for cylinder 3, on the opposite the air mass tapped for cylinder 2 is the lowest, whereas the other cylinders present an almost equal intake process goodness (Figure 4.4a, c). At the higher speeds the dynamic response of the system is different. The first two cylinders are richer whereas the other four are leaner (Figure 4.4 e, g). Therefore, the induced air differences are affected by the dynamic response of the system at different engine speeds and loads. As a matter of, the change of the intake dynamic response at 50% load occurs after 1800 rpm (Figure 4.4b, d, f, h).

The dynamic response of the engine with both the injection system configurations to transient operations is almost the same, as displayed in Figure 4.5. For the sake of brevity, a load transient (Figure 4.5a) and a speed one has been represented and the two configuration presents almost the same behavior (the green dots represent the engine speed). The experiments have been carried out in order to verify the goodness of the ECU calibration. The engine running with both the injection system achieves the ECU target.
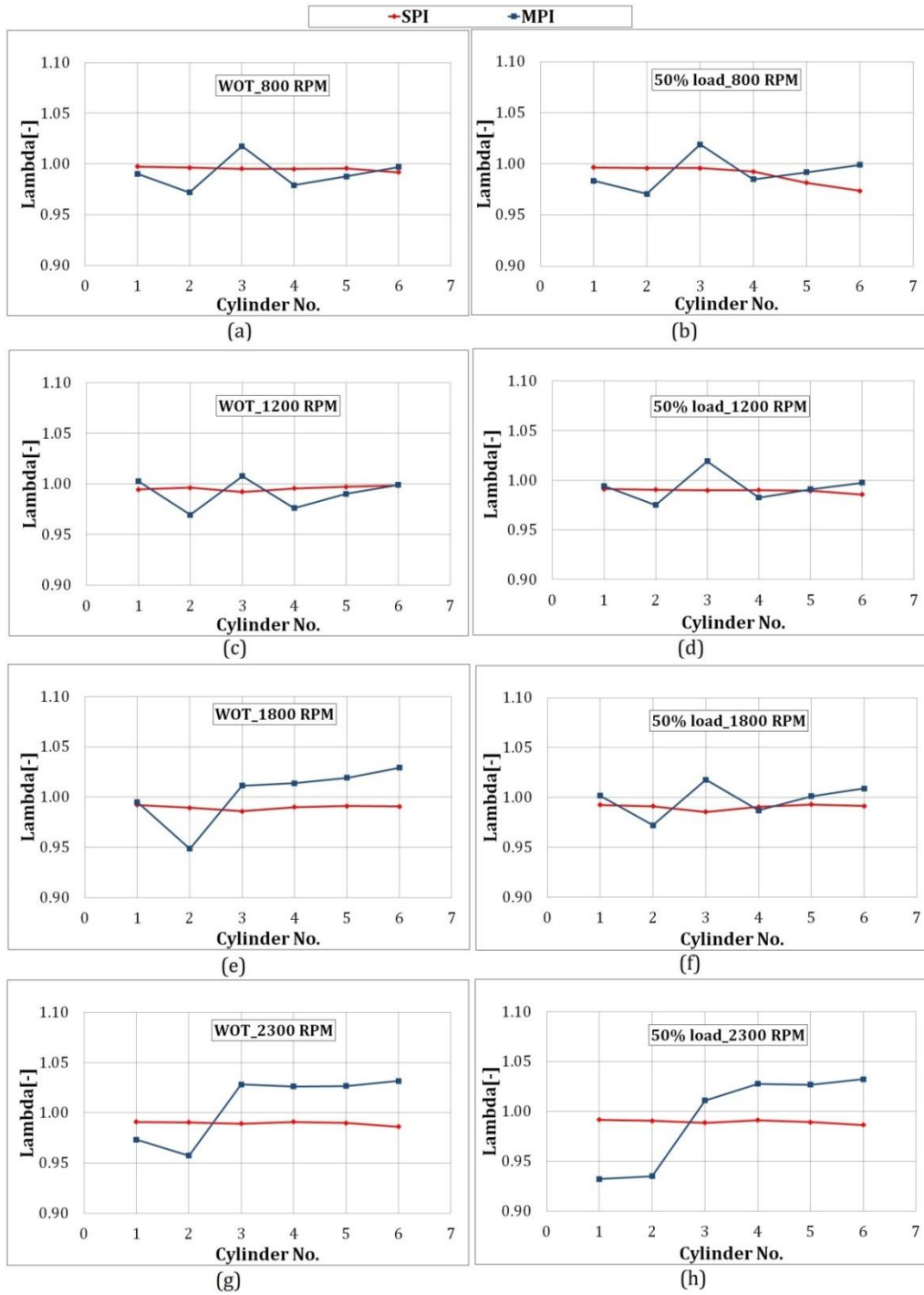
Figure 4.4: Relative air-to-fuel ratio variation for SPI and MPI configurations at different operating conditions [14]
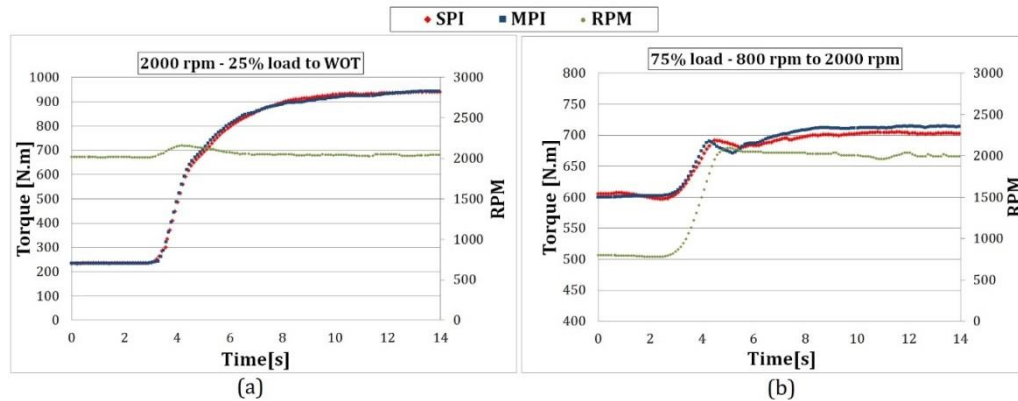
Figure 4.5: Load transient (a) and speed transient (b) [14]

4.3.2 Cyclic variation

A tough characterization of the cyclic variability of the two engine configurations has been performed in order to verify the behavior of the two systems. The four inner cylinders were equipped with pressure sensor transducers able to acquire the in-cylinder pressure with a crank angle resolution of 0.2°. One-hundred cycles have been acquired for each cylinder at each engine conditions in order to carry out a reliable statistical analysis. For the sake of conciseness, the coefficient of variation (COV: ratio between the standard variation and the average value of a physical quantity) of the indicated mean effective pressure (IMEP) and PFP will be shown. Figure 4.6 shows the cycle-to-cycle variability (CCV) of the engine running with SPI and MPI systems at 1200 rpm and 1800 rpm in full load condition, while Figure 4.7 raises the abovementioned analysis at 50% load. The bars represent the COV value of the analyzed quantity for each cylinder (red data for SPI results and blue data for MPI ones), whereas the horizontal dashed lines represent the average COV value.

The engine controls have been correctly calibrated and adjusted despite the two injection system arrangements, because the average IMEP COV is lower than 1.5%. However, the two injection systems produce observable differences in the engine performance output. As a matter of fact, the SPI system is responsible of a lower cylinder-to cylinder variability of both IMEP and PFP but with higher average values. The differences between the two systems have obviously to be ascribed to the two different mixture formation phenomena (the other engine parameters are kept almost the same). Therefore, the results

highlighted in the two figures listed below are connected with the ones shown in Figure 4.4.
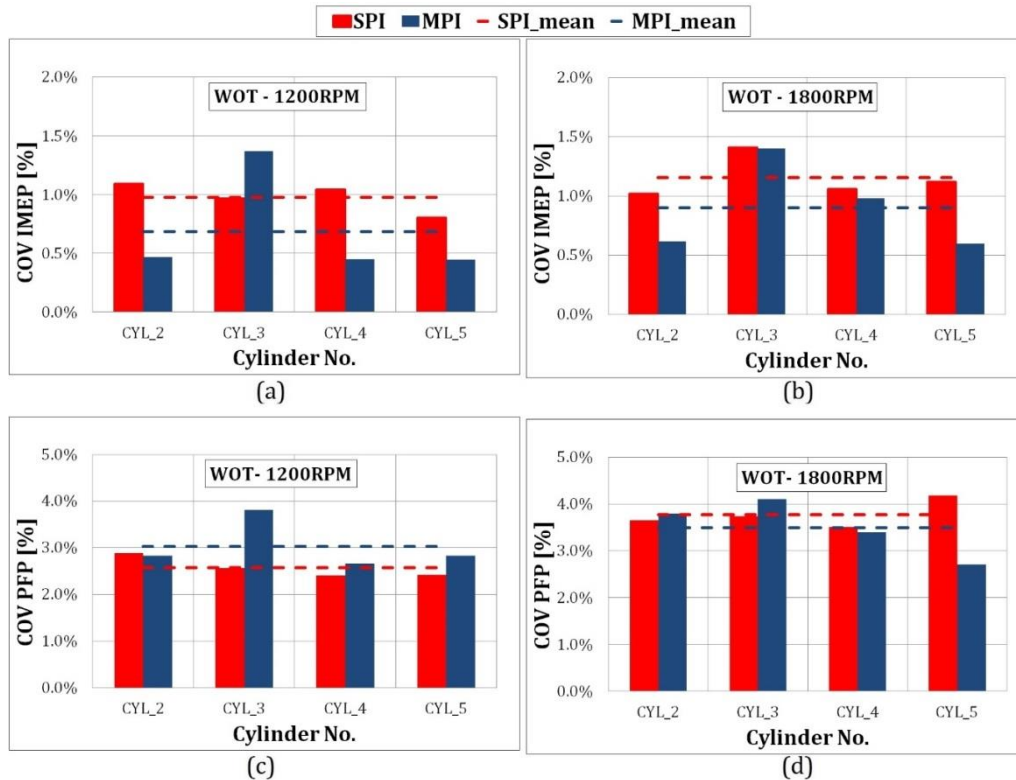
Figure 4.6: IMEP COV (a, b) and PFP COV (c, d) of the engine running with the two injection systems at 1200 rpm and 1800 rpm at full load condition [14]

Figure 4.6a and Figure 4.6c show the results of IMEP COV at 1200 rpm at full load condition: considering the MPI case, cylinder 3 has the highest dispersion, whereas the other three cylinders shows a sensible lower variability. The third cylinder was indeed the leaner one (Figure 4.4c), while the other three cylinders were also richer than themselves running under SPI mode. The CCVs of the two configurations at 1800 rpm in partial load condition (Figure 4.7b, d) are similar, in line with the results showed in Figure 4.4f. The improved efficiency of the MPI configuration has mainly to be ascribed to the different charge motion inside the chamber and to the different mixture formation. The injection has been approached to the combustion chamber by adopting the port fuel injection. The injection phasing has been overlapped to the intake one (further explanation will be given in Section 4.3.3), therefore the fluid motion has been enhanced and the in-cylinder turbulence has been improved also by the injection interaction with air flow.

Figure 4.7: IMEP COV (a, b) and PFP COV (c, d) of the engine running with the two injection systems at 1200 rpm and 1800 rpm at 50% load condition [14]

MPI system is able to guarantee better engine performances and lower cyclic variation, although the engine has been designed with dedicated intake and exhaust system to run properly with the SPI configuration. The engine indeed was not modified for the MPI layout. A proper engine layout and dedicated intake geometry (to connect the pressure waves and the injection events) can further improve the engine performance with the MPI configuration, as explained in [15].

4.3.3 Effects of the injection phasing

The effect of the injection phasing on the performance of the analyzed heavy-duty engine running with MPI system has been studied in deep by changing the injection duration and the end of injection (EOI) position (Table 4.2). The engine behavior under WOT and 50% load has been analyzed. Considering a steady state case, the injection duration window and the spark advance are kept unchanged whereas four different EOI positions have been tested. The four injection phases are linked to the intake phase: the first one (0 deg) end at the

BDC of compression, the last one ends 120 deg before, whereas the other two phases finish in the middle of the suction phase. For the base calibration the end of injection is positioned 60 deg before the BDC: it's the best solution as shown below. Figure 4.8 and Figure 4.9 show the CCV of the IMEP and PFP of the engine running at 1200 rpm and 1800 rpm in full load and 50% load conditions respectively. The four colored bars represent the behavior of the MPI engine depending on injection phasing. The worst results are produced by retarded injection phasing. The variability of the maximum pressure and of the IMEP is the highest for the phase that ends at the BDC. A retarded injection affects the engine performance because of [4, 16]: the mixture formation event needs a reasonable time to create a uniform and homogeneous charge and the injection event has to be phased with intake phase in order to exploit the dynamic effect of the air motion. These effects are emphasized at lower speeds and loads as shown in Figure 4.9a and Figure 4.9c because of a reduced air flow rate as well as lower turbulence intensity. For advance injection the results are unacceptable. As a matter of fact, there is a reasonable time for the mixture formation but reduced air motion due to a wrong phasing with the intake window.
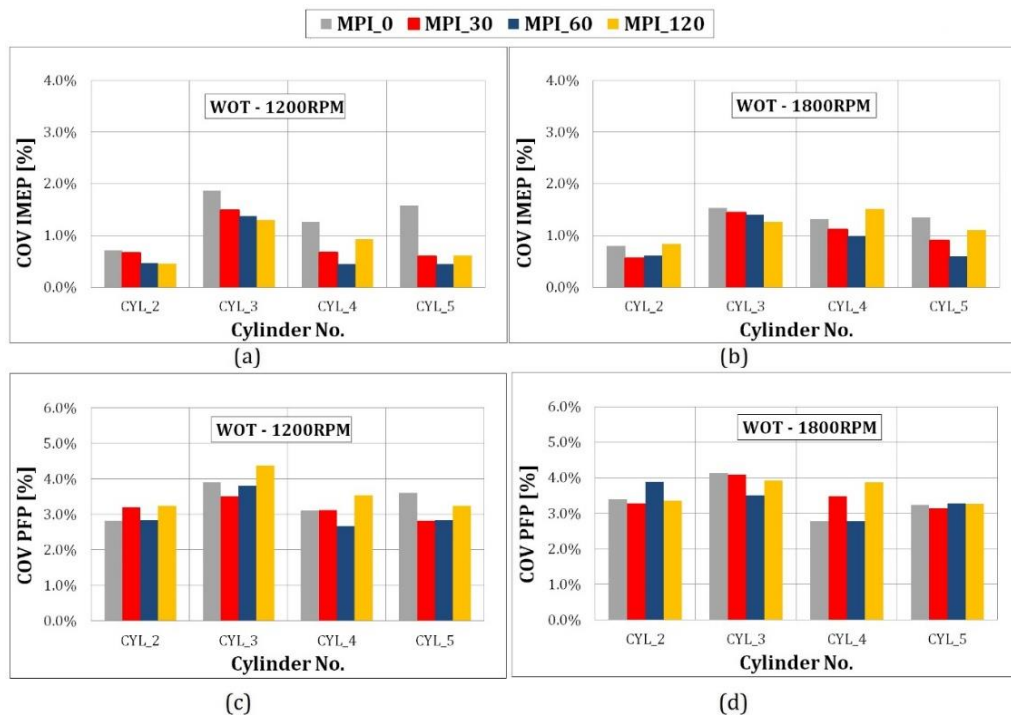
Figure 4.8: IMEP COV (a, b) and PFP COV (c, d) of the engine running with four different injection phasing at 1200 rpm and 1800 rpm at WOT [14]
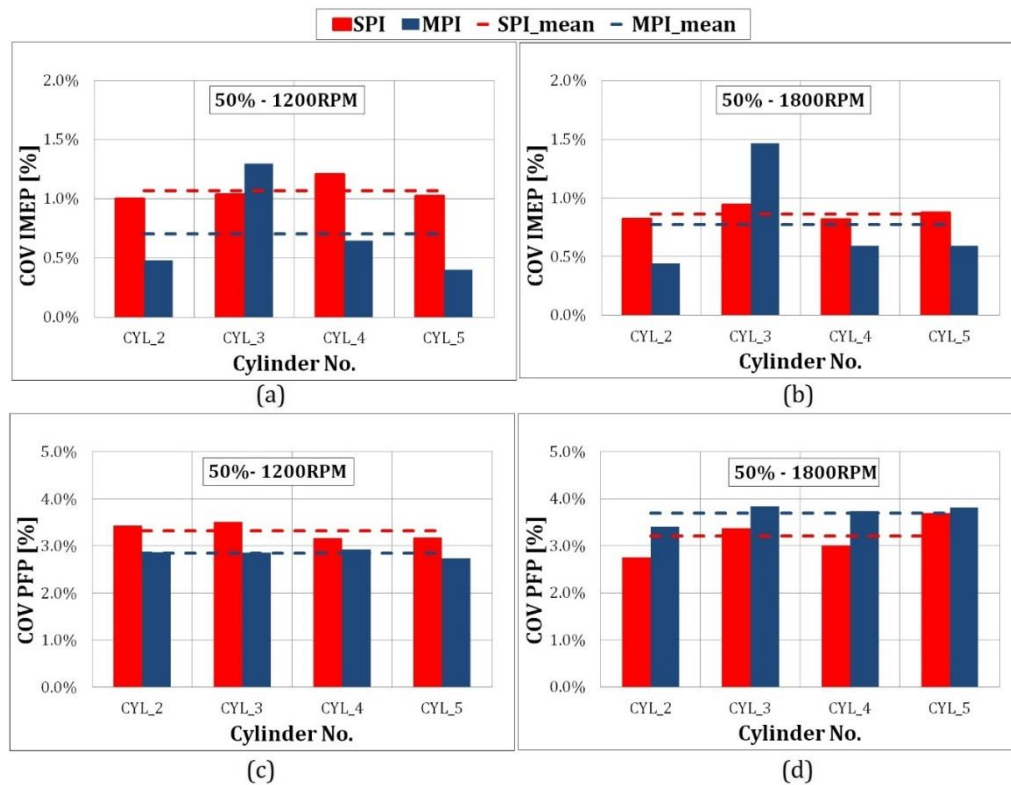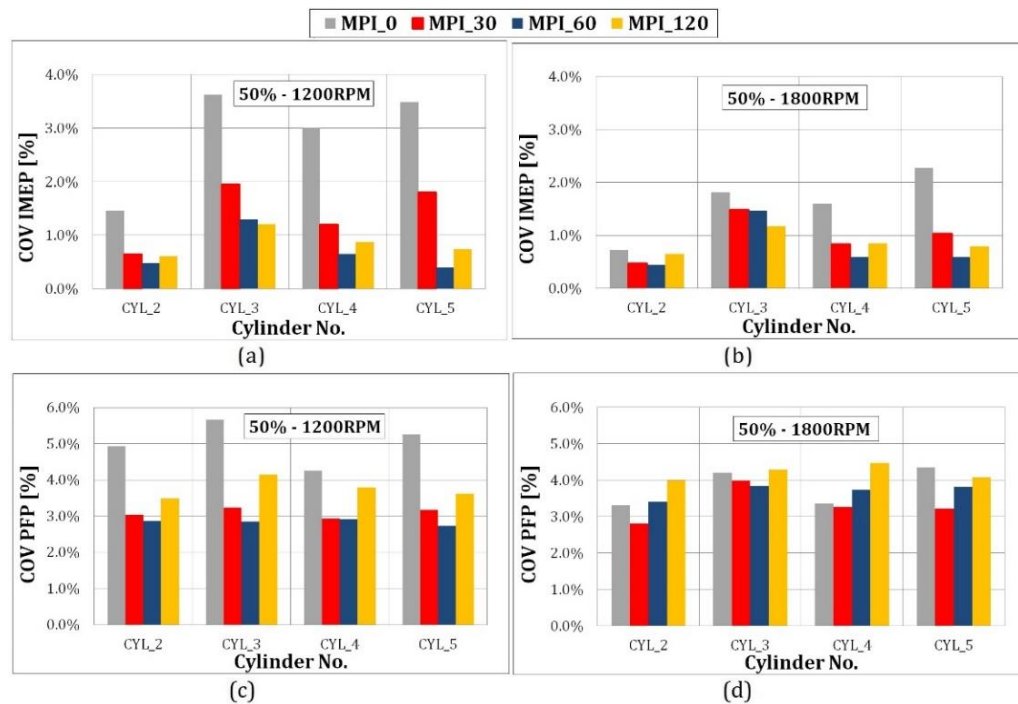
Figure 4.9: IMEP COV (a, b) and PFP COV (c, d) of the engine running with four different injection phasing at 1200 rpm and 1800 rpm at 50% load [14]

4.4 Engine numerical models

The experimental tests showed the engine performances with both the configurations in terms of engine power and combustion stability. Although the experimental findings have been useful for the evaluation of the benefits for a transition from a production SPI CNG heavy-duty engine to a MPI one, alternative engine controls could be evaluated with numerical codes. Therefore, the actual engine has been modeled in GT-Power v7.4 environment. The numerical code used is briefly described. Flow fluid dynamic is characterized by 1D Navier-Stokes equations, thus requiring a refined implementation of the geometric characteristics of all the elements of the internal combustion engine. The correct implementation of the material, of the fluid and of the valves' characteristics taken into consideration is mandatory. The pressure drop and heat transfer coefficients depend indeed primarily on the correct implementation of the technical characteristics of the experimental test bench. The combustion model used for the preliminary tests is a non-predictive combustion one. A non-predictive combustion model sets the burn rate as a function of crank angle [17]. It is appropriate when experimental data are provided and if the model is used to study variable that are minor affected by

the burn rate. Predictive combustion models are in turn slower, more complex and difficult to be calibrated. They are mandatory when the variable to be studied has a direct and significant effect on the burn rate. The ensemble in-cylinder pressure cycles collected for each cylinder at each steady state operating condition have been used for the implementation of the non-predictive Three-Pressure Analysis (TPA) tool. The TPA tool imposes the combustion rate to guarantee the experimental one (the heat coefficients have been properly tuned in order to guarantee the correct time history and look-up tables have been implemented). Each cylinder presents its own combustion rate. More details can be found in [17]. The maps of the turbine and compressor have been used for their characterization. The west gate diameters have been set by targeting the boost level and the turbine efficiency coefficients determined depending on the errors of the simulated pressure at the turbine inlet with respect to the experimental one. Finally, both the injection system configurations have been modeled and the two models have been calibrated considering the experimental data shown in Figure 4.3.

The SPI and MPI systems have been modeled considering the actual layouts. The single-point system is composed by four injectors that deliver the fuel in a steel pipe connected to a plastic robber bending pipe. The plastic pipe discharges the fuel in the intake duct through the mixer. The injection events have been reproduced by introducing the actual delivery rate of the CNG injector (for the given experimental rail pressure), and the injection durations have been corrected depending on the experimental relative air-to-fuel ratios. The based SPI injection strategy provides six injection events (produced by the four injectors) equally spaced in the engine cycle (120 deg). The 24 holes of the mixer have been substituted with an orifice. The diameter of the orifice has been calibrated in order to reproduce the experimental delivery rate and the proper dynamic response in the steel pipe. In the MPI model the single-point injection system has been neglected and six CNG injectors have been introduced in the GT-Power map in the proper positions. Finally, the injection phasing has been properly reproduced.

4.4.1 Validation of the numerical models

The GT-Power models have been set to simulate the engine map, consisting of the 32 operating conditions. The comparison between the experimental data (light blue dots) and simulation results (red squares) is displayed in Figure 4.10. Both the configurations have been analyzed in terms of air mass flow rate

(Figure 4.10a and c for SPI and MPI respectively) and IMEP (Figure 4.10b and d for SPI and MPI respectively). The results of the full load and 50% load conditions are highlighted. The numerical data approach the experimental results with negligible variances and the accuracy of the models is guaranteed by two major factors. The good agreement of the simulated air mass flow rate with the experimental one confirms the correct implementation of the engine layout (the models work with the same intake manifold and turbine inlet), whereas the goodness of the simulated IMEP certifies the appropriate application of the TPA tool. Moreover, the effectiveness of the numerical models is shown in Figure 4.11. For the sake of conciseness, the average in-cylinder pressure cycles of the 2nd cylinder running at WOT and 50% load at 1000 rpm and 2000 rpm are represented. A satisfying correlation is observed: the simulation data (dashed red lines) of the SPI and MPI models are in-line with the experimental readings (solid light blue lines). The negligible differences in the compression phases are correlated with the slight minor discrepancies of the induce air mass flow rates. The models have been hence correctly validated, thus leading to a detailed investigation into the effects of the injection phasing of the SPI system and specific advanced control of the MPI one (cylinder deactivation) on the engine performances.
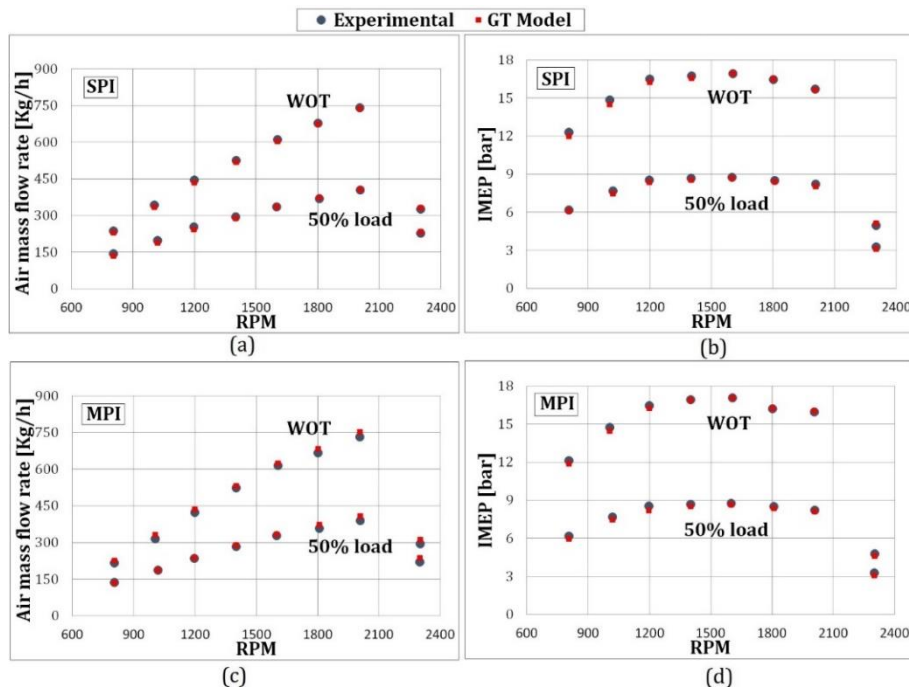
Figure 4.10: Comparison between experimental data and numerical results considering the air mass flow rate (a, c) and IMEP (b, d) [14]
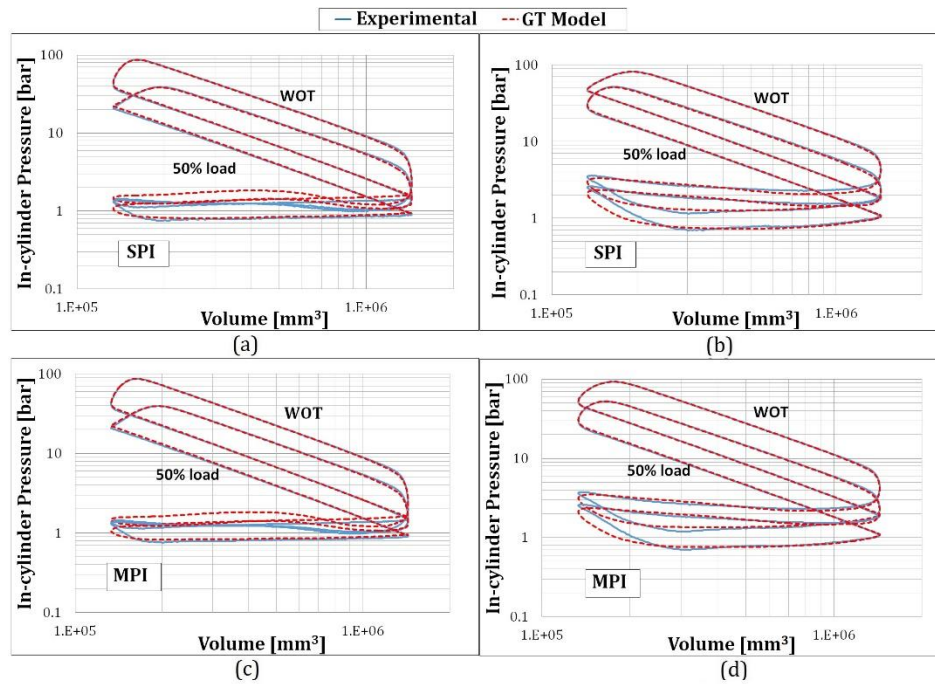
Figure 4.11: Experimental and simulated in-cylinder pressure cycle for 2nd cylinder at 1000 rpm (a, c) and 2000 rpm [14]

4.5 Effects of injection phasing for SPI configuration

The SPI system has been tested with the numerical model on different phasing strategies. A thorough analysis on the effect of the number of injection events and their spacing is useful to appreciate the differences between the two injection system configurations. The possible strategies are shown in Figure 4.12 (example of actuation at 800 rpm-WOT). The phased injections vary from "one" (Figure 4.12a) to six (Figure 4.12d) during the whole of an engine cycle (two revolutions of the crankshaft), and they are produced by four injectors controlled with precise order. The fuel mass flow rate is displayed with a dashed black line as a function of the crank angle. The valve lift of the six cylinders are displayed considering the firing order of the engine. For the first case (Figure 4.12a), the injectors are actuated all together instantaneously, whereas in the second one (Figure 4.12b) two injectors at a time are actuated, leading to two global injections. The third case (Figure 4.12c) shows four evenly spaced injections produced by the four injectors. Finally, the last case (Figure 4.12d) shows six injections produced by the four injectors with a sequentially order. The behavior of the engine is affected by the single-point injection system strategy. Therefore, the main engine performances (at WOT)

are reported in Figure 4.13, in which the intake manifold pressure, the PFP, the brake torque and the turbine inlet pressure are listed. These parameters are affected by the relative air-to-fuel ratio distribution between the cylinders, which are shown in Figure 4.14 and 4.15. For the sake of brevity, one steady state point has been represented in Figure 4.12 for the analysis of the four strategies. The considered operating condition is the one with the larger engine cycle (engine speed is equal to 800 rpm, leading to an engine cycle of 150 ms) and the shortest ET between the full load cases. The selected operating condition is hence the most useful one in order to analyze the injection sequences. With a reduced number of injection events during the engine cycle, a discontinuous feeding to the mixer body is guaranteed. The non-homogeneity of the mixture formation quality is enhanced at the lower speeds, where the injection events are spread due to lower injection duration with respect to the engine cycle. For higher engine speeds, the injection duration is gradually extended through the engine cycle, corresponding to better mixture formation homogeneity. Strategies with augmented injection events allow to find a good compromise between ET duration and rail pressure as highlighted in [18]. As a matter of fact, a reduced number of injections could lead to angular injection duration higher than engine cycle.
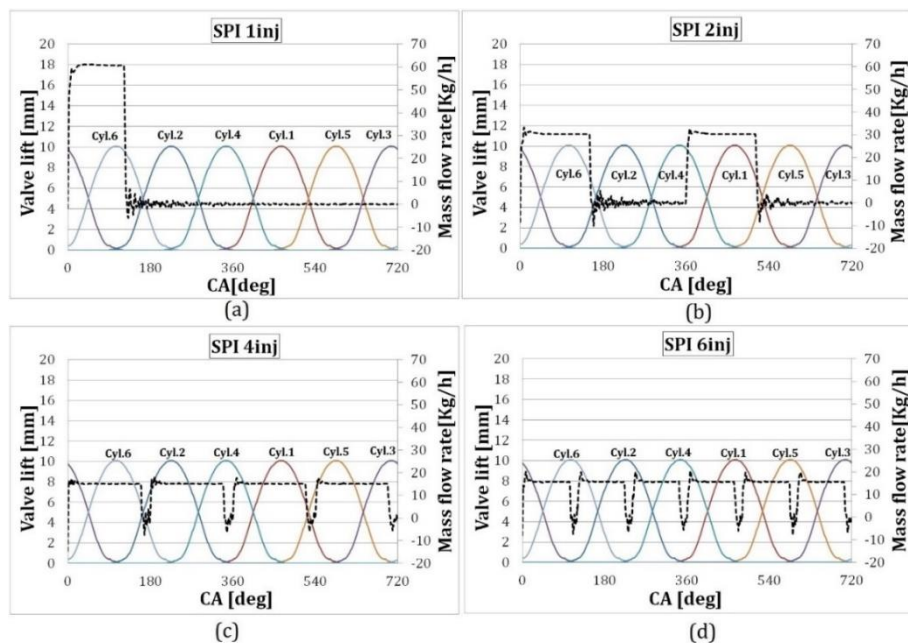
Figure 4.12: One to six injections for SPI engine at 800 rpm and full load condition [14]

Strategies with four or six injections allow for overlapping injection events produced by different injectors. Moreover, discontinuous feeding to the mixer at lower speeds are avoided by overlapped injections. On the contrary, at higher speeds the ET could exceed the engine cycle duration. The solution with an augmented number of injections is however the one with better results at lower speeds giving the rail pressure value constraint.

The engine performance outputs showed in Figure 4.13, 4.14 and 4.15 highlight the effect of the different SPI system control strategies. The main engine outputs are nearly the same for four and six injection events. The fuel delivered by the mixer is indeed released nearly continuously, allowing a correct mixing and hence a homogeneous air-to-fuel ratio among the cylinders. Figure 4.14 shows the noteworthy low cylinder-to-cylinder relative air-to-fuel ratio variation among the cylinders of the abovementioned strategies.
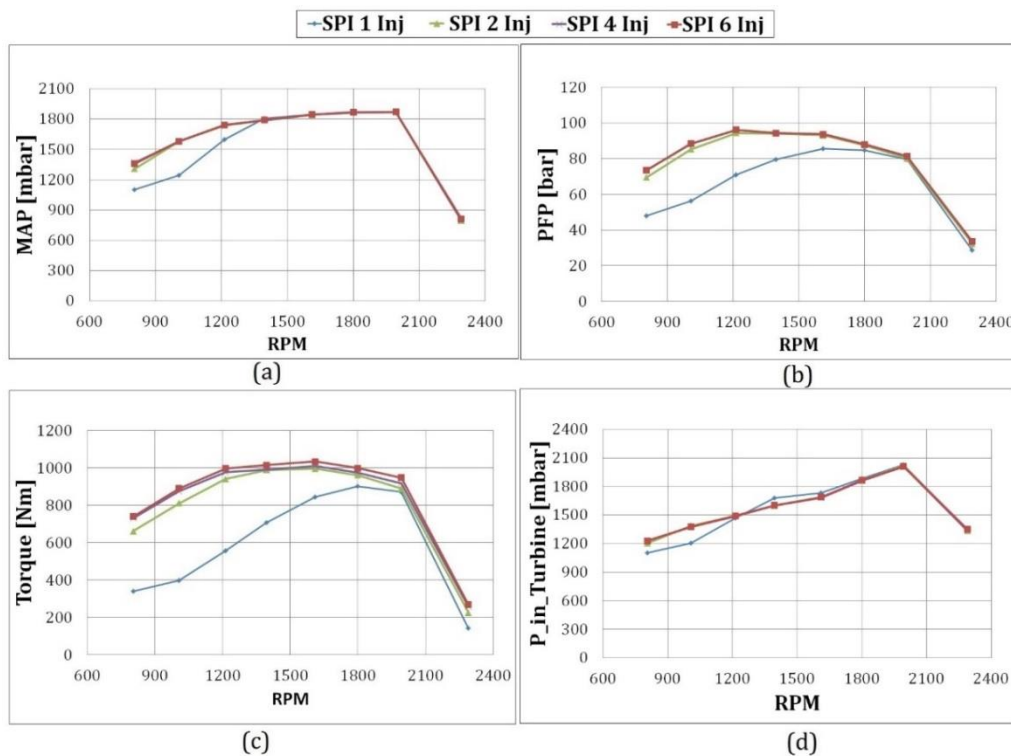
Figure 4.13: Engine performance at full load condition for different injection strategies [14]

The concentrated number of injections leads instead to appreciable lower engine performances at low and medium speeds. As a matter of fact, the discontinuous feeding of the fuel through the mixer brings to relevant non-

homogeneity of the air-to-fuel ratio among the cylinders. Considering the one injection control strategy, the lambda distribution in the worst operating condition (at 800 rpm and WOT) is shown in Figure 4.15: a significant cylinder-to-cylinder lambda dispersion is appreciable, with extremely lean and rich cylinders. As a matter of fact, the strong non-homogeneity leads to low combustion efficiency (Figure 4.13b and c), and extreme lean combustion could produce misfire events. The reduced engine out temperatures reflects into lower available enthalpy at the turbine inlet, resulting into the impossibility to reach the boost level (Figure 4.13a). The based control strategy of the SPI system contemplates the six injection events, thus no-possible enhancement could be achieved. A different control strategy will be shown in the next section, which can be adopted exclusively with the MPI system.
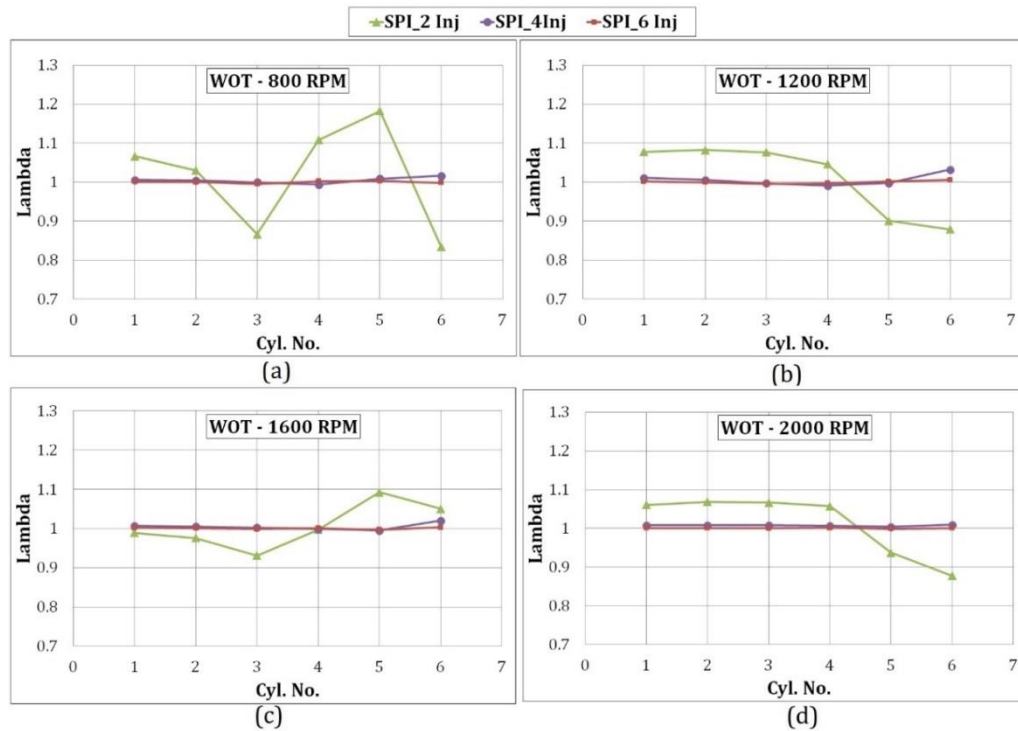
Figure 4.14: Relative air-to-fuel ratio distribution among the cylinders for the last three strategies at WOT for the indicated strategies [14]
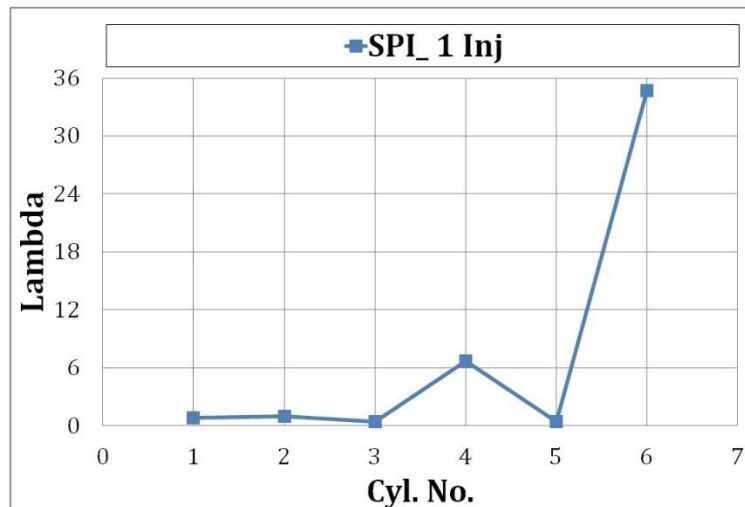
Figure 4.15: Relative air-to-fuel ratio distribution among the cylinders for the one
injection strategy at 800 rpm and WOT [14]

4.6 MPI cylinder deactivation strategy simulation

The based SPI system with the best control strategy (six injections with the
four injectors) showed worst engine performance than prototypal MPI
configuration. The MPI configuration of the heavy-duty engine produces the
same power output but with a lower fuel consumption (Figure 4.3a and c),
though intake and exhaust systems were not designed for the multi-point
system. Furthermore, MPI system could lead to better performances with the
so-called cylinder deactivation strategy, which cannot be adopted whit a SPI
system. Cylinder deactivation (or fire skipping) strategy reduces the fuel
consumption at partial load operating conditions by excluding some cylinders
depending on the torque request. Deactivation is adopted by neglecting the
injection and ignition of the excluded cylinder and typically by adopting a
variable valve actuation system (VVA) to close the intake and exhaust valves
to create an "air spring" in the chamber and neglecting the pumping losses. In
this section the GT-Power model of the MPI system has been improved in
order to introduce the cylinder deactivation control strategy during partial load
cases. For a given operating point, some cylinders are deactivated to guarantee
the requested power and reduce the fuel consumption. Table 4.3 shows the
results of the fire skipping strategy at 25% and 50% load by listing the number
of active cylinders and the improvement of BSFC.

The TPA combustion model has been substituted with Wiebe combustion tool. Mass fraction burned is characterized by the following function:

$$x_b = 1 - e^{-a\left(\frac{\theta - \theta_0}{\Delta\theta}\right)^{m+1}} \tag{4.1}$$

The parameters of the Wiebe function have been experimentally collected (θ angles) and evaluated with the TPA model (a and m parameters). Look-up tables for Wiebe parameters have been adopted for cylinder deactivation simulations, depending on engine speed and air trapped mass (simplified way to evaluate the different in-cylinder turbulence intensity). As a matter of fact, the engine model has been run by adopting the same boost level. The number of active cylinders has indeed been selected in order to guarantee the requested torque and the desired intake manifold pressure.

Table 4.3: Cylinder deactivation results [14]

Speed [rpm]	50% load		25% load	
	N. of active cylinders	BSFC benefit [%]	N. of active cylinders	BSFC benefit [%]
800	5	5.1	-	-
1000	5	1.6	3	12.1
1200	5	1.3	3	9.3
1400	4	2.8	3	7.0
1600	4	2.6	3	6.1
1800	4	3.0	3	6.4
2000	4	3.3	3	7.6

Different methods have been adopted to achieve the desired engine performances. For instance, the waste gate position has been kept unchanged, minor changes to the throttle position has been adopted to guarantee the correct manifold pressure and the SA has been adjusted in accordance with the look-up tables. Otherwise, the waste gate position has been changed by locking the throttle angle. The two methods produce almost the same results in term of BSFC, assessing the reliability of the cylinder deactivation method for the fuel consumption reduction and the non-correlation of the technique with throttling as well as exhaust backpressure.

Cylinder deactivation strategy leads to appreciable fuel consumption reduction for reduced loads, as shown in Figure 4.16. As a matter of fact, fire skipping strategy produces better results for a reduced power demand, thus increasing the number of deactivated cylinders as reported in [10]. Active cylinders reach hence better volumetric efficiency (due to the reduced number of cylinders at the same engine speeds) and combustion efficiency. The higher combustion efficiency is reached by increasing the intake manifold pressure to guarantee the requested power, with a corresponding reduction of the pumping losses. Looking to the deactivated cylinders, lower global pumping losses are produced by air spring effect.
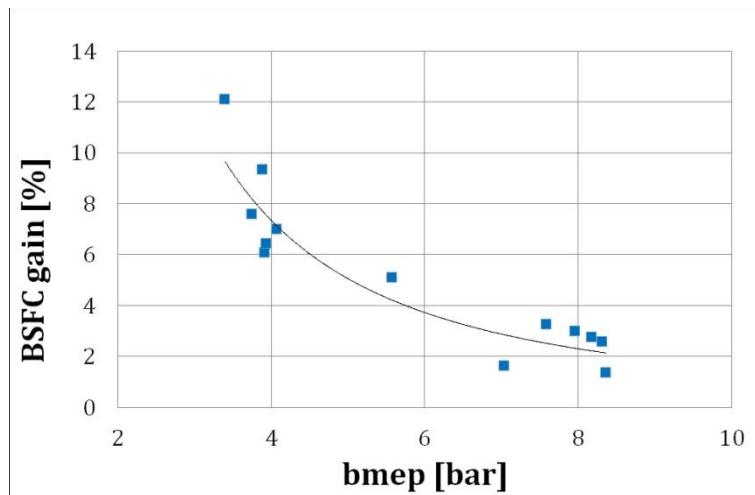
Figure 4.16: Brake specific fuel consumption gain with cylinder deactivation strategy as a function of the load [14]

The operating conditions listed in Table 4.3 have been analyzed in depth with the model running with the based throttle positions. The increased volumetric efficiency for the 2nd cylinder (activated one) is shown in Figure 4.17a. The

reduced number of activated cylinders produces a buildup of the air mass trapped, considerably higher at 25% load case in which the number of deactivated cylinders is half of the totality. For 50% load the trend of volumetric efficiency presents a deviation from 1200 rpm and 1400 rpm, because of the change of activated cylinders (see Table 4.3). The cylinder deactivation technique leads to an increase of the engine efficiency (Figure 4.17b) and a reduction of BSFC (Figure 4.17c) for the abovementioned reason. The improvement of the engine performances has to be ascribed only to the fire skipping technique: adopting a WOT and change the waste gate position at partial load conditions is possible only above 60% load (impossible hence for 50% and 25% load) and the engine efficiency improvement is negligible. Moreover, the number of deactivated cylinders is not linearly correlated with the requested load, as listed in Table 4.3: the number of active cylinders doesn't correspond to the load percentage, i.e. at 50% load the firing cylinders are higher than 3. This is because of different turbocharger behavior due to lower temperature at turbine inlet (as shown in Figure 4.17d) caused by higher combustion efficiency.
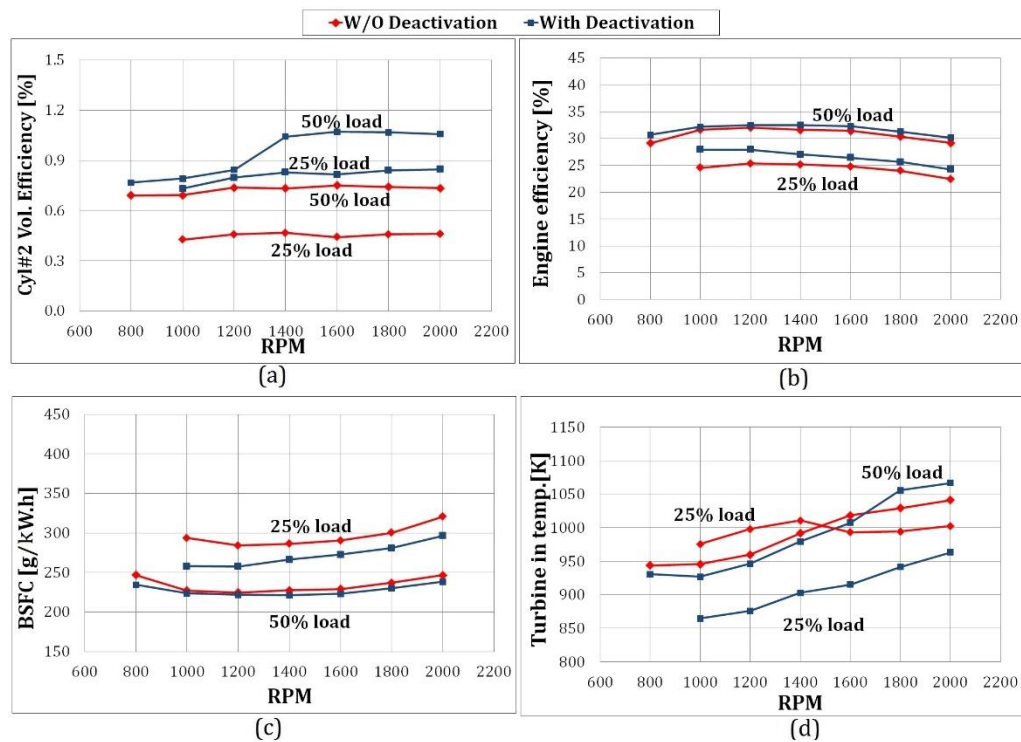
Figure 4.17: Engine performances at partial load conditions with cylinder deactivation mode [14]

The corresponding in-cylinder pressure traces of the firing cylinder (2nd cylinder) during fire skipping mode are compared with the base in-cylinder pressure cycle during normal partial load operations (Figure 4.18). The fire skipping cycles (dashed lines) are better than corresponding base ones (solid lines), but cannot reach the corresponding full load pressure cycle due to worse behavior of the turbocharger. Anyhow, the present research doesn't take into account the effects of the dynamic fire skipping (differences between constantly deactivated cylinders and active-deactivate strategies).
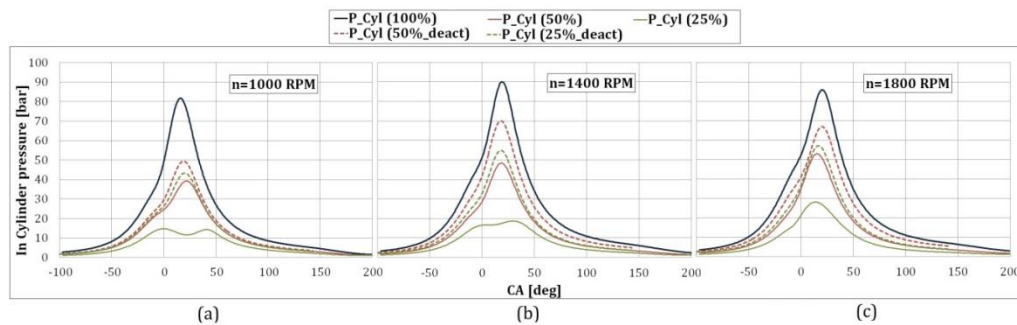
Figure 4.18: Comparison between in-cylinder pressure cycles during base partial load and fire skipping ones [14]

4.7 Conclusion

The research highlighted the behavior of a based SI heavy-duty engine fueled with CNG provided with two injection system layouts: a single-point configuration and a multi-point one. The SPI system was the base layout whereas the MPI configuration was a prototypal version. The two configurations have been analyzed under 32 steady state points (a full map of the engine operating conditions) and transient operations. The two layouts have been compared in terms of engine performance and cyclic variation. The MPI version showed light BSFC reduction at partial load conditions and appreciable lower cycle-to-cycle variability. The prototypal multi-point system is indeed able to better exploit the dynamic of the intake air mass flow rate. As a matter of fact, the injection event has been optimized considering the intake phase. Although MPI system produced a higher cylinder-to-cylinder variation (due to different air trapped among the cylinders), the global IMEP COV of the engine reduced by 30% at lower speeds. The SPI engine has indeed a better air-to-fuel mixture homogeneity, but lower combustion efficiency.

The GT-Power numerical models of the two configurations have been used in order to consider new control solutions. The SPI system was tested by changing the number phasing of the injection events for a fixed system layout (four injectors). Concentrated injection events lead to non-homogeneity of the mixture formation due to discontinuous feeding of the fuel through the mixer. Therefore, with a higher number of injections a better trade-off between rail pressure and mixture equality can be found. Anyhow, SPI system with the best control strategy showed worst engine performance than prototypal MPI configuration. Furthermore, MPI system model has been adopted to simulate cylinder deactivation strategy, which cannot be run whit a SPI system. The fire skipping mode has been simulated and the numerical model shows reduction of the brake specific fuel consumption up to 12% at lower speeds and loads. ECU control strategies could improve engine functioning considering new solutions for heavy-duty engines like dynamic fire skipping mode and advanced valve managements like VVA.

4.8 References

[1]   Baratta, M., Kheshtinejad, H., Laurenzano, D., Misul, D., & Brunetti, S. (2015). Modelling aspects of a CNG injection system to predict its behavior under steady state conditions and throughout driving cycle simulations. Journal of Natural Gas Science and Engineering, 24, 52-63.

[2]   Heywood, J. B. (1988). Internal combustion engine fundamentals (Vol. 930). New York: Mcgraw-hill.

[3]   Park, C., Lee, S., Lim, G., Choi, Y., & Kim, C. (2013). Effect of mixer type on cylinder-to-cylinder variation and performance in hydrogen-natural gas blend fuel engine. International Journal of Hydrogen Energy, 38(11), 4809-4815.

[4]   Ji, S., Lan, X., Cheng, Y., Zhao, X., Li, X., & Wang, F. (2016). Cyclic variation of large-bore multi point injection engine fuelled by natural gas with different types of injection systems. Applied Thermal Engineering, 102, 1241-1249.

[5]   Thipse, S. S., Sonawane, S. B., FD'Souza, A., Rairikar, S. D., Kavathekar, K. K., & Marathe, N. V. (2015). Injection Strategies,

Optimization and Simulation Techniques on DI CNG Technology
(No. 2015-26-0046). SAE Technical Paper.

[6]   Choi, M., Lee, S., & Park, S. (2015). Numerical and experimental
        study of gaseous fuel injection for CNG direct injection. Fuel, 140,
        693-700.

[7]   Dickinson, P., & Shenton, A. T. (2009). Dynamic calibration of
        fueling in the PFI SI engine. Control Engineering Practice, 17(1), 26-
        38.

[8]   Geok, H. H., Mohamad, T. I., Abdullah, S., Ali, Y., & Shamsudeen,
        A. (2009). Experimental investigation of performance and emissions
        of a sequential port injection compressed natural gas converted
        engine (No. 2009-32-0026). SAE Technical Paper.

[9]   Patel Nimit, M., & Patel, A. D. (2016). Conversion of diesel engine
        to port injection cng engine using gaseous injector nozzle multi holes
        geometries improvement: A review. International Journal of
        Automotive Engineering, 6(3), 2220-2235.

[10]   Wilcutts, M., Switkes, J., Shost, M., & Tripathi, A. (2013). Design
        and benefits of dynamic skip fire strategies for cylinder deactivated
        engines. SAE International Journal of Engines, 6(2013-01-0359),
        278-288.

[11]   Guzzella, L., & Onder, C. (2009). Introduction to modeling and
        control of internal combustion engine systems. Springer S cience &
        Business Media.

[12]   Zeng, K., Lv, S., Liu, B., Ma, F., & Huang, Z. (2006, December).
        Development and calibration on an electronic control system of cng
        engine. In Vehicular Electronics and Safety, 2006. ICVES 2006.
        IEEE International Conference on (pp. 204-208). IEEE.

[13]   http://www.yuchaiie.com/product/10988.html

[14]   Baratta, M., Kheshtinejad, H., Laurenzano, D., Maino, C., & Misul,
        D. A. (2018). Investigation into the Potentials of a Dedicated Multi-
        Point Injection System for a production NG Single-Point Heavy-

Duty Engine. SAE International Journal of Engines, 11(2018-01-9275).

[15] Czerwinski, J., Comte, P., & Zimmerli, Y. (2003). Investigations of the gas injection system on a HD-CNG-Engine (No. 2003-01-0625). SAE Technical Paper.

[16] Baratta, M., & Rapetto, N. (2015). Mixture formation analysis in a direct-injection NG SI engine under different injection timings. Fuel, 159, 675-688.

[17] GT-SUITE Engine Performance Application Manual, Gamma Technologies, 2016.

[18] Baratta, M., Misul, D., Spessa, E., Gazzilli, G., & Gerini, A. (2012, May). Fluid-dynamic characterization of a CNG injection system. In ASME 2012 Internal Combustion Engine Division Spring Technical Conference (pp. 829-836). American Society of Mechanical Engineers.

5 Combustion, CCV and knock in CNG SI engine

5.1 Introduction

Nowadays, research activities on CNG engine are focused on developing ICE elements correlated with combustion in order to reduce power output losses. In order to exploit knock-resistance peculiarity of NG, new strategies have to be adopted like new combustion chamber shape, new turbo compressor (TC) strategies and improved ignition management [1]. Moreover, full campaign of experimental tests on ICE is costly and time demanding, considering the amount of degree of freedom [2]. Dedicated engine operations and control strategies can be preventively analyzed by modelling the entire engine system. During the previous research activity, the MPI heavy-duty engine has been modeled with GT-Power in order to test cylinder deactivation. The combustion models used for the tests were non-predictive combustion tools. As a matter of fact, the Three-Pressure Analysis model and the Wiebe function have been implemented [3]. The former was adopted for engine model validation, whereas the latter was used for implementation of fire skipping strategy. The Wiebe function was adapted by adopting look-up tables depending on engine speed and volumetric efficiency. It is worth recalling that a non-predictive combustion model sets the burn rate as a function of crank angle [3]. It is appropriate when experimental data are provided and if the model is used to study variable that are minor affected by the burn rate. Predictive combustion models are in turn slower, more complex and difficult to be calibrated. However, they are mandatory when the variable to be studied has a direct and significant effect on the burn rate. The new strategies previously mentioned strictly affect the heat release rate (HRR) shape. Therefore, predictive

combustion model should be adopted. High-efficiency natural gas engines could in turn lead to knock conditions. Higher CR and different combustion chamber shape could be responsible of the abovementioned anomalous combustion beyond NG knock-resistance. Experimental analysis at test bench could be carried out in order to calibrate appropriate ECU control strategies for knock mitigation. However, an experimental campaign under knock condition is dangerous and costly due to possible failure of mechanical parts of the engine. Numerical models for auto-ignition prediction could hence overcome the aforementioned problems by reducing the experimental tests. A sound knock prediction model is anyhow based on a correct estimation and simulation of the average in-cylinder pressure cycle at different operating conditions (predictive combustion model for the heat release rate modelling) and of the cycle-to-cycle variability. Moreover, knock and CCV are strictly correlated, thus requiring a numerical model for reliable cyclic variability simulation. In this chapter combustion, CCV and knock in SI engine will be evaluated and a new methodology will be presented.

5.1.1 Combustion and CCV in SI engine

A brief introduction of combustion physics of SI engine is described (most of the information are available in [1]). In commonly SI engine, an almost homogenous air-to-fuel mixture is induced or formed in the combustion chamber (and mixed with residual gas) and then compressed. The combustion is started by a spark plug approaching typically the top dead center (TDC). After the kernel growth phase, the flame grows burning the fresh mixture. The turbulent flame advances until it comes to the chamber walls and quenches. In the rapid burning phase, the flame front is corrugated by the in-cylinder turbulence and propagates depending on the in-cylinder gas mixture composition and motion. The SA is typically located before the TDC. As a matter of fact, the combustion duration process ends in 30 to 90 deg, thus it generally starts during the compression phase and ends in the expansion stroke. By advancing the SA, the combustion is phased with the compression stroke and the in-cylinder pressure rises, but the compression stroke work increases. By retarding the spark discharge, the combustion is phased with the expansion stroke and the in-cylinder pressure diminishes. The best SA position depends on the operating conditions and leads to the MBT. The mass fraction burned shape is affected by the combustion phases. The first part, the so-called flame-development phase, starts at the SA and ends commonly when a significant part of the mixture has burned (typically 10 percent of the total charge). The

period of the kernel growth phase is affected by charge composition and motion in the spark plug region. The central part of the combustion process is called rapid burning phase. During the previous-mentioned period the large fraction of the charge is burned and its behavior is correlated to the in-cylinder chamber conditions. The last phase is affected by the flame quenching due to interaction between heat released by combustion process and heat transferred between charge and chamber walls. The three stages are shown in Figure 5.1.
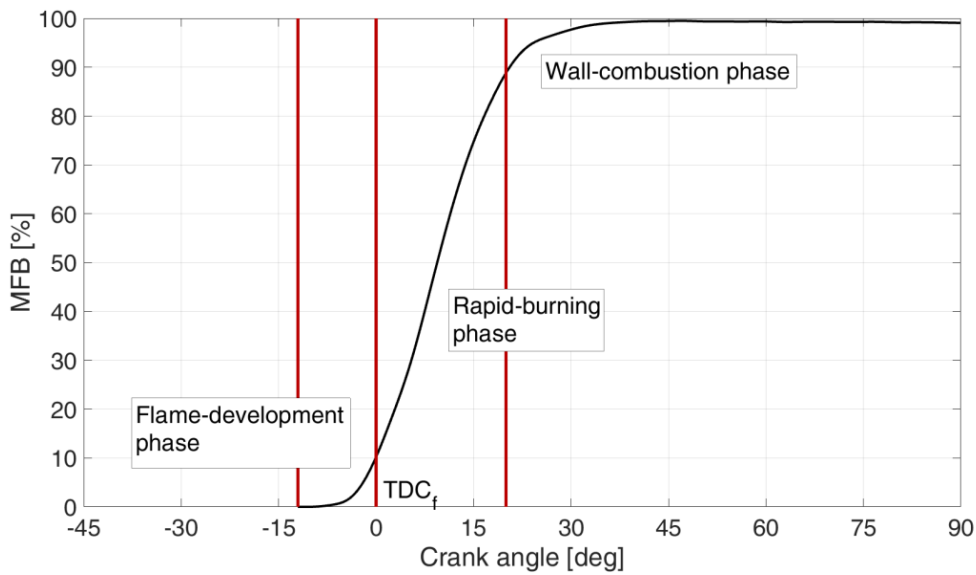
Figure 5.1: Example of mass fraction burned

In SI engine, the combustion process is strictly affected by the charge composition and by in-cylinder flow field. The charge composition affects the flame propagation speed. The laminar flame speed (S_L, flame propagation into quiescent condition) and flame thickness (δ_L) are indeed function of temperature, pressure and composition of the fresh charge. The flame thickness is indeed evaluated as the ratio between the molecular diffusivity (D_L) and the laminar flame speed. Experimental evidence [1] connects the flame front shape and propagation with the charge motion. As a matter of fact, the spherical flame front propagates in the first phase with a non-corrugated surface then is affected by the turbulence intensity in the rapid burning period (corrugated one). A larger flame front surface area leads to greater fresh mixture crossing the flame, thus to higher flame speed propagation (for a given laminar flame speed). Turbulence is hence briefly explained. Considering a steady turbulent flow, the instantaneous local fluid velocity can be written as:

$$U(t) = \bar{U} + u(t) \tag{5.1}$$

Where $\bar{U}$ is the time average of U(t) during period τ. The turbulent intensity is instead defined as:

$$u' = \lim_{\tau \to \infty} \left(\frac{1}{\tau} \int_{t_0}^{t_0 + \tau} u^2 \, dt \right)^{1/2} \tag{5.2}$$

The turbulent premixed flames are affected by the turbulence intensity (RMS of flow velocity fluctuation and by the various length scales of the turbulent flow: from large eddies (Integral length scale, l_I) to smallest ones, which are dissipated by viscosity (Kolmogorov length scale, l_K). The interaction between premixed flame front and in-cylinder turbulence is evaluated. The flow field is evaluated by means of the turbulent Reynolds number:

$$Re_T = \frac{u' l_I}{\nu} \tag{5.3}$$

Where ν is the kinematic viscosity. As a matter of fact, the integral and the Kolmogorov length scales are correlated by means of Eq. 5.3, for homogenous and isotropic turbulence (for detailed explanation see [1], Chapter 8.2.1):

$$\frac{l_K}{l_I} = Re_T^{-3/4} \tag{5.4}$$

Characteristic turbulent eddy turn over time (τ_T) and characteristic chemical reaction time (τ_L) can be defined as:

$$\tau_T = \frac{l_I}{u'} \quad \tau_L = \frac{\delta_L}{S_L} \tag{5.5}$$

The ratio between the abovementioned times is called Damköholer number:

$$Da = \left(\frac{l_I}{u'} \right) \left(\frac{S_L}{\delta_L} \right) = \left(\frac{l_I}{\delta_L} \right) \left(\frac{S_L}{u'} \right) \tag{5.6}$$

The inverse of dimensionless Damköholer parameter describes the effects of the turbulence flow on the chemical process. Other two dimensionless parameters are used for premixed turbulent combustion analysis: Karlovitz numbers. The first Karlovitz number represents the characteristic time of laminar flame with respect to Kolmogorov turbulence time scale (τ_η and u_η are the characteristic turn over time of the Kolmogorov scale and the characteristic speed respectively) and is equal to:

$$Ka = \frac{\tau_L}{\tau_\eta} = \frac{\delta_L{}^2}{l_K{}^2} = \frac{u_\eta{}^2}{S_L{}^2} \qquad (5.7)$$

Typically, the molecular diffusivity is equal to the kinematic viscosity. Thus, turbulent Reynolds number could be expressed as function of Damköholer number and first Karlovitz number:

$$Re_T = Da^2 Ka^2 \qquad (5.8)$$

The second Karlovitz number is correlated with the inner layer of the flame front. As a matter of fact, the structure of a premixed flame can be divided in three zones: a preheat zone in which the fresh charge is heated by exothermic reactions, the abovementioned inner layer (with a width called l_δ) in which the chain-breaking reactions occur and the radical are released and the oxidation layer in which the oxidation reactions take place [4] (Figure 5.2). The second Karlovitz number takes hence into consideration the effects of the Kolmogorov turbulence scale on the inner layer of the flame. It is equal to (referring to the data in Figure 5.2):

$$Ka_\delta = \frac{l_\delta{}^2}{l_K{}^2} = \delta^2 \frac{\delta_L{}^2}{l_K{}^2} = \delta^2 Ka^2 \qquad (5.9)$$

Finally, Reynolds number could be expressed as function of Damköholer number and second Karlovitz number:

$$Re_T = Da^2 Ka_\delta{}^2 \qquad (5.10)$$
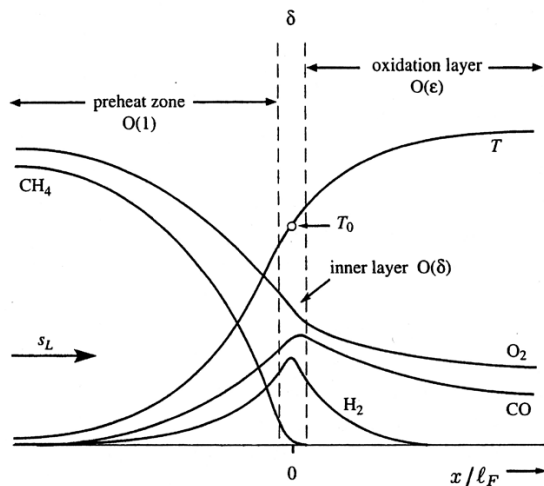
Figure 5.2: Structure of a premixed methane-air flame [4]

The effects of the turbulent flow (considering all the length scales) on the different zones of the flame front can be summarized in the so-called "Borghi diagram" shown in Figure 5.3 [5].
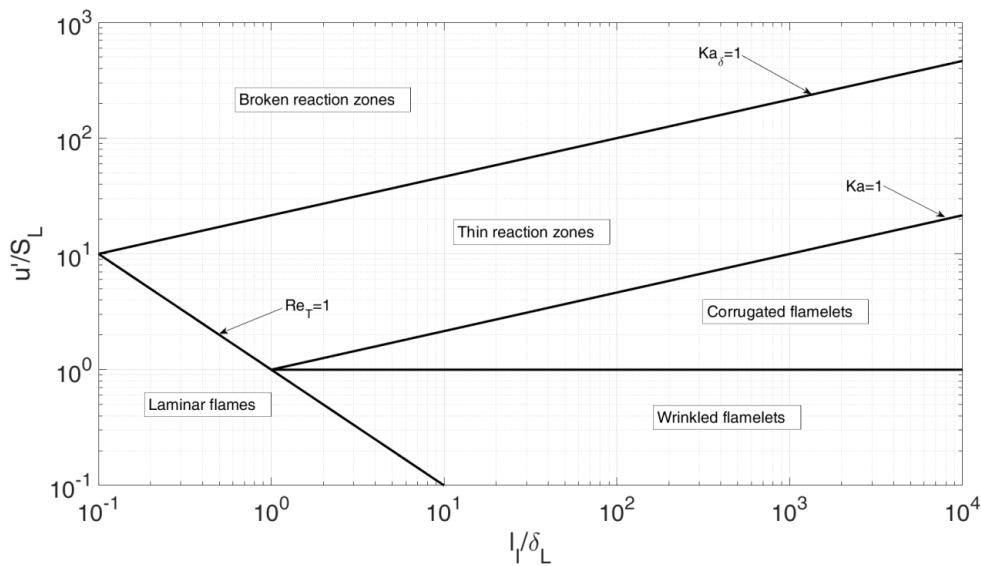
Figure 5.3: Borghi diagram [5]

Different connection between turbulent flow and premixed flame front can be highlighted. With negligible flow pattern the Re_T is lower than unity and flame propagates in laminar way. The other regions are affected by the ratio between the turbulence intensity and laminar flame speed: if the ratio is lower than the unity, the flow pattern doesn't affect the combustion propagation and produces

a wrinkling effect. If the ratio is greater than unity, larger the ratio higher the number of eddies that affects the flame front. In the corrugated flamelets zone the flame front surface is increased and the flame propagates with a speed higher than laminar one: it proceeds with a fictitious turbulent speed (S_b), considering a spherical unchanged flame front. When Ka=1, the Kolmogorov length scale has the same order of magnitude of the flame thickness. Therefore, whole flow pattern corrugates the flame, from larger eddies (integral length scale) to lower ones (Kolmogorov length scale). For higher in-cylinder turbulence, (Ka>1), a fraction of the smaller eddies has a characteristic length scale lower than flame thickness. These eddies influence the preheated layer by enhancing the heat exchange and thus boosting the flame front propagation speed (thin reaction zone). Finally, with an exalted turbulence flow field, a part of the smaller eddies has a characteristic length scale smaller than inner layer thickness (Ka_δ>1). The reactions occurring in the inner layer are obstructed by the smaller eddies. Therefore, in the broken reaction zones the flame propagation speed is lowered. Typically, commercial ICE operates in corrugated flamelets region.

The chemical and physical properties of the air, fuel and residual gas mixture affect the laminar burning speed. As a matter of fact, the flame propagation depends on the chemical reaction in the inner layer region (chemical properties) and on the heat exchanged in the preheat zone (physical characteristics). The laminar burning speed could be defined as:

$$S_L = \omega \frac{dm_b/d\theta}{A_f \rho_u} \tag{5.11}$$

Where ω is the engine speed, m_b the burned gas mass, A_f the flame area and ρ_u the unburned gas density. In research activities shown in this thesis, premixed combustion of air-CNG mixture is considered. Finally, laminar burning speed of compressed natural gas can be estimated depending on pressures, temperatures, relative air-to-fuel ratios and residual gas fractions (X_{res}) occurring in the chamber.

Combustion behavior during flame development phase depends on several parameters. The main sources are spark characteristics and in-cylinder flow pattern and mixture properties near spark-plug region [6, 7]. The first stage of flame development phase (flame initiation) is characterized by spark initialization due to a voltage rise between the electrodes of the plug, which

produce an electrical breakdown ($\approx$ 10 ns), then an electrical discharge ($\approx$ 100 µs) and finally the glow phase. The first two stages initiate the spark event, whereas the glow phase sustains the flame propagation. However, the flame initiation is affected by the mixture quality in the spark plug gap, which affects the spark ignition due to its conductivity. Moreover, the electrical discharge is enhanced by in-cylinder flow near the spark plug, which distorts the spark ark and increases the energy transfer [8].

Premixed combustion phenomenon during rapid burning phase is hence affected by air-to-fuel mixture properties (affecting laminar burning speed) and by in-cylinder flow pattern. In the flame development phase, the combustion is instead affected by mixture properties (air, fuel and residual gas fraction) and flow pattern in the spark plug region. All the above-mentioned parameters are however affected by a cycle-to-cycle variation [1, 6, 9-11]. As a matter of fact, induced air, injected fuel mass and released residual gas are different at each cycle thus affecting in-cylinder flow pattern and mixture composition. Dispersion in incoming and outgoing in-cylinder mass flow rates influences the in-cylinder turbulence intensity, introducing cyclic variability of flame development phase duration and flame front distortion. Moreover, mixture composition is different at each engine cycle and is certainly spatially non-homogenous, affecting whole combustion phase.

Predictive numerical model for combustion and CCV simulation has to be designed by taking into consideration the physics of the premixed combustion phenomenon. Model reliability in whole engine operating conditions could be indeed guaranteed. The adopted models are shown in section 5.2.

5.1.2 Knock and ringing phenomena

Knock is the sound produced by the engine's block when it's excited by the pressure waves caused by the auto-ignition of a portion of the end-gas [1, 12]. Knocking combustion depends on several factors. Pressure and unburned gas temperature history are the most significant, correlated with air, fuel and residual gas composition and thus on chemical properties of the mixture. As a matter of fact, induction time of a fresh charge depends on its chemical characteristics at given values of pressure and temperature. Indeed, methane-air mixture has a single high-temperature ignition limit [1]. Considering auto-ignition phenomenon in SI engine, mass fraction burned rate affects auto-ignition too. This phenomenon typically occurs near the angle of the peak firing pressure in zone of the in-cylinder chamber in which the unburned gas

reaches the highest temperature and has the proper composition. The instantaneous combustion of a portion of the charge produces an impulse excitation of the system generating pressure waves inside the chamber [13]. Knock phenomenon is hence detected due to oscillation of the in-cylinder pressure signal or due to engine's block vibrations produced by pressure waves [14]. Figure 5.4 shows the in-cylinder pressure data of a knocking cycle. Pressure waves produced by auto-ignition have resonance modes at different frequencies with different shapes, depending on geometric characteristics of SI engine. First natural frequency (circumferential mode) is the base oscillation of the pressure waves, which survives for a longer time than others. Typically, this oscillation is transmitted to engine block. Highest natural frequencies appear at beginning of auto-ignition phenomenon and rapidly decay.
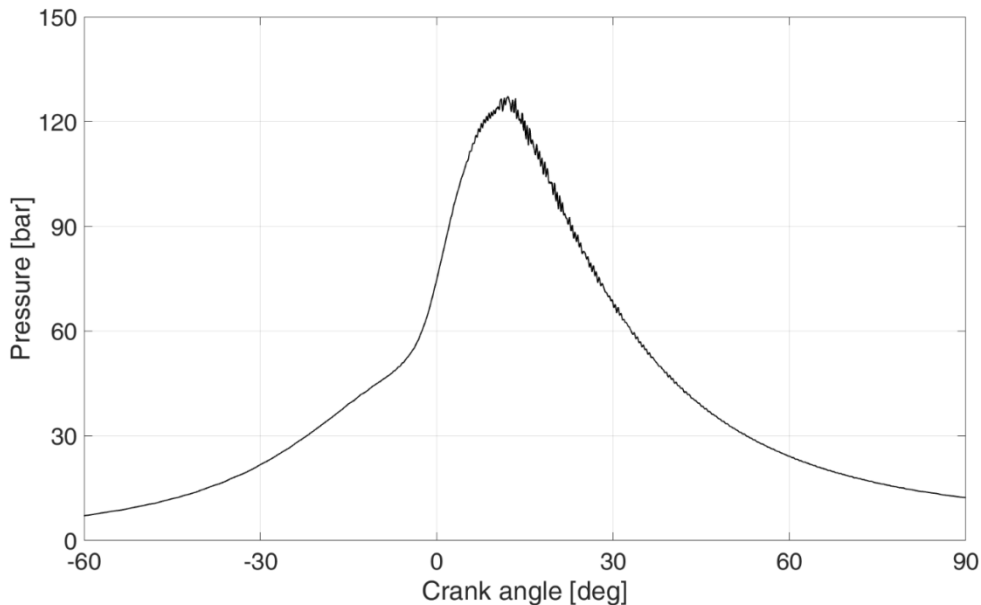
Figure 5.4: Knocking cycle

Knock phenomenon is highly dependent on cyclic variability. Pressure, temperature, mixture composition and combustion phenomenon are different at each cycle. Faster cycles lead to higher pressure and temperature and hence are more inclined to reach auto-ignition, but flame geometry due to corrugation affects knock propensity. Therefore, operating conditions could be divided into three zones, due to CCV: non-knocking conditions, borderline knock conditions and knock combustion ones [12]. Amplitude of pressure waves depends on the amount of charge that ignites, thus leading to relevant oscillation during knock combustion conditions. Engine control strategies are

designed in order to prevent knock combustion operating conditions and set borderline knock conditions as operating limit. During borderline conditions however, number of knocking cycles and amount of pressure waves are poor. Numerical models have to be modeled in order to operate properly mainly in non-knocking conditions and borderline ones. In natural gas SI engine, pressure waves could be produced by a different phenomenon, ringing. Ringing refers to pressure waves produced in dual fuel engine during pre-mixed combustion or in HCCI combustion [15-17]. It happens casually during normal combustion event and typically the amplitude of the pressure oscillation depends on the amount of burned fuel mass. However, the abovementioned phenomenon has been identified only during compression ignition combustion. In experimental tests shown in next chapter on a CNG SI engine with high CR (CR~13), ringing has been detected. Probably, pressure waves have been produced by high heat release rate due to overlap of combustion with compression phase. Gasoline engine never reached indeed a rapid increase of in-cylinder pressure (due to relevant heat released) because of major propensity to auto-ignition than methane. Pressure waves produced by ringing in analyzed engine start before angle of peak firing pressure, whereas knock occurs in PFP region, as shown in Figure 5.5. Moreover, characteristic frequencies of ringing phenomenon differ from knock ones, depending on engine geometry (examples will be shown afterwards).
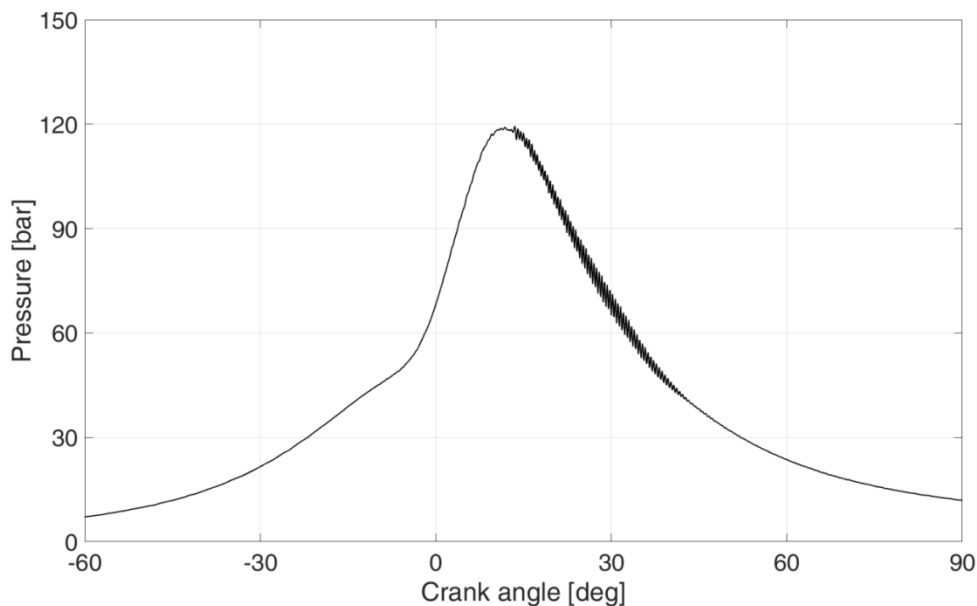

Figure 5.5: Ringing cycle

Reliable models for knock detection and ringing recognition have to be analyzed. They will be useful both for experimental tests and for auto-ignition prediction model calibration.

5.2 Numerical models for Combustion, CCV and auto-ignition prediction in CNG SI engine

Numerical models for combustion, CCV and auto-ignition prediction are mandatory for knock onset estimation and could reduce experimental campaign. A knock prediction model needs a correct estimation and simulation of the average in-cylinder pressure. Moreover, knock and CCV are strictly correlated, thus requiring a numerical model for reliable cyclic variability simulation. Numerical models used in the research activity are shown in next sections.

5.2.1 Fractal predictive combustion model

The physics of the premixed combustion phenomenon has been considered for the implementation of a predictive numerical model for combustion and CCV simulation. A 0D-1D numerical model has been used, evaluating the rate of burned mass fraction in order to reproduce the in-cylinder pressure. 0D-1D fractal model has been selected instead 3D ones in order to achieve an acceptable and detailed description with an acceptable time requirement. Eq. 5.11 shows the relationship between laminar flame speed and rate of mass fraction burned. Considering a spherical burning area (A_b), Eq. 5.11 can be written (considering a hypothetic turbulent flame speed S_b) as:

$$S_b = \omega \frac{dm_b/d\theta}{A_b \rho_u} \qquad (5.12)$$

Combining Eq. 5.11 and 5.12 gives:

$$S_b A_b = S_L A_f \qquad (5.13)$$

The predictive combustion model analyzed in [18-23] has been implemented in GT-Power environment. Turbulent burning speed is evaluated according to the fractal theory [24, 25]:

$$\frac{A_f}{A_b} = \frac{S_b}{S_L} = \left(\frac{\varepsilon_o}{\varepsilon_i}\right)^{D-2} \tag{5.14}$$

The ratio between A_f and A_b is the flame surface area distortion (as explained in Chapter 5.1.1). The flame corrugation is estimated due to fractal geometry characterization. The inner cutoff length scale is considered equal to the Kolmogorov one, therefore:

$$\varepsilon_i = l_K = l_i \left(\frac{u' l_i}{v}\right)^{-3/4} \tag{5.15}$$

The integral turbulence scale is the size of the large-scale eddies and could be assumed to be proportional to the in-cylinder main principal distance. It is proportional to the sum of chamber clearance at the TDC and the piston position from TDC.

$$L_i = C_L\left(h_{min} + S_p\right) \tag{5.16}$$

For the outer cutoff length scale, the integral length scale has been replaced with a characteristic linear dimension of the flame front ($\sqrt{A_b}$). Turbulence distortion on flame front is indeed a function of ratio between flame front and eddies dimensions. Finally, considering the microscale turbulence effects on the heat and species transfer through burning front, the ratio between the turbulent burning speed and the laminar one could be estimated by the following formula [20]:

$$\frac{S_b}{S_L} = \left(\frac{\rho}{\rho_0}\right)^n \left(\frac{C_L\sqrt{A_b}}{C_L\left(h_{min} + S_p\right)\left(\frac{u'C_L\left(h_{min}+S_p\right)}{v}\right)^{-3/4}}\right)^{D-2} \tag{5.17}$$

Spherical flame front data has been produced with a CAD model depending on engines' layouts. Combustion model evaluation depends on the turbulence

intensity. It is evaluated by means of the modified K-k model [21, 23- 27], based on the 0D energy cascade theory. The zero-dimensional code takes into consideration the effects of the mass flow rates flowing inside and outside the cylinder and the injected compressed natural gas, with a set of ordinary differential equation for the evaluation of the mean flow kinetic energy ($K = \frac{1}{2} m U^2$) and turbulence kinetic energy ($k = \frac{3}{2} m u'^2$):

$$\frac{dK}{dt} = C_{in} \frac{1}{2} \dot{m}_\iota v_i{}^2 - P - K \frac{\dot{m}_0}{m} + K \frac{\dot{\rho}}{\rho} + C_{GDI} \frac{1}{2} \dot{m}_{inj} v_{inj}{}^2 \qquad (5.18)$$

$$\frac{dk}{dt} = P - m\varepsilon - k \frac{\dot{m}_0}{m} + k \frac{\dot{\rho}}{\rho} + C_{GDI} \frac{1}{2} \dot{m}_{inj} v_{inj}{}^2 \qquad (5.19)$$

With $\varepsilon = C_\alpha u'^3 / l_i$ the rate of turbulent kinetic energy dissipation, $\dot{m}_\iota$ and $\dot{m}_0$ the mass flow rates flowing inside and outside the cylinder, v_i the entering speed, P the rate of turbulent kinetic energy production, m the in-cylinder mass, $\dot{m}_{inj}$ the mass flow rate due to injection and v_{inj} the speed of the injected gas. P is evaluated as follows:

$$P = 0.3307 C_\beta \frac{K}{l_I} \left(\frac{k}{l_i}\right)^{1/2} \qquad (5.20)$$

Part of the proportional coefficients previously presented will be calibrated on few steady state cases for each engine layout. The other coefficients will be set considering literature suggestions [18-27]. The abovementioned models need some corrections in order to proper describe the physics of the considered phenomena. Firstly, the propagation of the flame front cannot be described with the fractal theory. Although combustion behavior during kernel growth phase should be connected with spark characteristics and in-cylinder flow pattern and mixture properties near spark-plug region, the implemented model calculates the angular period between SA and crank angle in which mass fraction burned reaches 1% ($\Delta\theta_{0-1\%}$) [28]. Although a correct estimation of mass fraction burned shape within the $\Delta\theta_{0-1\%}$ would be preferable, the energy content released is negligible. Even though we accepted an error on the trend, the most important consideration is the $\Delta\theta_{0-1\%}$ period. By means of

experimental analysis, a regression for the evaluation of abovementioned period has been extrapolated depending on the thermodynamics conditions at the SA. Hence, a polynomial characterization of the mass fraction burned was used. Secondly, wall-combustion phase has been modeled by means of wall-combustion sub-model shown in [21, 23] so as to correctly model the heat released in the final stage. At a precise value of MFB (c_{wc}) the combustion is evaluated as follows:

$$
\left(\frac{dm_b}{dt}\right) = \left(\frac{m - m_b}{(m - m_b)_{c_{wc}}}\right)\left(\frac{dm_b}{dt}\right)_{fractal} + \cdots
$$
$$
+ \left(1 - \frac{m - m_b}{(m - m_b)_{c_{wc}}}\right)\left((A_b \rho_u S_b)_{c_{wc}}\left(\frac{m - m_b}{(m - m_b)_{c_{wc}}}\right)\right)
\tag{5.21}
$$

The calibrated steady state points have been used in order to find the proper correlation of three parameters. Correlations are required to guarantee correct model accuracy due to 0D-1D evaluation [23]. Results will be shown in next section. The parameters that need a correlation will be:

- C_L: parameter for turbulent flame speed and turbulent intensity correlation
- $\Delta\theta_{0-1\%}$: period between SA and 1% of MFB
- c_{wc}: switch from pure fractal combustion to fractal and wall combustion

Typically, laminar burning speed of methane is evaluated by means of Metghalchi's correlation [29], as a function of pressure, temperature, relative air-to-fuel ratio and residual gas fraction. In order to improve the model reliability, CNG laminar flame speeds (for different fuel blend) have been estimated by means of model based on GRI Mech 3.0 reaction mechanism [30]. The model estimates laminar speed as a function of the abovementioned inputs. It's able to extend the range of reliability of laminar flame speed estimation. As a matter of fact, empirical relations cannot achieve acceptable results at high-pressure and high-temperature conditions (pressure ranging from 40 bar to 120 bar and unburned temperature up to 1000 K) [31, 32].

5.2.2 CCV applied to fractal combustion model

The cyclic variation in SI ICE has different causes [1, 6] mainly ascribed to: goodness of air-fuel mixture especially near the spark plug, variations of the

amount of air, fuel and residual gas and finally variation in the in-cylinder gas motion. The abovementioned causes mainly affect the kernel growth period and the turbulent flame speed. Although these are three-dimensional phenomena which could be modeled with large eddy simulation (LES) [33, 34], 0D model has been proposed. As a matter of fact, LES is highly demanding from computational point of view both in time and computational power required. CCV has been hence modeled by introducing in the GT-Power environment a proper perturbation of combustion parameters depending on ICE operating conditions. Model parameters perturbation has been proposed also in [35, 36]. The novelty of this research activity is the perturbation of $\Delta\theta_{0-1\%}$ and C_L. The former is indeed the development phase period and CCV is mainly affected by the duration of the first phase [6, 37, and 38]. The latter refers to the correlation between turbulent flame speed and turbulent intensity: cycle-by-cycle variation of flow pattern change flame corrugation and hence turbulent flame speed. A normal distribution has been imposed to the two parameters of predictive combustion model by imposing proper COV correlated to engine operating conditions:

$$COV_{\Delta\theta_{0-1\%}} = \frac{\sigma_{\Delta\theta_{0-1\%}}}{\mu_{\Delta\theta_{0-1\%}}} \quad COV_{c_L} = \frac{\sigma_{c_L}}{\mu_{c_L}} \tag{5.22}$$

At the beginning of computation, the two parameters are fixed and equal to the corresponding steady state values. Normal distribution with a proper standard deviation ($\sigma = COV * \mu$) is set to $\Delta\theta_{0-1\%}$ and C_L when the model reaches numerical stability. Although a numerical instability is introduced in order to mimic physics instability, relationship of previous parameters with combustion physics aspects is considerable. Moreover, correlation of COV with engine operating conditions guarantees the predictability of the model. Correlations have been found by calibrating input COVs under few selected steady state points by targeting PFP COV. Results will be shown in next chapter.

5.2.3 Models for knock detection and prediction

Ignition process (in combustion chamber) is a complex reacting mechanism in which a large number of chemical reactions occur [1]. During initiating stage, a large number of radicals is released. Then radicals react with reactants producing products and other radicals. Finally, process ends when "*chain propagating radicals are removed*" [1]. The so-called chain-branching phenomenon is strictly correlated to chemical hydrocarbon-air mixture

properties. Mixture of CNG and air shows a single-stage ignition process as shown in Figure 5.6. Single-stage process leads to uniquely-defined induction times, function of pressure and temperature of fresh mixture
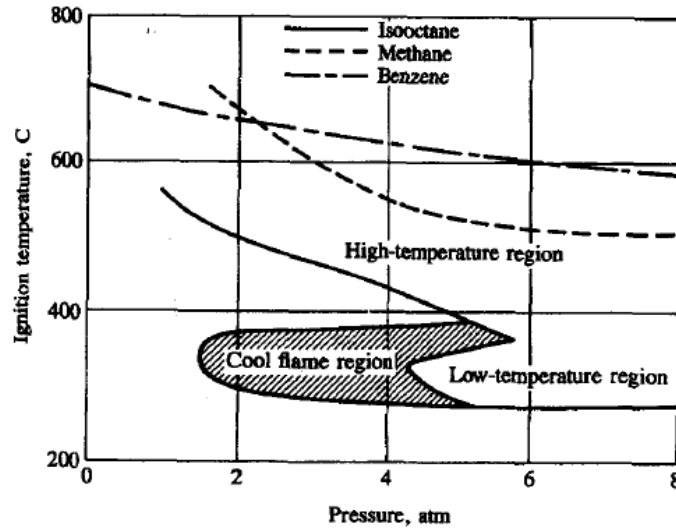
Figure 5.6: Ignition diagram for different fuels [1]

Auto-ignition process in CNG engines could be effectively evaluated by calculating induction times. Development of the model starts with the relation between ignition delay (τ_a) pressure and temperature due to Arrhenius law [39-45]:

$$\tau_a(p, T_u) = Ap^{-n}e^{\frac{B}{T_u}} \tag{5.23}$$

The reactions accumulation could be described by a function $\phi(t)$ and auto-ignition occurs at critical value ϕ_c. Considering chain-branching theory, auto-ignition occurs after a time τ_a when accumulation of reactions reaches critical value. Moreover, reaction rate could be described as:

$$\frac{d\phi}{dt} = f(\phi, p, T_u) \cong \frac{\phi_c}{\tau_a} \tag{5.24}$$

Hence, "Auto-ignition integral" could be written as:

$$\frac{\phi}{\phi_c} = \int_{t_0}^{t} \frac{dt}{\tau_a(p, T_u)} \tag{5.25}$$

Knock onset occurs when auto-integral reaches the unity:

$$\int_{t_0}^{t_{KO}} \frac{dt}{Ap^{-n}e^{\frac{B}{T_u}}} = 1 \tag{5.26}$$

Ignition delay depends on pressure and temperature of unburned gas. The three coefficients of induction time depend on engine fuel. They have been calibrated due to a heat release rate analysis and knock detection tool. As a matter of fact, experimental data of engine running in borderline knock conditions have been used for model calibration. In-cylinder pressure data have been acquired. Heat release rate model based on multi-zone approach [46] has been used in order to evaluate combustion characteristics (mass fraction burned and temperature of unburned gas) that are useful to use the first model. Multi-zone model evaluates mixture which is divided in three or more zones. Mass and energy conservation law are applied for each zone in which the volume is divided.

Heat release rate outputs have been used as numerical inputs for auto-ignition integral during calibration. The integral has been calibrated using a full factorial DOE for A, n and B values, by targeting knock onset prediction, similarly to [44, 45]: integral value at end of combustion (EOC) analytically discriminates knocking and normal cycles. Integral has been calculated considering experimental pressure data, unburned temperature and EOC deriving from heat release rate model. Starting time has been set equal to EOI or EOC (tested engine is a DI, engine characteristics will be shown during next chapter); latest one has been selected. Analytical discrimination has been compared with experimental results. Experimental in-cylinder data of each cycle have been acquired and knock occurrence has been detected. Starting values for abovementioned parameters has been evaluated starting from findings of [42-45], for two fuel blends as shown in Table 5.1.

Table 5.1: CNG fuels

Fuel	Elements	Mole fraction [%]
1st	Methane	95
	Ethane	2.9
	Propane	0.8
	Nitrogen	0.5
	Carbon dioxide	0.5
	Others	0.3
2nd	Methane	87
	Ethane	13

Knock detection model has been carefully used in order to discriminate experimental knocking cycles and normal ones, considering ringing phenomenon. Cycles shown in Figure 5.4 and 5.5 are tested to show the adopted methodology. Experimental in-cylinder pressure data have been filtered with a zero-phase digital band-pass filter. For evaluated engines, which will be further described (light-duty engines, 4 in-line cylinders and 1368 cm^3), lower and upper cutoff frequencies have been set to 5 kHz and 30 kHz. It is worth highlighting that the sampling frequencies are fixed by utilized crank angle resolution: for selected 0.1 CA resolution, sampling frequencies range over 60 kHz at 1000 rpm to 330 kHz at 6000 rpm. Filtered pressures, Fast-Fourier Transform (FFT) and Power Spectral density (PSD) of knocking ad ringing cycles previously shown are displayed in Figure 5.7 and 5.8. Pressure waves in knocking cycle occurs near PFP region, as shown in Figure 5.7a and 5.7b, whereas ringing takes place in other phases (Figure 5.8a and 5.8b). Moreover, ringing phenomenon affects mostly higher frequencies, while knock excites all engine natural frequencies [15]. Figure 5.7c and 5.7d show PSD and Single-Sided Spectrum of knocking cycle: four main natural frequencies in 5÷30 kHz range are excited. The four peaks present the same order of magnitude. For a ringing cycle (Figure 5.8c and 5.8d) higher natural frequencies are mostly excited and hence PSD's peaks of higher frequencies

are an order of magnitude bigger than the others. Taking into consideration knock index (KI) parameter [47] for knock detection, an advanced tool has been used.
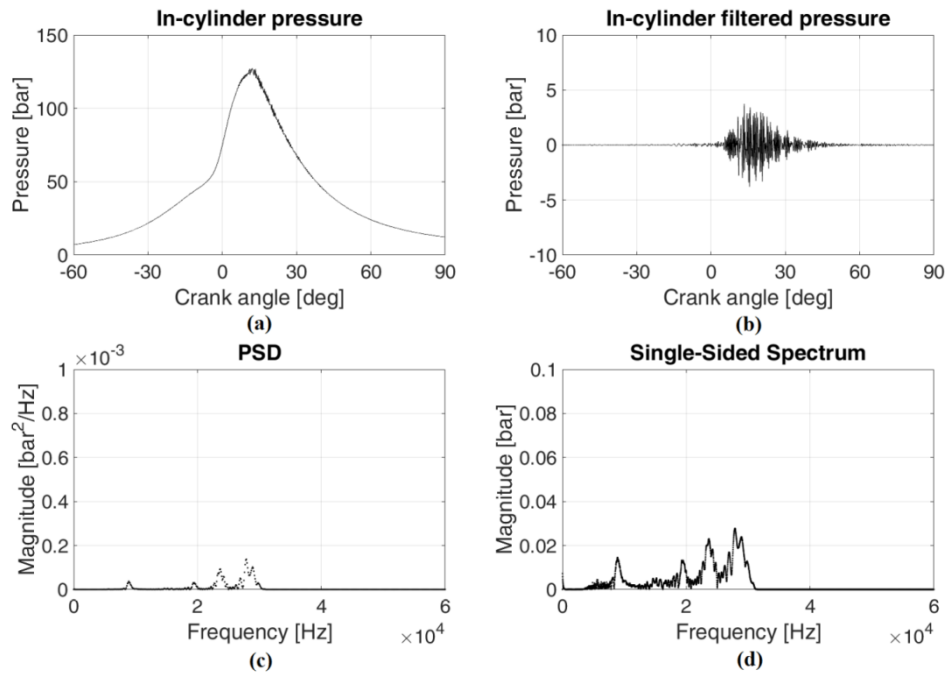

Figure 5.7: Actual pressure, filtered pressure, power spectrum and single-sided spectrum of knocking cycle
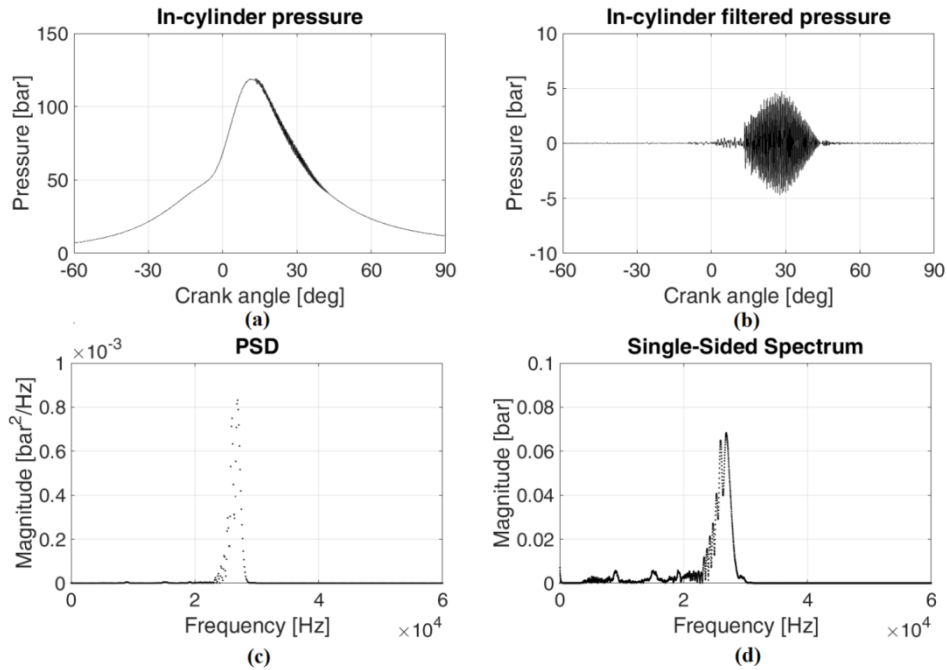
Figure 5.8: Actual pressure, filtered pressure, power spectrum and single-sided spectrum of ringing cycle

The integral of the absolute value of the time derivative of the band-pass filtered pressure signal has been used [47]:

$$KI = \int \left| \frac{dp_{bpf}}{dt} \right| dt \qquad (5.27)$$

Value of each cycle is compared with a reference threshold, typically two times average value of knock index of whole population during normal combustion. Figure 5.9 shows KIs for engine working in borderline knock conditions; figure shows data for four cylinders and two-hundred cycles for each one. Unfortunately, knock detection estimation with KI is reliable if ringing doesn't occur. As a matter of fact, ringing cycles are counted as knocking ones. Therefore, cycles with a KI higher than selected threshold are further analyzed.
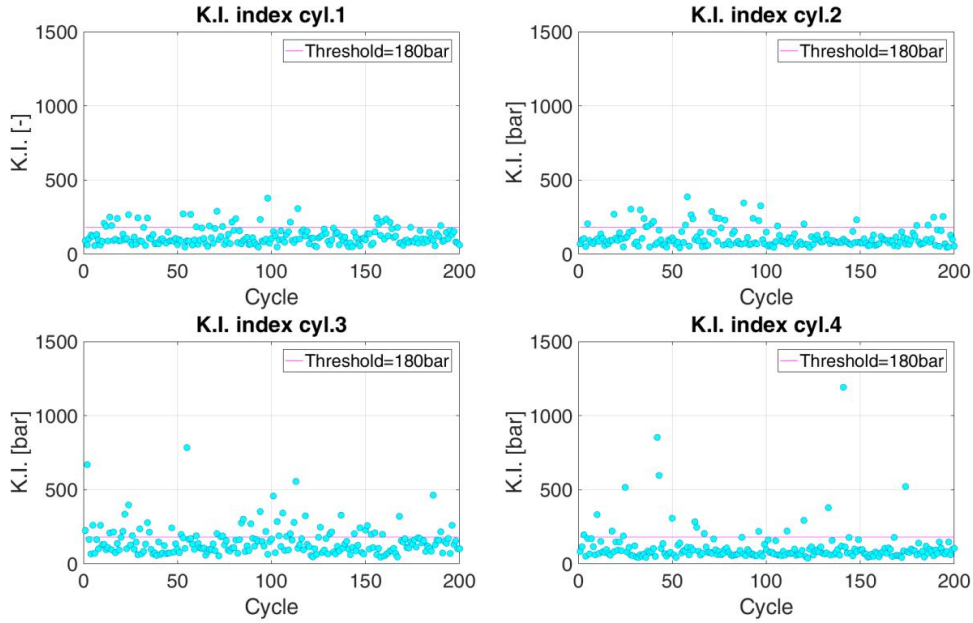
Figure 5.9: KIs for borderline knock conditions

Detection has been improved by thoroughly analyzing frequency content of both ringing and knocking cycles. Indeed, ringing phenomenon mostly excites frequencies between 22 and 29 kHz. Therefore, proposed model computes ratio of two integrals of the single-sided spectrum of the band-pass filtered pressure: first one between lower and upper cutoff frequencies, second one between 22 and 29 kHz. The ratio of the two integrals is compared with an empirical threshold ($r_{threshold}$=0.9).

$$r = \frac{\int_{22\,kHz}^{29\,kHz} P_{bpf}(f)df}{\int_{f_L}^{f_U} P_{bpf}(f)df} \tag{5.28}$$

Considering cycles with KI higher than selected KI threshold, knocking and ringing cycles could be discriminated due to r parameter. Ringing cycles present a ratio higher then empirical r limit. Auto-ignition integral could hence be calibrated: analytical discrimination is compared with knock detection results. Optimum set of A, B and n has been found with a full factorial DOE: it is the one which produces the lowest numerical misdetection. In [43-45], auto-ignition integral goodness has been evaluated on the base of knock onset position. In this research activity, the evaluation is carried out considering the integral value at EOC: auto-ignition integral value is greater than unity for a

knocking cycle. Therefore, numerical results of each set of parameters have been compared with KI discrimination to find optimum set.

Predictability of knock onset model is guaranteed by auto-ignition integral reliability with CNG engine (due to single stage process, Fig. 5.6) and goodness of fractal combustion model and CCV simulation. This research activity shows the potentiality of this new methodology: 0D-1D model for knock prediction, with a novel CCV estimation applied to fractal combustion model.

5.3 Experimental set-up

Experimental tests have been performed on two different engines at Politecnico di Torino (Corso Duca degli Abruzzi, 24.- 10129 Torino, ITALY), at CRF and at AVL LIST GmbH (Hans-List-Platz 1, 8020 Graz, Austria) laboratories. The research activity has been carried out firstly on a Fiat 1.4 T-Jet turbocharged 1.4-liter light-duty engine designed to run with CNG at Politecnico di Torino, and its characteristics are listed in Table 5.2. The acquisition system has been designed in order to acquire the cycle averaged engine speed and torque, the average pressure and temperature at the compressor inlet and outlet, at the inter-cooler outlet, in the intake manifold, in injection rail and intake runners and at the turbine admission. The air flow rate has been evaluated with a hot-film air mass sensor and the air-to-fuel ratio has been acquired with a UEGO sensor in exhaust system. The in-cylinder pressure data cycles of four cylinders have been collected using four water-cooled KISTLER piezoelectric cylinder pressure sensor transducers with a crank angle resolution of 0.1° in order to correctly describe cyclic variation. Exhaust-gas analyzer has been used in order to measure total hydrocarbons (THC), methane hydrocarbons (MHC), CO_2, CO, NO_x and O_2. Similarly, second engine has been analyzed at CRF and at AVL LIST GmbH. It is an evolution of the first one, with DI, VVA and higher CR upgrade. Due to confidentiality agreement, main engine characteristics will not be shown (i.e. VVA actuation, injection timing, etc.) and significant data will be normalized. However, the main differences are listed in Table 5.2. Prototype engine has been tested in order to achieve knock conditions (knock did not occur in first engine).

Table 5.2: 1.4 T-Jet engine and prototype engine characteristics

Engine	Specifications	Value
1.4 T-Jet	Type	Turbocharged, Vertical In-line, CNG engine
	Bore (mm)	72
	Stroke (mm)	84
	Compression ratio	9.8
	Cylinder number	4
	Displacement (cm^3)	1368
	Injection system type	MPI-Port fuel
Prototype	Type	Turbocharged, Vertical In-line, CNG engine
	Compression ratio	~13
	Cylinder number	4
	Valve actuation	VVA
	Injection system type	DI

First engine has been tested in a wide range of operating conditions in order to analyze numerical models' capability. As a matter of fact, different engine speeds and loads with lambda closed-loop and lambda sweep have been tested. Closed loop operating conditions are summarized in Figure 5.10: a grid of engine speed (2000 rpm, 3300 rpm, 4000 rpm, and 4600 rpm) and loads (2.2 bar, 3.6 bar, 4.4 bar, 6.2 bar, 7.9 bar, 10 bar, 12 bar and 14 bar of bmep) have

been tested in order to distinguish different effects. Moreover, typical ECU's operating conditions have been evaluated. For lambda sweep tests, four engine points have been tested:

- n=2000 rpm bmep=6 bar, λ from 0.7 to 1.6 and step of 0.1
- n=2570 rpm bmep=7.9 bar, λ from 0.7 to 1.7 and step of 0.1
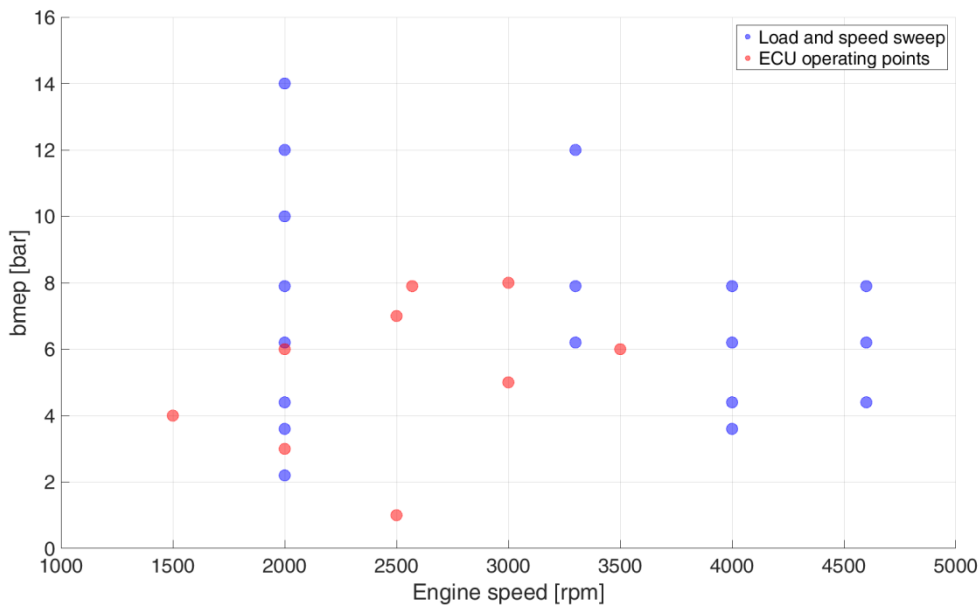- n=3000 rpm bmep=8 bar, λ from 0.7 to 1.5 and step of 0.1

Figure 5.10: Closed loop operating conditions for first engine

It is worth observing that 1.4 T-Jet engine has been fueled with pure methane. Second engine has been tested in full load (FL) and partial load (PL) conditions and normalized cases are shown in Figure 5.11. Engine map points have been tested with first fuel reported in Table 5.1 Borderline knock conditions have been analyzed with SA sweep tests at different engine speeds with different fuels:

- 1750 rpm with second fuel listed in Table 5.1
- 2000 rpm with first fuel listed in Table 5.1
- 3500 rpm with first fuel listed in Table 5.1

Second fuel listed in Table 5.1 has been used in order to enhance knock propensity. As a matter of fact, even with higher CR, borderline conditions were not reachable with normal CNG at 1750 rpm. Moreover, predictive

models capability has been stressed by using three different fuels and two different engines.
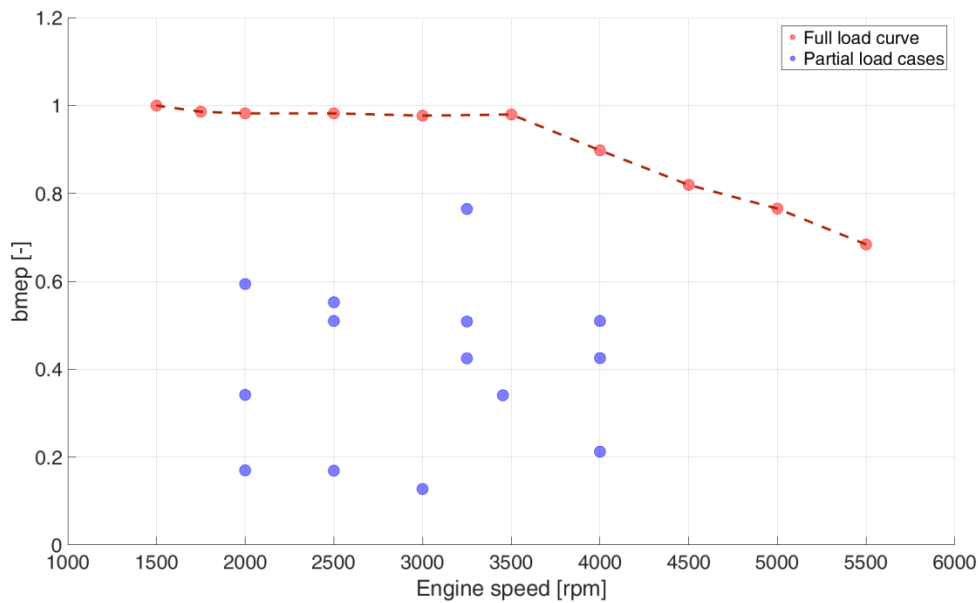

Figure 5.11: FL and PL operating conditions for second engine

5.4 Numerical results for 1.4T-Jet engine

Simulation analysis has been carried out firstly on 1.4 T-Jet engine due to lower degree of freedom (constant valve actuation and port fuel injection). Few operating points were used for combustion, turbulence and CCV model calibration [23]. Other cases have been used for model validation. Afterwards, prototype engine has been modeled and auto-ignition model has been tested.

5.4.1 Calibration and validation of combustion and CCV numerical models

Abovementioned numerical models have been implemented in GT-Power environment. Turbulence model and fractal combustion one need indeed thermodynamic initial conditions (like pressure, temperature, mixture composition, mass flow rate, etc.) and engine functioning parameters (spark advance, injection phasing, boost level, turbocharger working point due to waste-gate (WG) command). Model has been hence built considering experimental data and heat release model results [46]. In-cylinder pressure and temperature are calculated by GT-Power applying energy conservation

equation to n+1 zones due to mass fraction burned evolution calculated by fractal predictive model. Numerical model has been calibrated considering ten closed-loop operating conditions [23] and twelve lambda sweeps cases, listed in Table 5.3. The relative air-to-fuel ratio effect has been indeed extensively studied.

Table 5.3: Calibration cases

Case	Speed [rpm] x bmep [bar]	λ [-]
Closed loop	2000x2.2	1
	2000x3	1
	2000x4.4	1
	2000x6.2	1
	2000x12	1
	2570x7.9	1
	3000x8	1
	3300x6.2	1
	3300x12	1
	4000x6.2	1
Lambda sweep	2000x6	0.7
	2000x6	0.8
	2000x6	1.3
	2000x6	1.6
	2570x7.9	0.7
	2570x7.9	0.8
	2570x7.9	1.5
	2570x7.9	1.6
	3000x8	0.7
	3000x8	0.8

3000x8	1.3
3000x8	1.5

Turbulence model calibration has been extensively verified in [23]. For the sake of brevity, combustion model outputs of three different cases (2000x4 closed loop, 2570x7.9 λ=1.6 and 3000x8 λ=0.7) are displayed in Figures 5.12, 5.13 and 5.14. MFB shapes (Figure 5.12b, 5.13b and 5.14b) depend on turbulence evolution inside the chamber and interaction between flow pattern and flame front distortion, evaluated through C_L value. This coefficient represents indeed the proportionality between outer cutoff length scale dimension and in-cylinder integral length scale. Heat release rate is hence strictly correlated with C_L. Wall combustion effect is instead modeled thanks to c_{wc} implementation: it represents MFB value for which flame front to the chamber walls and quenches. It is worth recalling that in-cylinder pressures (Figure 5.12a, 5.13a and 5.14a) depend on MFB evaluations (pressure cycle is calculated applying energy conservation equation). In-cylinder heat transfer has been previously modeled implementing TPA combustion tool. Indeed, TPA tool imposes a proper combustion rate to guarantee a correct simulated in-cylinder pressure and heat coefficients are properly tuned in order to guarantee energy conservation. Moreover, turbulence intensity is calculated considering Eq. 518, 5.19 and 5.20. Figure 5.15 shows turbulence intensity for the three cases before mentioned.
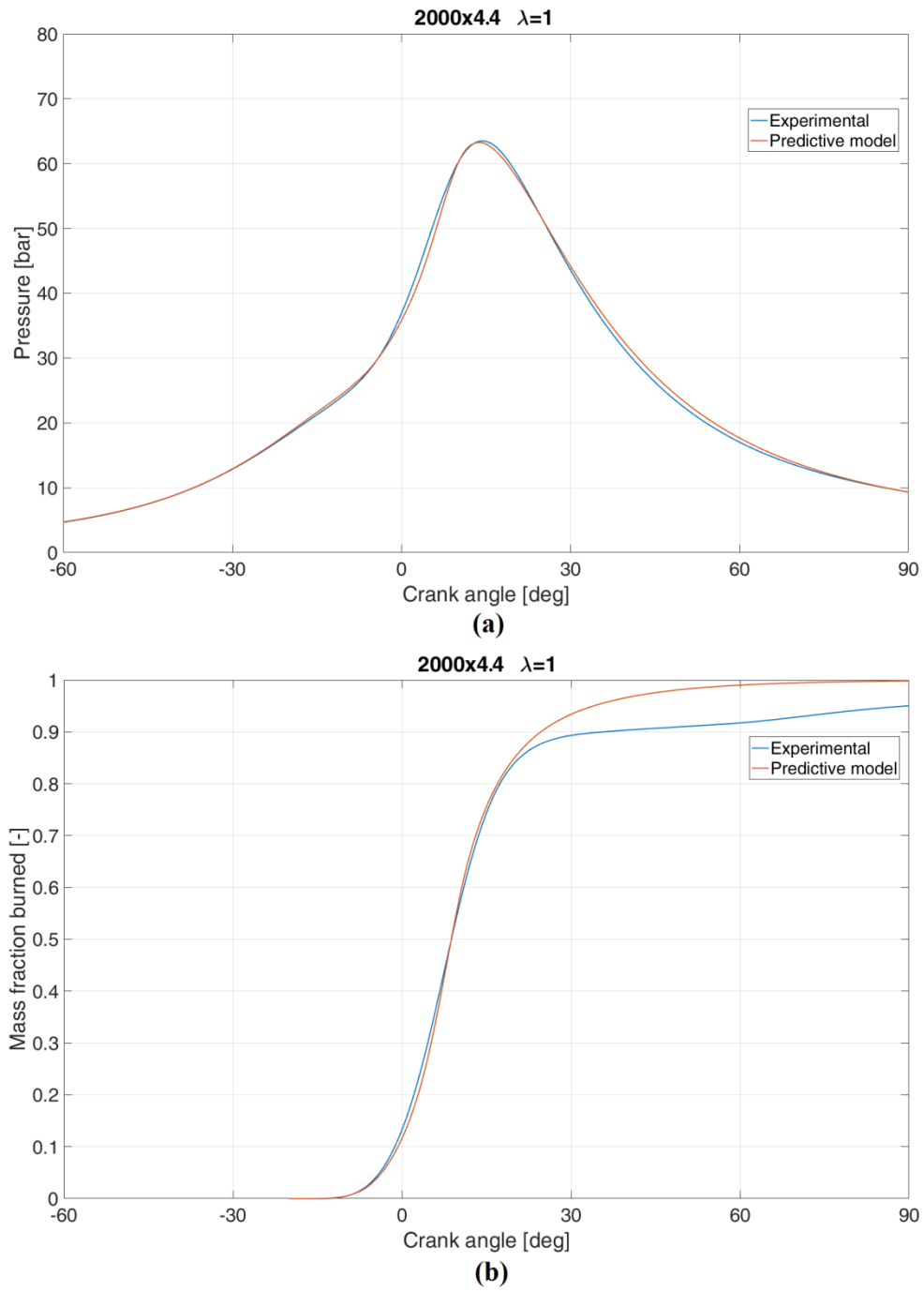
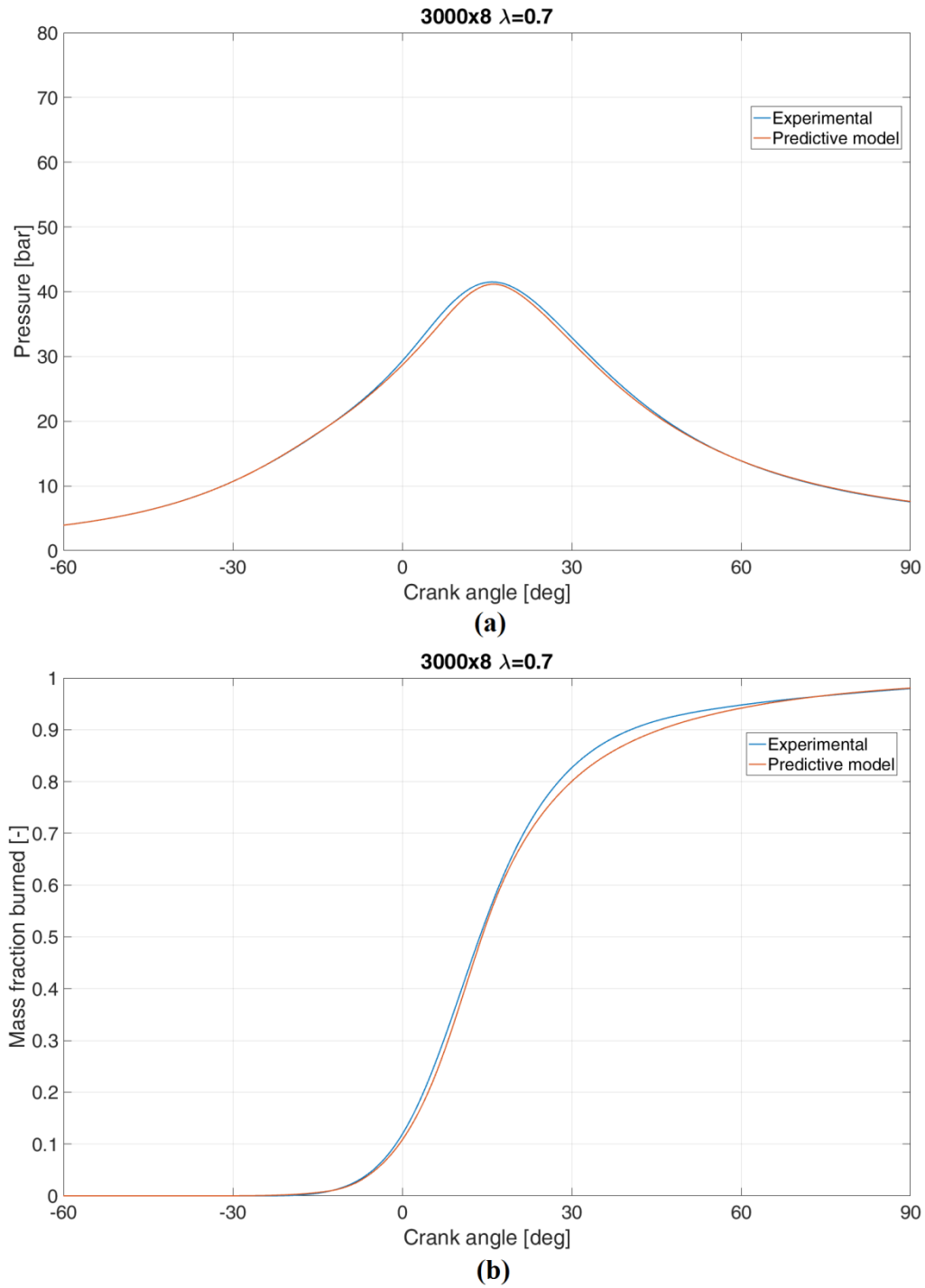Figure 5.12: In-cylinder pressure (a) and mass fraction burned (b) for 2000x4 closed loop point

Figure 5.13: In-cylinder pressure (a) and mass fraction burned (b) for 2000x4 closed loop point
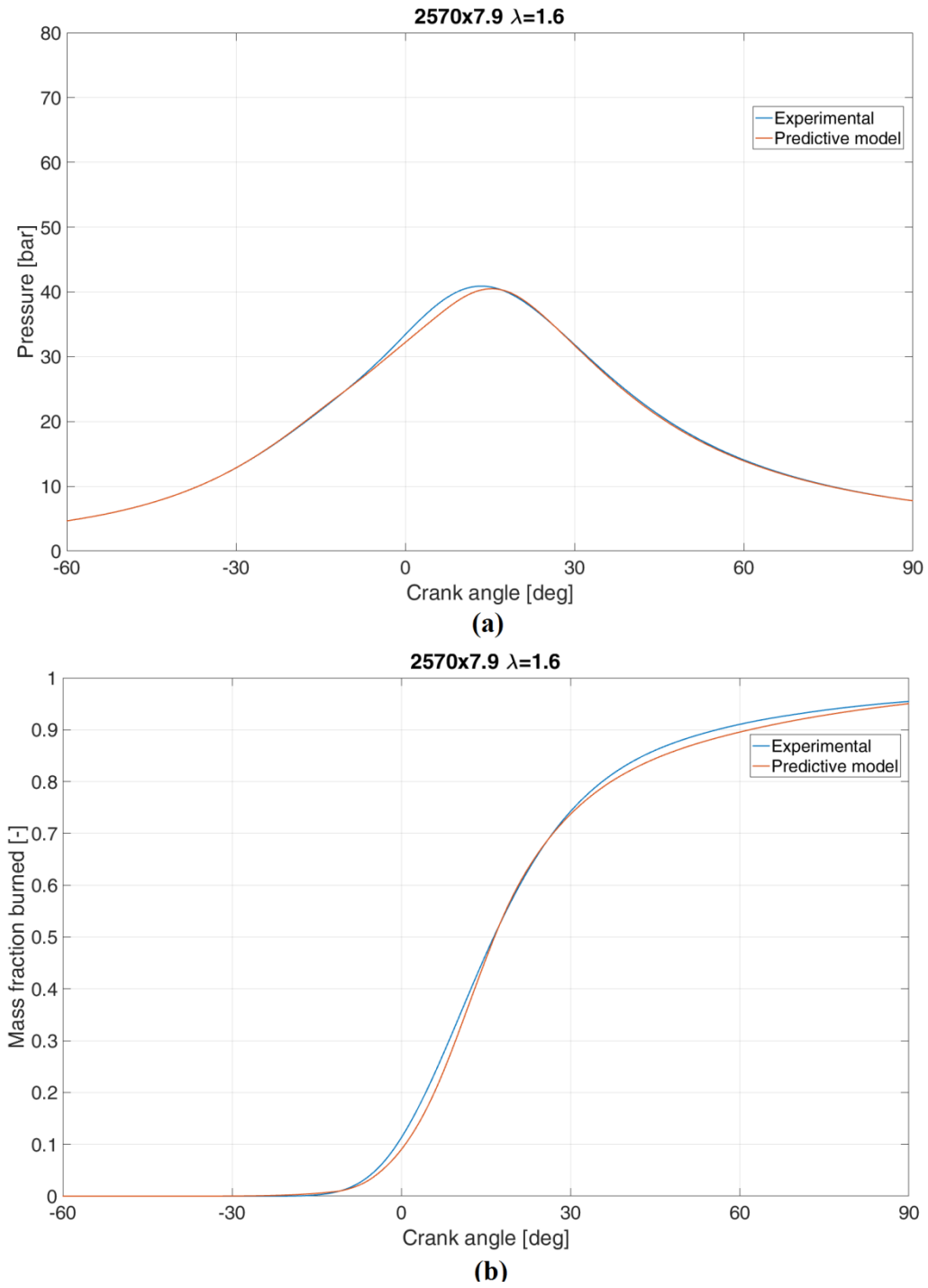
(a)

(b)

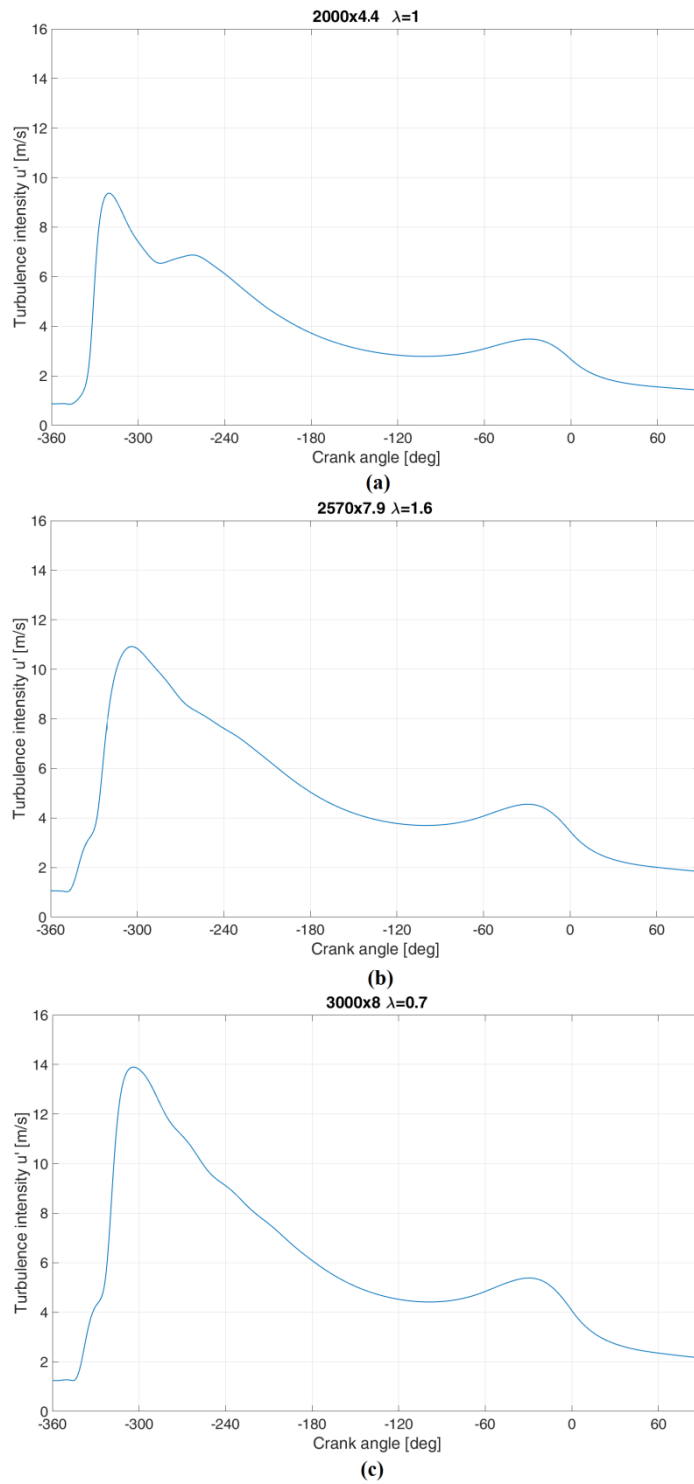Figure 5.14: In-cylinder pressure (a) and mass fraction burned (b) for 3000x8 λ=0.7

Figure 5.15: Turbulence intensity for 2000x4 closed loop (a), 2570x7.9 λ=1.6 (b) and 3000x8 λ=0.7 (c)

MFBs and in-cylinder pressures evaluated by fractal combustion model (blue lines) mostly overlap with experimental results (red lines), proving the worth calibration method. C_L and c_{wc} tuning for each operating condition of Table 5.3 is the first step of combustion model calibration. A fully predictive approach has been indeed guaranteed by imposing regressions to C_L and c_{wc}, depending on in-cylinder mass thermodynamic and chemical characteristics at SA timing. Regressions comply with 0D-1D characterization of 3D phenomena and for example minimize the inaccuracies of turbulence model results (0D model of a 3D phenomenon) or fractal geometry characterization. For instance, corrugated flame front is evaluated with fractal geometry, but this is just an assumption, which is totally incorrect from extreme leaner combustion [6]. Although fractal combustion model is an adequate tool for combustion prediction, it could be improved with C_L and c_{wc} regressions. Therefore, regressions of the two combustion parameters have been characterized due to abovementioned manual calibration with a least square method:

$$C_L = aT_{SA}{}^b p_{SA}{}^c n^d X_{res}{}^e \lambda^f \tag{5.29}$$

$$c_{wc} = a'T_{SA}{}^{b'} n^{c'} \lambda^{d'} \tag{5.30}$$

Regression coefficients' values are listed in Table 5.4.

Table 5.4: Coefficient of C_L and c_{wc} regressions

C_L coefficients	Value	c_{wc} coefficients	Value
a	95.9	a'	8.9e-3
b	3.9	b'	0.5
c	-1.4	c'	-3e-2
d	-5.5	d'	-0.4
e	-2.2		
f	0.3		

Fractal combustion model with implementation of the abovementioned two regressions could be used effectively for predictive analysis. The model automatically evaluates combustion parameters given by GT-Power as initial conditions. Mass fraction burned is calculated due to turbulence intensity evaluation and fractal estimation. Pressure is instead computed applying energy conservation equation. All steady state operating conditions have been hence numerically reproduced with predictive combustion model. Combustion model capabilities could hence be evaluated by comparing experimental and simulated periods between SA and 50% of mass fraction burned and PFP values. For the sake of conciseness, steady state points out of calibration have been considered and errors for first cylinder have been evaluated.

Kernel growth period and turbulent flame speed are well estimated by fractal predictive combustion model. Indeed, these two parameters affect mainly flame front propagation during development and rapid burning phases and hence influence period between SA and position of 50% of mass fraction burned. Differences of $MFB_{0-50\%}$ periods between experimental data and numerical model results for steady state points out of calibration are shown in Figure 5.16. It is worth recalling that numerical model has been used in a predictive way and, thus, combustion parameters depend on GT-Power initial conditions. Maximum absolute error is equal to 2.5 crank angles, proving the valuable capabilities of predictive combustion model. Mass fraction burned estimation for a longer period (i.e. from SA to 75% of MFB) could be evaluated by considering peak firing pressure estimation. Considering a good estimation of $MFB_{0-50\%}$ period, PFP value is strictly correlated to $MFB_{75\%}$ position.
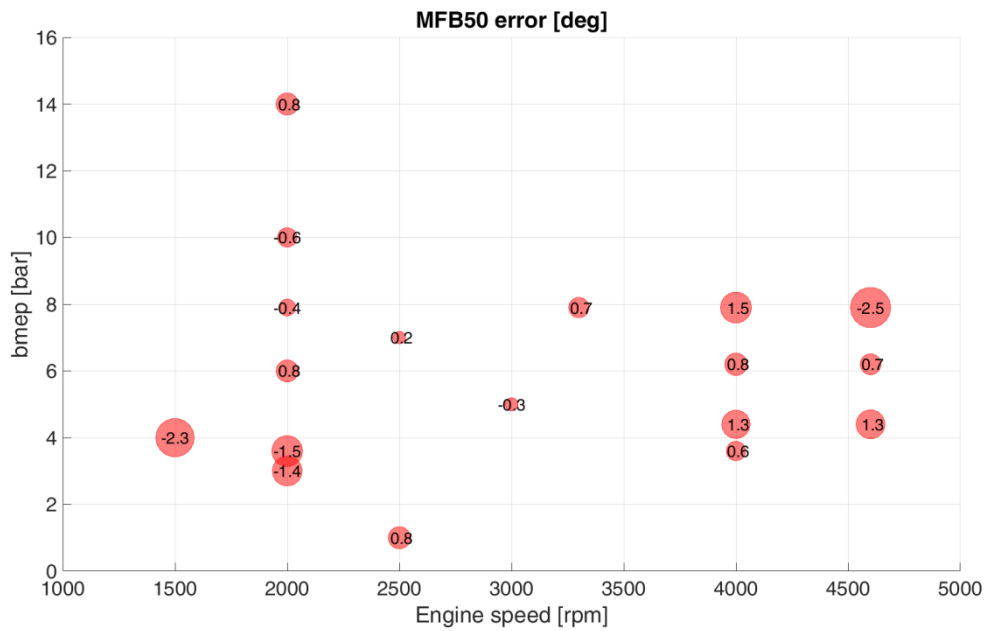
Figure 5.16: Errors of MFB50 position for steady state points out of calibration
(cylinder 1)

Figure 5.17 displays PFP relative errors of numerical models compared with experimental data for validation steady state points. Inaccuracies of maximum pressure are directly connected to numerical results presented in Figure 5.16: overestimation of turbulent flame speed leads to lower $MFB_{0-50\%}$ period and hence to a heat released in a shorter time, resulting in greater in-cylinder maximum pressure. Numerical misleading is clear in operating conditions like 1500x4 or 1600x7.9. On the contrary, underestimation of flame front propagation speed introduces lower PFP (i.e. 4600x4.4). Although maximum absolute error of PFP is equal to 10%, it is worth observing that fractal predictive model has been calibrated in a wide range of operating conditions (different engine speeds, loads, relative air-to-fuel ratio).
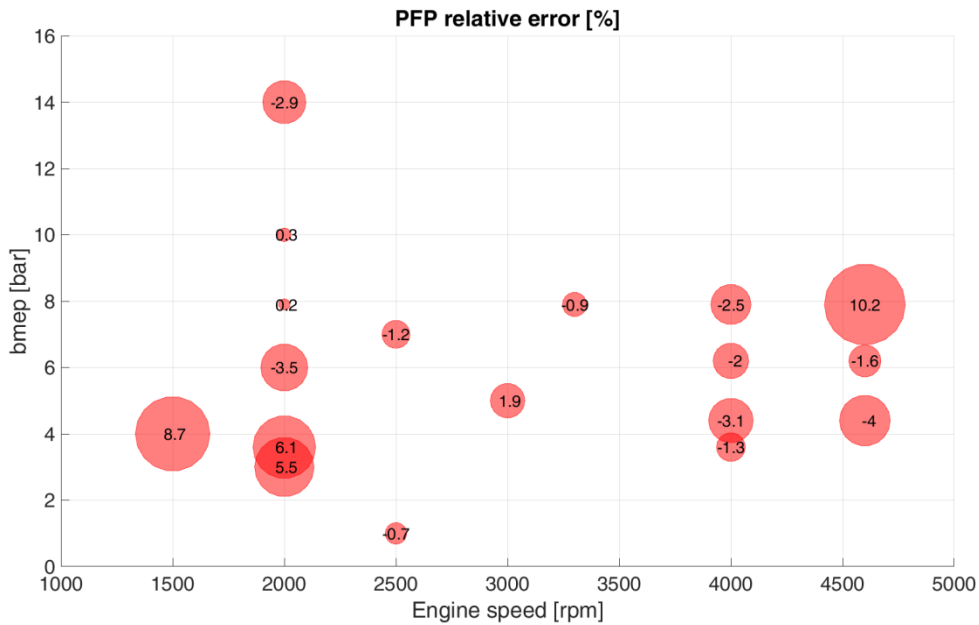
Figure 5.17: PFP relative errors for steady state points out of calibration (cylinder 1)

As a matter of fact, predictive model has been used to simulate lambda sweep tests. Differences of $MFB_{0-50\%}$ periods between experimental data and numerical model results and PFP ones are displayed in Figure 5.18 and 5.19.

Although fractal model has been used and calibrated considering lean and rich operating conditions, fractal characterization of flame front corrugation could be inappropriate [6]. However, combustion model reliability is proved for lean and rich mixture close to stoichiometric conditions. PFP relative errors up to 15% for extreme lean and rich mixture have been approved considering the effectiveness of fractal predictive combustion model in a wide range of operating conditions.
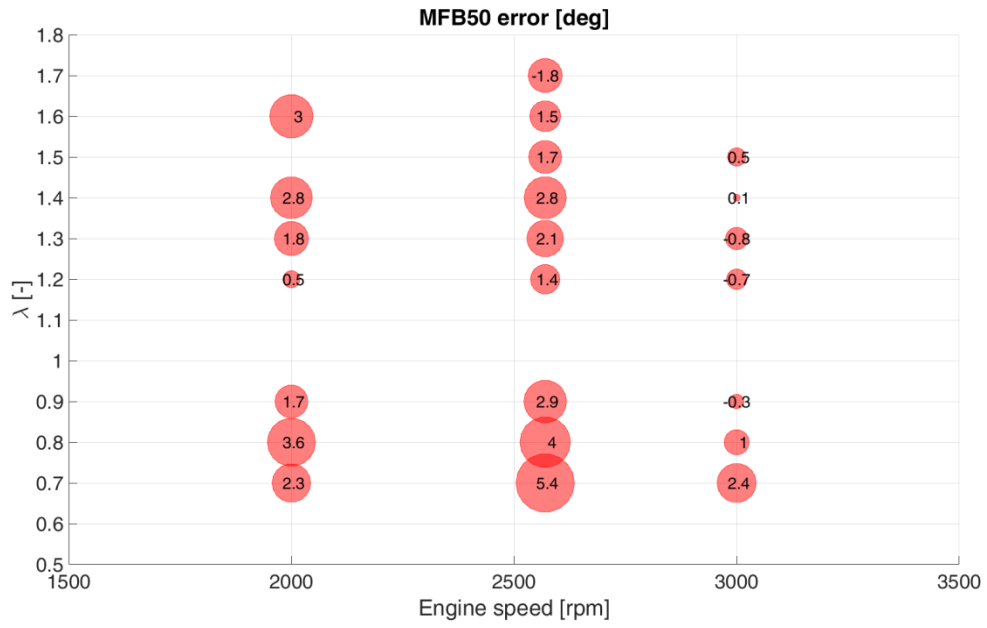
Figure 5.18: Errors of MFB50 position for lambda sweep tests (cylinder 1)

Figure 5.19: PFP relative errors for lambda sweep tests (cylinder 1)

Average in-cylinder pressure cycles have been successfully evaluated by fractal predictive combustion model. Modelling of CCV has been explained in Section 5.2.2: C_L and $\Delta\theta_{0-1\%}$ receive a numerical Gaussian dispersion in order to perturbate the correlation between the turbulence and the flame front area

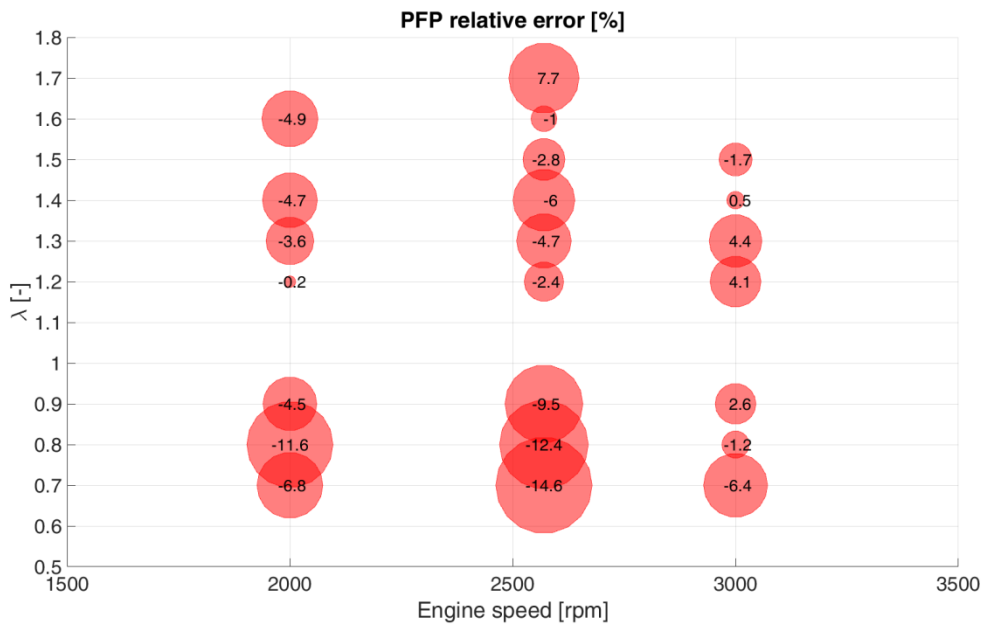and the kernel growth period so as to model the theory of the considered phenomena. The calibration consists in an optimization procedure performed on CoV of the two parameters so as to obtain the best possible correlation of CoV values of PFP for operating conditions listed in Table 5.3. Experimental $\Delta\theta_{0-1\%}$ dispersion at each operating condition has been analyzed with heat release model analysis: its standard deviation is generally equal to 8% of the average value. CoV of C_L parameter is instead slightly engine operating conditions dependent: a correlation between CoV of C_L and thermodynamic conditions during SA has been verified (Table 5.5).

$$CoV_{C_L} = a \left({T_{SA}}/{1000} \right)^b p_{SA}{}^c X_{res}{}^d \lambda^e \qquad (5.31)$$

Table 5.5: Coefficient of CoV_{CL} regression

CoV_{CL} coefficients	Value
a	100
b	5
c	-1.2
d	-0.5
e	0.6

It is worth observing that the two abovementioned combustion parameters are strictly linked with physics phenomena (kernel growth and flame front corrugation) and their numerical dispersion leads to cyclic variation simulation. Comparisons between experimental and simulated standard deviations of peak firing pressure for operating conditions out of calibration and lambda sweep tests are shown in Figure 5.20, 21 and 22. It is worth observing that CCV simulations have been not carried out for leaner cases. CCV physical correlation with fractal characterization of the flame front is indeed unfeasible for extremely leaner mixture (for premixed combustion in SI engine) as

explained in [6]. The good agreement of the simulated standard deviation of the PFP with the experimental one confirms the appropriate application of the fractal predictive combustion model and CCV tool. Moreover, the effectiveness of numerical models is shown in the next three figures.
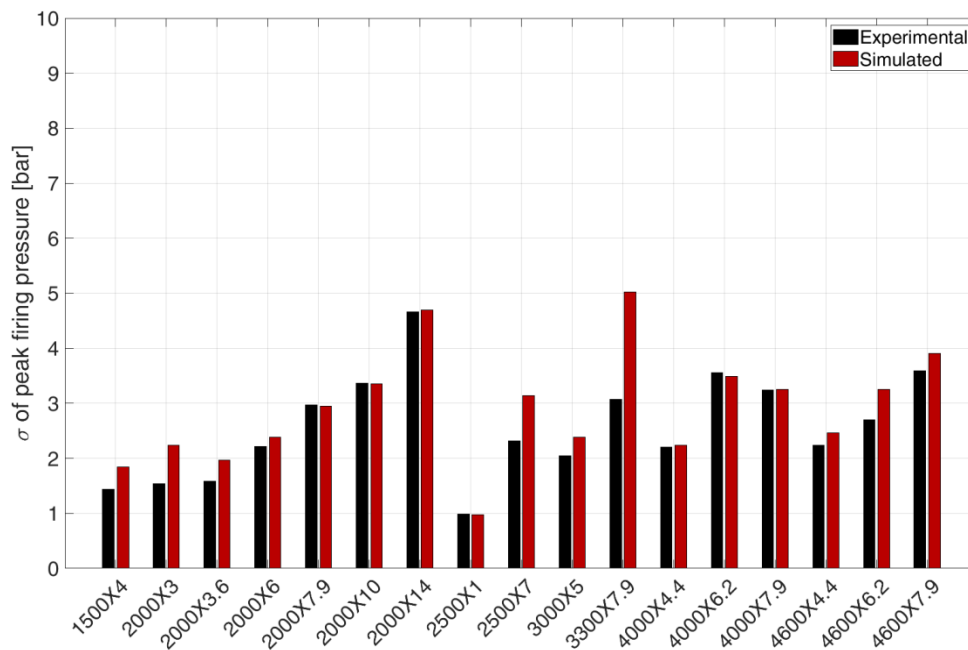

Figure 5.20: Comparison between experimental and simulated standard deviations of PFP for steady state points out of calibration

A satisfying correlation is observed: the simulation data (red bars) are in-line with the experimental readings (black bars). The models have been hence correctly validated. Simulated standard deviations of PFP are aligned with experimental ones except for 3300x7.9 case: the combination of simulated physical conditions at SA leads to a mismatch. Further investigations will be done to deepen the knowledge on these mismatches. However, it is worth recalling that predictive model has been calibrated in order to work correctly in a wide range of operating conditions (different engine speeds, loads and different air-to-fuel mixture). The wide satisfying capability of CCV numerical model among different operating conditions, especially for rich (Figure 5.21) and lean mixtures (Figure 5.22), has a significant role for knock simulation. As explained previously, operating conditions and CCV affect indeed engine behavior, moving from normal combustion to knock one. Nevertheless, 1.4 T-Jet engine fueled with methane was not able to reach knock conditions, due to methane characteristic (extremely higher RON) connected with engine ones

(reduced CR). For this reason, attention has been paid for the second prototype engine. However, validation tests prove numerical models predictability: these tools could be adopted to reduce experimental campaign which is costly and time demanding, considering the amount of degree of freedom.
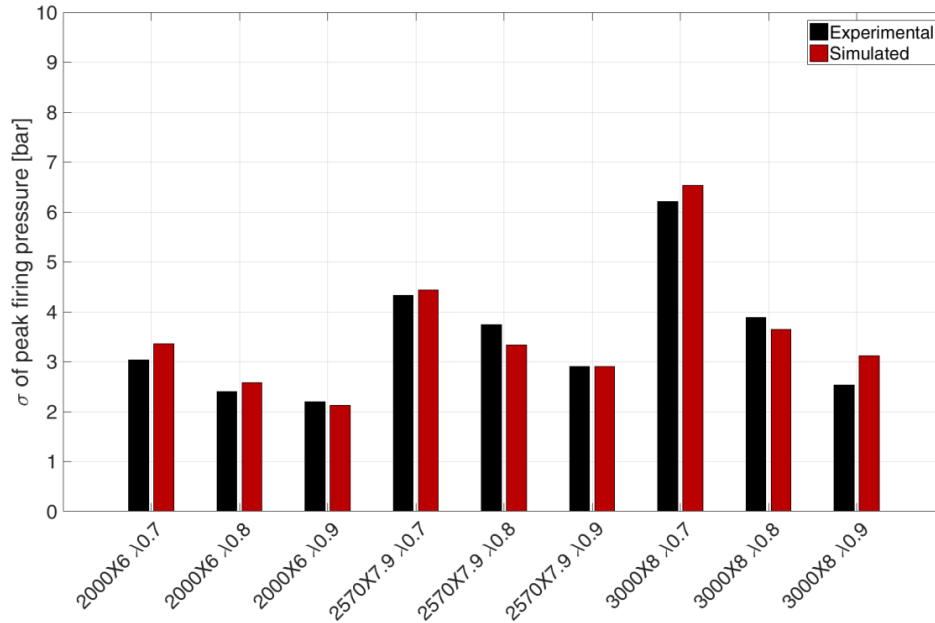

Figure 5.21: Comparison between experimental and simulated standard deviations of PFP for tests with rich mixture
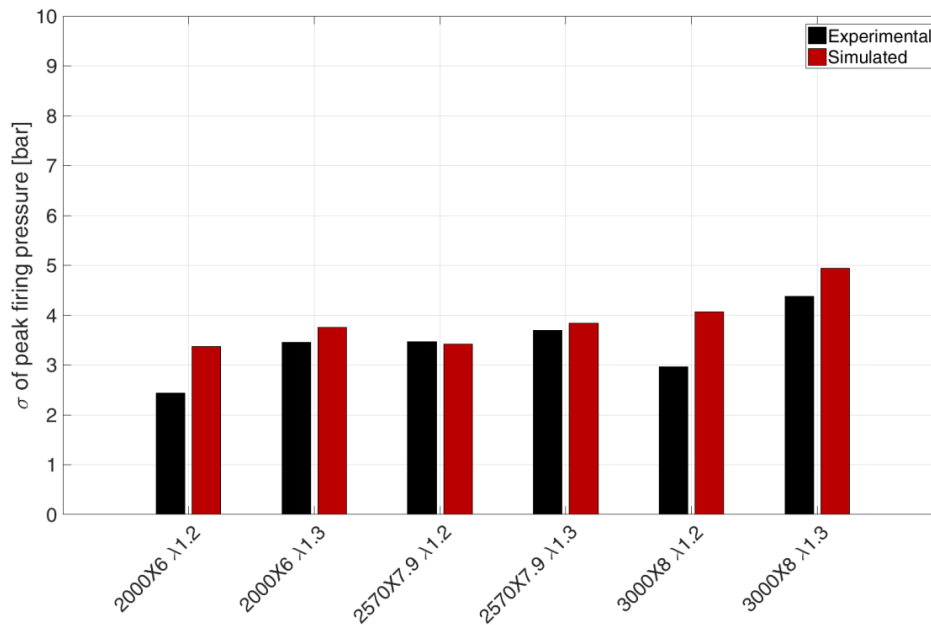
Figure 5.22: Comparison between experimental and simulated standard deviations of PFP for tests with lean mixture

5.5 Numerical results for prototype engine

Prototype engine has been modeled in GT-Power environment and previous predictive numerical models have been implemented to simulate combustion and CCV. Auto-ignition model has been consequently tested due to knock propensity of considered engine: with a CR equal to 13, knock occurrence has been experimentally recognized at medium engine speeds during full load conditions. Therefore, auto-ignition model has been properly tested.

5.5.1 Validation of combustion and CCV numerical models

Numerical models have been calibrated as previously explained in Section 5.4.1. As a matter of fact, GT-Power environment has been still used. Two main differences have to be considered: coefficients of turbulence model and combustion one have been set considering literature suggestions [18-27]; moreover, regression of C_L parameter has been changed due to different intake valvetrain layout. Prototype engine was provided with a VVA intake system. In order to accomplish a satisfying regression, the third parameter (n) has been substituted with the turbulence intensity (u') at spark discharge timing and overall parameters have been recalibrated. The effect of engine speed on correlation between in-cylinder flow pattern and flame front propagation is not affected by intake valve actuation in previous engine because of fixed valve lift shape. Prototype engine could instead provide different intake valve shapes for same engine speeds so as to guarantee different loads (throttle usage was neglected).

All steady state operating conditions have been numerically reproduced with predictive combustion model. Combustion model capabilities have been evaluated by comparing experimental and simulated periods between SA and 50% of mass fraction burned and PFP values. For the sake of conciseness, errors for first cylinder have been considered. Differences of $MFB_{0-50\%}$ periods between experimental data and numerical model results are shown in Figure 5.23. It is worth recalling that numerical model has been used in a predictive way and, thus, combustion parameters depend on GT-Power initial conditions. Maximum absolute error is equal to 4.5 crank angles, 2 crank angle degrees greater than previous engine. Numerical results are satisfactory considering the considerable complexity of prototype engine: DI and VVA affect indeed

reliability of the 0D-1D fractal predictive model due to 3D phenomena. AS previously mentioned, by considering a good estimation of $MFB_{0-50\%}$ period, PFP value is strictly correlated to $MFB_{75\%}$ position.
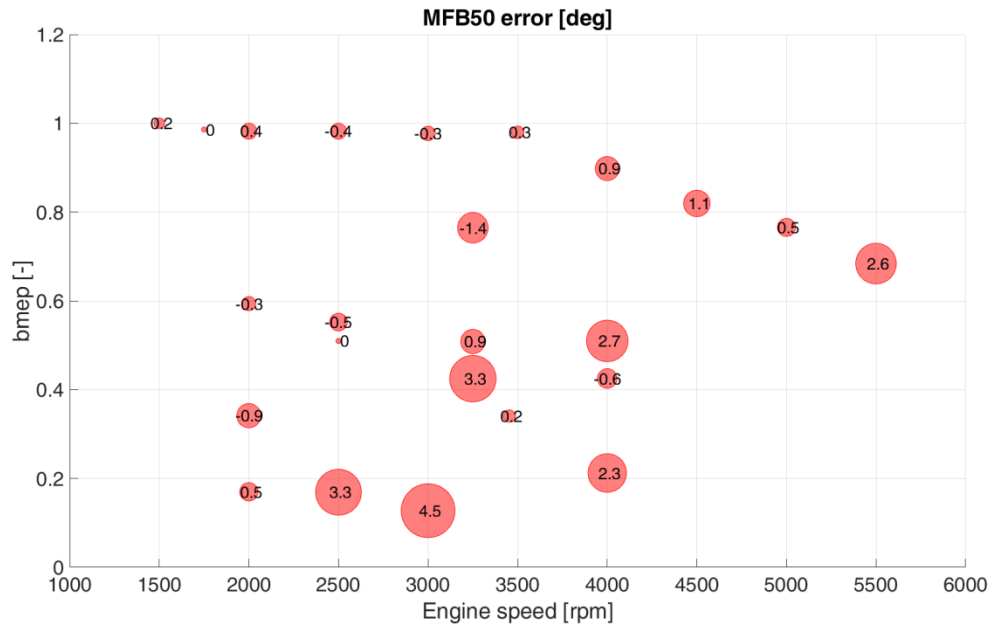

Figure 5.23: Errors of MFB50 position for steady state operating conditions (cylinder 1)

Figure 5.24 displays PFP relative errors of numerical models compared with experimental data for validation steady state points. Underestimation of turbulent flame speed leads to greater $MFB_{0-50\%}$ period and hence to a heat released in a longer time, resulting in lower in-cylinder maximum pressure. Numerical misleading is clear in operating condition at 3000 rpm and lowest load. Although maximum absolute error of PFP is equal to 12.5%, fractal predictive model has been calibrated considering extremely different operating conditions: spread of IVC angles is extremely wide, as IVO ones and injection timings. Unfortunately, due to confidentiality agreement these data could not be shown.
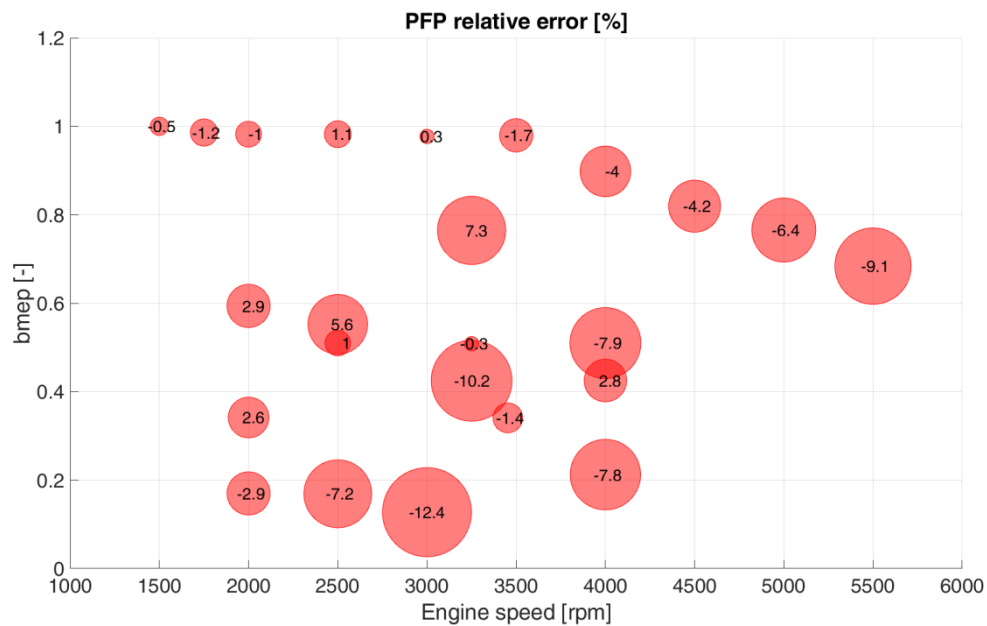
Figure 5.24: PFP relative errors for steady state operating conditions (cylinder 1)

Comparisons between experimental simulated standard deviations of IMEP for full load conditions and partial load ones are displayed in Figure 5.25 and 26. The good agreement of the simulated standard deviation of the IMEP with the experimental one confirms the appropriate application of the fractal predictive combustion model and CCV tool, considering the wide functioning variability of the considered engine: VVA affects indeed residual gas fraction at different speeds and loads, changing cyclic variability. Moreover, the effectiveness of numerical models is shown in the next figures. A satisfying correlation is observed: the simulation data (red bars) are in-line with the experimental readings (black bars). The models have been hence correctly validated. It is worth observing that predictive model has been calibrated in order to work correctly in a wide range of operating conditions. Typically, full load conditions at medium-high engine speeds lead to late intake valve closing strategies (LIVC) while at low speeds normal IVC is coupled with an early intake valve opening (EIVO) in order to apply scavenging effect and boosting turbine performances (and applying internal EGR). On the contrary, during partial load conditions, throttle is substituted with strong early intake valve closing (EIVC): air mass trapped is controlled by changing EIVC always at WOT. Although VVA system reduces pumping losses, EIVC strategies affect dramatically turbulence intensity evolution during compression and even more during combustion, leading to a weakened in-cylinder flow pattern. Therefore,

numerical models are able to simulate correctly combustion and cyclic variation considering the wide boundary condition variation of the abovementioned engine.
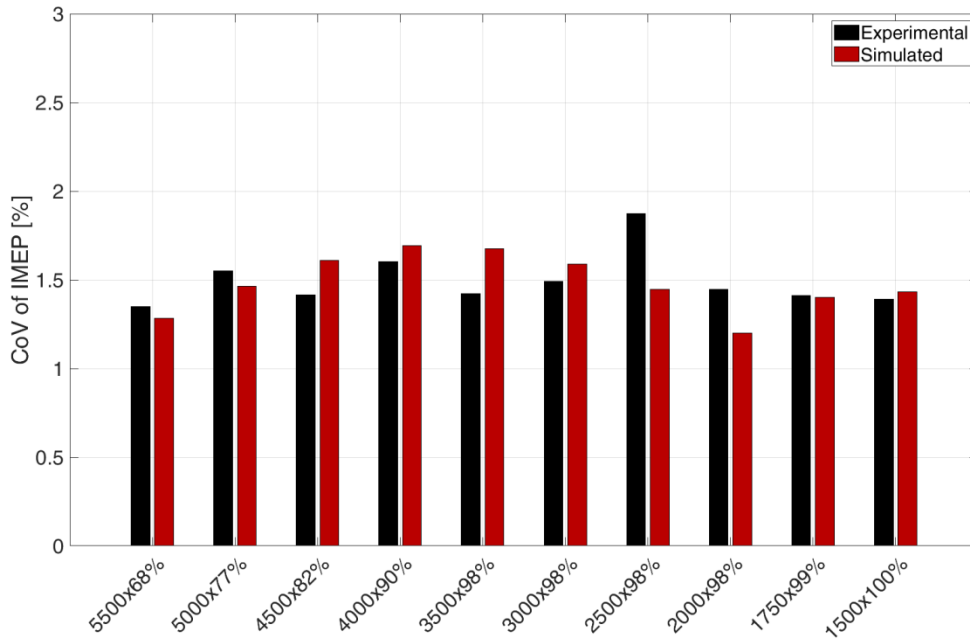
Figure 5.25: Comparison between experimental and simulated CoV of IMEP for full load steady state cases

Figure 5.26 shows CoV of IMEP for partial load cases: 3000x13% case shows how numerical model is able to reproduce correctly cyclic variation when extreme EIVC is adopted. The wide satisfying capability of CCV numerical model among different operating conditions has a significant role for knock simulation. Prototype engine fueled with both fuel mixture highlighted in Table 5.1 was able to reach knock conditions, due to higher CR and overall higher engine performances.
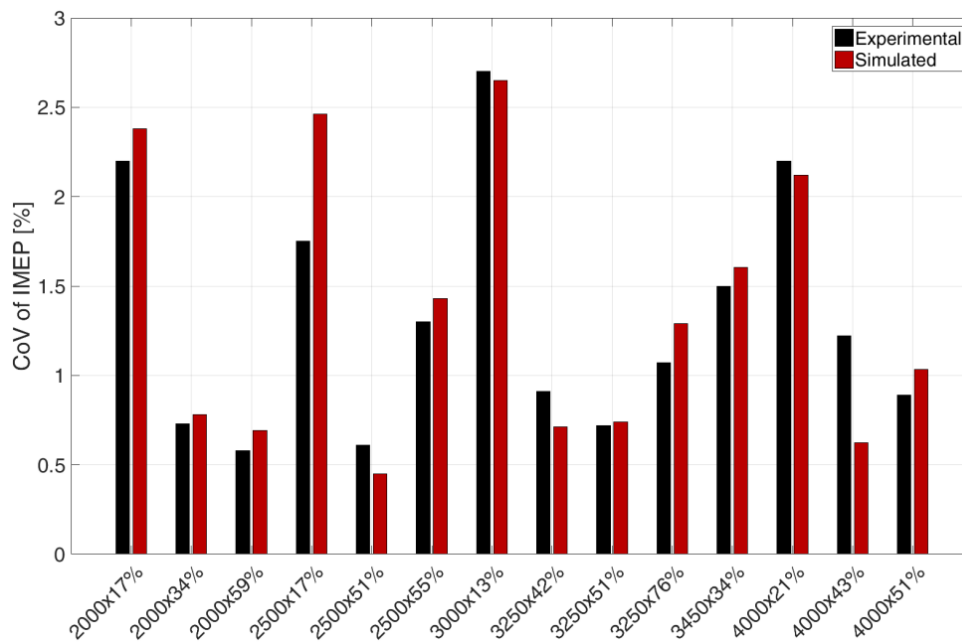
Figure 5.26: Comparison between experimental and simulated CoV of IMEP for partial load steady state cases

5.5.2 Auto-ignition model for knock onset estimation

Auto-ignition integral has been adopted in order to estimate knock onset propensity for different operating conditions. It has to be adopted together with predictive combustion and CCV tools: ignition delay depends on pressure and temperature of unburned gas and on cyclic variation. Moreover, they depend on engine fuel: high RON value for CNG leads to longer ignition delay and hence to lower knock propensity. For this reason, two different fuels have been adopted (Table 5.1). Besides CNG, a methane-ethane blend has been adopted due to higher knock propensity.

The three coefficients of induction time depend on engine fuel. They have been calibrated due to a heat release rate analysis and knock detection tool. Heat release rate outputs have been used as numerical inputs for auto-ignition integral during calibration. The integral has been calibrated using a full factorial DOE for A, n and B values, by targeting knock onset prediction, similarly to [44, 45]: integral value at end of combustion (EOC) analytically discriminates knocking and normal cycles. Integral has been calculated considering experimental pressure data, unburned temperature and EOC deriving from heat release rate model. Starting time has been set equal to EOI or EOC; latest one has been selected. Analytical discrimination has been

compared with experimental results. Experimental in-cylinder data of each cycle have been acquired and knock occurrence has been detected. Starting values for abovementioned parameters has been evaluated starting from findings of [42-45], for two fuel blends as shown in Table 5.1. The parameters' ranges are shown in Table 5.6.

Table 5.6: Parameters of auto-ignition integral

Parameter	Range	First fuel	Second fuel
A	0.001÷0.04	0.003	0.01
n	0.2÷1.8	1.1	0.4
B	5000÷25000	17770	5300

The heat release rate model has been calibrated by targeting the in-cylinder heat transfer depending on engine-out emission quantities and characteristics. Therefore, some changes will be found in GT-Power outputs, in which a Woschni heat transfer theory has been used [1].

Figure 5.27 shows comparison between experimental percentage of knocking cycles (black line and dots) and simulated one (red line and dots) at 1750 rpm during full load condition, for different SA with methane-ethane blend (Table 5.1 second fuel). Intake manifold temperature has been set equal to 50°C in order to enhance knock propensity (by adjusting water flow in inter-cooler). Methane-ethane fuel blend has been selected for two main reason. Firstly, it has a major knock propensity than CNG (which cannot lead to knock occurrence at lower speeds) and hence knock borderline conditions have been analyzed at different engine speeds. Secondly, fractal predictive combustion tool and CCV one have been studied with a quite different fuel (tested CNG was very similar to methane tested with first engine) proving the goodness laminar speed estimation. Two-hundred cycles have been performed for each cylinder. Figure 5.27 displays the robustness of implemented numerical models. As a matter of fact, borderline knock conditions could be evaluated properly, and correct suggestions could be given for experimental tests.
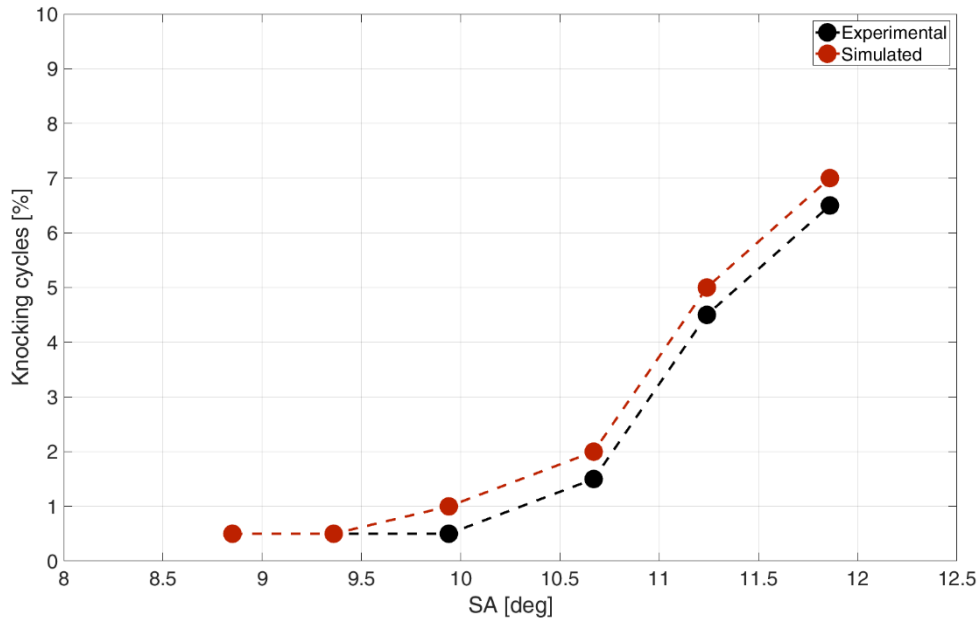
Figure 5.27: Knocking cycles estimation at 1750 rpm for different SA (methane, ethane blend)

Engine behavior and tool capacities with CNG are displayed in Figure 5.28 and 5.29. Numerical models are able to perform acceptable and remarkable results during non-knocking conditions and borderline ones whereas knock combustion conditions are not well estimated. This misleading has to be ascribed to different in-cylinder heat transfer that have not been modeled: under heavy knock conditions in-cylinder heat transfer is indeed influenced [48]. However, research aim was to discriminate borderline conditions to non-knocking one due to mechanical constraints. As shown in next figures, numerical tools correctly estimate percentage of knocking cycles for different engine speeds (and different fuels).
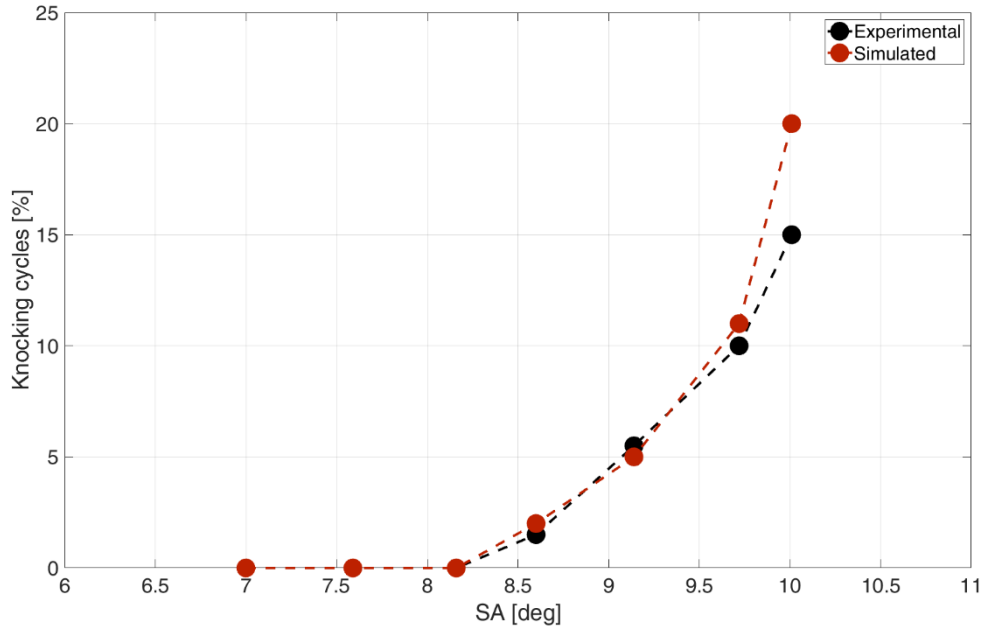
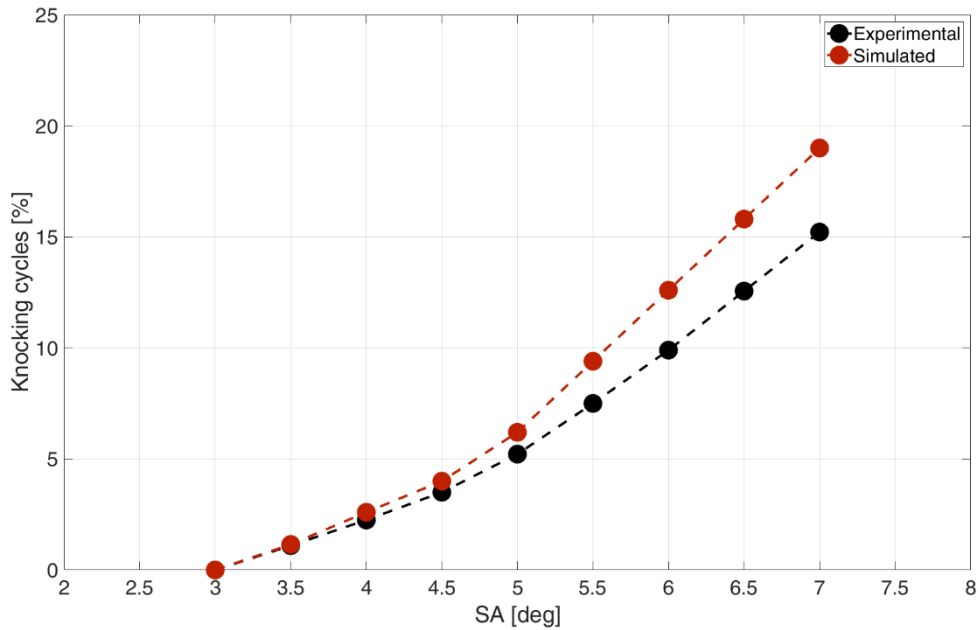Figure 5.28: Knocking cycles estimation at 2000 rpm for different SA (CNG)

Figure 5.29: Knocking cycles estimation at 3500 rpm for different SA (CNG)

5.6 Conclusion

An innovative methodology for combustion, CCV and knock prediction has been proposed. The new procedure has been performed on two different light-duty engines, fueled with methane, CNG and methane-ethane blend. Fractal predictive combustion model has been implemented in GT-Power environment, simulating flame front propagation phenomenon and its distortion due to in-cylinder flow pattern. Turbulence intensity estimation and combustion modeling have been tested with a PFI engine and a DI one with VVA. Correct estimation of the mass fraction burned evolution has been proven by showing the comparison between experimental MFB50 and PFP and simulated ones. Numerical model could guarantee proper results for extremely different boundary conditions. Cyclic variation is instead modeled by acting on fractal model characteristics. A normal distribution has been imposed to kernel growth period and correlation coefficient between turbulent flame speed and turbulent intensity. Research activities show indeed correlation between CCV and flame development phase period and in-cylinder flow pattern variations. Proper normal distributions are imposed, depending on physical boundary conditions. CCV tool correctly estimates cyclic variations at different operating conditions (FL and PL), different relative air-to-fuel ratio and different partial load controls: throttled and VVA ones. Both combustion and CCV numerical models could hence properly simulate different engine operating conditions.

Finally, knock onset is predicted with auto-ignition integral. Methane stability could guarantee a correct estimation of percentage of knocking cycles. The three coefficients of different induction times have been calibrated due to heat release rate analysis and knock detection tool, discriminating knocking cycles to ringing ones. Knock prediction is correctly predicted in borderline conditions, whereas an overestimation is produced for heavy knock conditions. This misleading has to be ascribed to different in-cylinder heat transfer which has not been modeled. However, a correct evaluation of borderline conditions has been addressed to and useful and effective simulation suggestions could hence be provided for new experimental tests. Borderline knock conditions are indeed an application limit for SI high-efficiency engine and the aim of this research activity was to support development and calibration by reducing experimental campaign.

5.7 References

[1]   Heywood, J. B. (1988). Internal combustion engine fundamentals (Vol. 930). New York: Mcgraw-hill.

[2]   Guzzella, L., & Onder, C. (2009). Introduction to modeling and control of internal combustion engine systems. Springer Science & Business Media.

[3]   GT-SUITE Engine Performance Application Manual, Gamma Technologies, 2016.

[4]   Peters, N. (2000). Turbulent combustion. Cambridge university press.

[5]   Borghi, R. (1985). On the structure and morphology of turbulent premixed flames. In Recent advances in the Aerospace Sciences (pp. 117-138). Springer, Boston, MA.

[6]   Aleiferis, P. G., Taylor, A. M., Whitelaw, J. H., Ishii, K., & Urata, Y. (2000). Cyclic variations of initial flame kernel growth in a Honda VTEC-E lean-burn spark-ignition engine (No. 2000-01-1207). SAE Technical Paper.

[7]   Maly, R. (1984). Spark ignition: its physics and effect on the internal combustion engine. In Fuel economy (pp. 91-148). Springer, Boston, MA.

[8]   Kalghatgi, G. T. (1989). Flame initiation and development from glow discharges—Effect of electrode deposits. Combustion and flame, 77(3-4), 321-336.

[9]   Whitelaw, J. H., & Xu, H. M. (1993). An Experimental Study of Gas Velocity, Flame Propagation and Pressure in a Spark Ignition Engine (No. 932702). SAE Technical Paper.

[10]   Le Coz, J. F. (1992). Cycle-to-cycle correlations between flow field and combustion initiation in an SI engine (No. 920517). SAE Technical Paper.

[11] Sztenderowicz, M. L., & Heywood, J. B. (1990). Mixture nonuniformity effects on SI engine combustion variability (No. 902142). SAE Technical Paper.

[12] Mittal, V., Revier, B. M., & Heywood, J. B. (2007). Phenomena that determine knock onset in spark-ignition engines (No. 2007-01-0007). SAE Technical Paper.

[13] Draper, C. S. (1938). Pressure waves accompanying detonation in the internal combustion engine. Journal of the Aeronautical Sciences, 5(6), 219-226.

[14] Naber, J., Blough, J. R., Frankowski, D., Goble, M., & Szpytman, J. E. (2006). Analysis of combustion knock metrics in spark-ignition engines (No. 2006-01-0400). SAE Technical Paper.

[15] Kirsten, M., Pirker, G., Redtenbacher, C., Wimmer, A., & Chmela, F. (2016). Advanced Knock Detection for Diesel/Natural Gas Engine Operation. SAE International Journal of Engines, 9(2016-01-0785), 1571-1583.

[16] Eng, J. A. (2002). Characterization of pressure waves in HCCI combustion (No. 2002-01-2859). SAE Technical Paper.

[17] Tsurushima, T., Kunishima, E., Asaumi, Y., Aoyagi, Y., & Enomoto, Y. (2002). The effect of knock on heat loss in homogeneous charge compression ignition engines (No. 2002-01-0108). SAE Technical Paper.

[18] Baratta, M., Catania, A. E., Spessa, E., & Vassallo, A. (2005, January). Flame Propagation Speed in SI Engines: Modeling and Experimental Assessment. In ASME 2005 Internal Combustion Engine Division Fall Technical Conference (pp. 193-208). American Society of Mechanical Engineers.

[19] Baratta, M., Catania, A. E., Spessa, E., & Vassallo, A. (2006). Development and Assessment of a Multizone Combustion Simulation Code for SI Engines Based on a Novel Fractal Model (No. 2006-01-0048). SAE Technical Paper.

[20] Baratta, M., Catania, A. E., d'Ambrosio, S., & Spessa, E. (2008). Prediction of Combustion Parameters, Performance, and Emissions in Compressed Natural Gas and Gasoline SI Engines. Journal of Engineering for Gas Turbines and Power, 130(6), 062805.

[21] De Bellis, V., Severi, E., Fontanesi, S., & Bozza, F. (2014). Hierarchical 1D/3D approach for the development of a turbulent combustion model applied to a VVA turbocharged engine. Part I: turbulence model. Energy Procedia, 45, 829-838.

[22] De Bellis, V., Severi, E., Fontanesi, S., & Bozza, F. (2014). Hierarchical 1D/3D approach for the development of a turbulent combustion model applied to a VVA turbocharged engine. Part II: combustion model. Energy Procedia, 45, 1027-1036.

[23] Tong, Y. (2017). Technologies for CO2 Reductions in ICEs (Doctoral dissertation, Politecnico di Torino).

[24] Gülder, Ö. L., Smallwood, G. J., Wong, R., Snelling, D. R., Smith, R., Deschamps, B. M., & Sautet, J. C. (2000). Flame front surface characteristics in turbulent premixed propane/air combustion. Combustion and Flame, 120(4), 407-416.

[25] Gouldin, F. C., & Miles, P. C. (1995). Chemical closure and burning rates in premixed turbulent flames. Combustion and Flame, 100(1-2), 202-210.

[26] Poulos, S. G., & Heywood, J. B. (1983). The effect of chamber geometry on spark-ignition engine combustion (No. 830334). SAE Technical Paper.

[27] Bozza, F., Gimelli, A., Strazzullo, L., Torella, E., & Cascone, C. (2007). Steady-state and transient operation simulation of a "downsized" turbocharged SI engine (No. 2007-01-0381). SAE Technical Paper.

[28] Baratta, M., d'Ambrosio, S., Spessa, E., & Vassallo, A. (2006, January). Cycle-Resolved Detection of Combustion Start in SI Engines by Means of Different In-Cylinder Pressure Data Reduction Techniques. In ASME 2006 Internal Combustion Engine Division

Spring Technical Conference (pp. 303-316). American Society of Mechanical Engineers.

[29] Elia, M., Ulinski, M., & Metghalchi, M. (2001). Laminar burning velocity of methane–air–diluent mixtures. Journal of engineering for gas turbines and power, 123(1), 190-196.

[30] http://combustion.berkeley.edu/gri-mech/version30/text30.html

[31] Hu, E., Li, X., Meng, X., Chen, Y., Cheng, Y., Xie, Y., & Huang, Z. (2015). Laminar flame speeds and ignition delay times of methane–air mix tures at elevated temperatures and pressures. Fuel, 158, 1-10.

[32] Donohoe, N., Heufer, A., Metcalfe, W. K., Curran, H. J., Davis, M. L., Mathieu, O., ... & Güthe, F. (2014). Ignition delay times, laminar flame speeds, and mechanism validation for natural gas/hydrogen blends at elevated pressures. Combustion and Flame, 161(6), 1432-1443.

[33] Vermorel, O., Richard, S., Colin, O., Angelberger, C., Benkenida, A., & Veynante, D. (2009). Towards the understanding of cyclic variability in a spark ignited engine using multi-cycle LES. Combustion and Flame, 156(8), 1525-1541.

[34] Enaux, B., Granet, V., Vermorel, O., Lacour, C., Pera, C., Angelberger, C., & Poinsot, T. (2011). LES study of cycle-to-cycle variations in a spark ignition engine. Proceedings of the combustion Institute, 33(2), 3115-3122.

[35] Vitek, O., Macek, J., Poetsch, C., & Tatschl, R. (2013). Modeling cycle-to-cycle variations in 0-d/1-d simulation by means of combustion model parameter perturbations based on statistics of cycle-resolved data. SAE International Journal of Engines, 6(2013-01-1314), 1075-1098.

[36] Millo, F., Rolando, L., Pautasso, E., & Servetto, E. (2014). A methodology to mimic cycle to cycle variations and to predict knock occurrence through numerical simulation (No. 2014-01-1070). SAE Technical Paper.

[37] Lee, K. H., & Foster, D. E. (1995). Cycle-by-cycle variations in combustion and mixture concentration in the vicinity of spark plug gap (No. 950814). SAE Technical Paper.

[38] Johansson, B. (1993). Influence of the velocity near the spark plug on early flame development (No. 930481). SAE Technical Paper.

[39] Elmqvist, C., Lindström, F., Ångström, H. E., Grandin, B., & Kalghatgi, G. (2003). Optimizing engine concepts by using a simple model for knock prediction (No. 2003-01-3123). SAE Technical Paper.

[40] Soylu, S., & Van Gerpen, J. (2003). Development of an autoignition submodel for natural gas engines☆. Fuel, 82(14), 1699-1707.

[41] Saikaly, K., Le Corre, O., Rahmouni, C., & Truffet, L. (2010). Preventive knock protection technique for stationary SI engines fuelled by natural gas. Fuel Processing Technology, 91(6), 641-652.

[42] Chen, L., Li, T., Yin, T., & Zheng, B. (2014). A predictive model for knock onset in spark-ignition engines with cooled EGR. Energy Conversion and Management, 87, 946-955.

[43] Beccari, S., Pipitone, E., & Genchi, G. (2015). Calibration of a knock prediction model for the combustion of gasoline-LPG mixtures in spark ignition engines. Combustion Science and Technology, 187(5), 721-738.

[44] Beccari, S., Pipitone, E., & Genchi, G. (2016). Knock onset prediction of propane, gasoline and their mixtures in spark ignition engines. Journal of the Energy Institute, 89(1), 101-114.

[45] Pipitone, E., Genchi, G., & Beccari, S. (2015). An NTC zone compliant knock onset prediction model for spark ignition engines. Energy Procedia, 82, 133-140.

[46] Catania, A. E., Misul, D., Spessa, E., & Vassallo, A. (2004, August). A Diagnostic Tool for the Analysis of Heat Release, Flame Propagation Parameters and NO Formation in SI Engines (SI Engines, Combustion Diagnostics). In The Proceedings of the

International symposium on diagnostics and modeling of combustion in internal combustion engines 2004.6 (pp. 471-486). The Japan Society of Mechanical Engineers.

[47] Millo, F., & Ferraro, C. V. (1998). Knock in SI engines: a comparison between different techniques for detection and control (No. 982477). SAE Technical Paper.

[48] Ferraro, C. V., Marzano, M. R., Millo, F., & Bochicchio, N. (1996). Comparison between heat transfer and knock intensity on a statistical basis (No. 962101). SAE Technical Paper.